AgRISTARS

SM-YO-00495

NAS7-100

A Joint Program for Agriculture and Resources Inventory Surveys Through Aerospace Remote Sensing

Soil Moisture

SEPTEMBER 15, 1980

STUDY REPORT

JOINT MICROWAVE AND INFRARED STUDIES FOR SOIL MOISTURE DETERMINATION

By:

E.G. NJOKU

J.P. SCHIELDGE

A.B. KAHLE

PREPARED BY

JET PROPULSION LABORATORY
CALIFORNIA INSTITUTE OF TECHNOLOGY
PASADENA, CALIFORNIA

(JPL PUBLICATION 80-57)

1. Report No.	2. Government Accession No.	3. Recipient's Catalog No.
SM-YO-00495		

4. Title and Subtitle	5. Report Date
Joint Microwave and Infrared Studies for Soil Moisture Determination	September 15, 1980
	6. Performing Organization Code

7. Author(s)	8. Performing Organization Report No.
E. G. Njoku, J. Schieldge, A. B. Kahle	80-57
	10. Work Unit No.

9. Performing Organization Name and Address	11. Contract or Grant No.
Jet Propulsion Laboratory 4800 Oak Grove Drive Pasadena, California 91103	NAS7-100
	13. Type of Report and Period Covered

12. Sponsoring Agency Name and Address	13. Type of Report and Period Covered
National Aeronautics and Space Administration Washington, D.C. 20546	External Report
	14. Sponsoring Agency Code

15. Supplementary Notes

16. Abstract

Remote sensing can potentially be of great value in determining the moisture content of soils on a regular basis and over large areas of land. There is need to know which sensors -- or combination of sensors -- are most effective for this task. This study deals with the feasibility of using a combined microwave-thermal infrared system to determine soil moisture content. This report deals strictly with bare soils and contains a description of the theoretical basis for microwave emission from soils, and the transport of heat and moisture in soils. Also, a description is given of the results of two field experiments held during the vernal months of 1978 and 1979 in the San Joaquin Valley of California.

17. Key Words (Suggested by Author(s))	18. Distribution Statement
Agriculture (General); Hydrology and Limnology; Soil Mechanics; Earth Resources	Unlimited

19. Security Classif. (of this report)	20. Security Classif. (of this page)	21. No. of Pages	22. Price*
Unclassified	Unclassified	130	

*For sale by the National Technical Information Service, Springfield, Virginia 22161

SM-YO-00495

NAS7-100

STUDY REPORT

JOINT MICROWAVE AND INFRARED STUDIES FOR SOIL MOISTURE DETERMINATION

BY

E. G. Njoku

J. P. Schieldge

A. B. Kahle

This report deals with the feasibility of using a combined microwave-thermal infrared system to determine soil moisture content.

JET PROPULSION LABORATORY
CALIFORNIA INSTITUTE OF TECHNOLOGY
PASADENA, CALIFORNIA 91103

September 15, 1980

The research described in this publication was carried out by the Jet Propulsion Laboratory, California Institute of Technology, under NASA Contract No. NAS7-100.

TABLE OF CONTENTS

TABLE OF CONTENTS (cont'd)

Figures

TABLE OF CONTENTS (cont'd)

TABLE OF CONTENTS (cont'd)

Tables

INTRODUCTION

Quantitative soil moisture measurements on a global basis are essential for planning and modeling in agriculture, climatology, and hydrology. A major part of the soil moisture information currently used for these purposes is derived from measurements of precipitation. These precipitation measurements, in general, do not provide sufficient coverage and are not uniquely correlated to soil moisture content. With the spatial and temporal coverage requirements, it would be highly desirable to obtain soil moisture information from satellites. A likely candidate for a sensor system to measure soil moisture from space combines passive microwave and thermal infrared (IR) detectors. It is now possible to orbit large microwave antennas which can provide sufficient surface resolution at the lower frequencies to enable meaningful measurements of soil moisture content to be made. Thermal infrared data can be obtained simultaneously to improve the soil moisture determination algorithms.

The potential of microwave radiometry for soil moisture sensing lies in the marked increase in the dielectric constant of wet soil over that of dry soil, due to the presence of moisture. The resultant decrease in emissivity leads to a pronounced decrease in the microwave brightness temperature which is measurable by remote sensors. This has been confirmed in the past by a series of ground-based and aircraft measurements which show an approximately linear decrease in brightness temperature as a function of increasing moisture content. These measurements exhibit a rather large scatter, however, due to the numerous other surface features which also affect the microwave emission.

This study is an attempt to better quantify the effects of these surface features such as variations in the moisture and temperature profiles, subsurface layering, surface roughness, and vegetation cover. Theoretical models

have been developed starting on a simple basis, and are being extended to account for the significant features found in natural terrain.

The microwave brightness temperature is affected by surface temperature as well as the other surface characteristics discussed above. Thus, surface temperature measurements by thermal infrared will improve the soil moisture determination accuracy of a microwave instrument alone. Furthermore, an indication of the soil thermal inertia made possible by such infrared measurements provides additional information on the moisture content. A coupled soil heat and moisture flux model has been developed to aid in interpretation of the infrared data. A major objective of this study is to examine the interrelationships between the microwave and infrared models, and ultimately to derive algorithms for retrieving near-surface soil moisture information from combined microwave and infrared remotely-sensed data sets.

Field experiments have been undertaken in the southern San Joaquin Valley, California, to acquire data to enable verification and improvement of both microwave and thermal-moisture models. Data were obtained using microwave and infrared ground-based systems. The test sites consisted of bare fields with the capability of being ploughed, irrigated, and instrumented at will. The field work was undertaken in cooperation with Dr. John Estes, S. Atwater, P. O'Neill, and other students of the Geography Remote Sensing Unit, U. C. Santa Barbara. Measurements with the microwave radiometric system - consisting of UHF (0.6 to 0.9 GHz/50.0 to 33.3 cm), L band (1.42 GHz/21.4 cm), and X band (10.69 GHz/2.8 cm) channels - were made at horizontal and vertical polarizations as functions of view angle, soil moisture and temperature conditions, and surface roughness. Measurements of surface thermal infrared emission were made from 8 to 14 μm.

Soil samples were obtained at frequent intervals during the experiment for analysis in terms of moisture content, bulk density, and texture. Temperature probes were used at various depths to monitor the changing temperature profiles. The net result was a complete set of subsurface temperature and moisture profiles as a function of time during the course of the experiment.

Measurements of the micrometeorological conditions in the lower (surface) boundary layer were also made.

This report describes the two modeling efforts, the data acquisition and interpretation, and future plans for combining measurements and models of the two spectral regions into a valid soil moisture measurement technique.

MICROWAVE EMISSION FROM BARE SOILS

Introduction

Microwave emission from soils depends on soil characteristics that can be divided into two groups: (a) volume characteristics, and (b) surface characteristics. Volume characteristics are those which determine the thermal and dielectric properties of the bulk medium (e.g., moisture content, soil type, and inclusions such as rocks and organic matter). Surface characteristics include roughness and vegetation cover, and can be natural or man-made (such as agricultural fields). The effects of these soil characteristics have been studied in the past using both theoretical and experimental approaches. At the frequencies of interest (~ 1 to 10 GHz) soil moisture content is the dominant characteristic affecting emission from bare soils.

Various theoretical models have been developed to compute microwave emission from surfaces. These models include emissivity calculations (Peake, 1959; Tsang and Kong, 1976), radiative transfer models (England, 1974; Tsang and Kong, 1975; Burke et al., 1979), and more rigorous coherent models (Stogryn, 1970; Tsang et al., 1975; Wilheit, 1978). In general, these models treat idealized situations, since some soil characteristics are too complex to be accurately modeled. In particular, surface roughness and vegetation have not so far been adequately represented in the models. Even in simplified form, however, the models have provided an understanding of the basic soil emission characteristics to be obtained, and can be used to obtain approximate results for situations in which experimental data are unavailable.

Experimental programs in soil moisture remote sensing have provided microwave data from ground-based radiometer measurements (Poe et al., 1971; Blinn et al., 1972; Newton, 1976), aircraft measurements (Schmugge et al., 1974, 1976), and satellite measurements (Eagleman and Lin, 1976; McFarland,

1976; Meneely, 1977). These radiometer measurements, in conjunction with simultaneous ground-truth measurements of moisture and temperature, have enabled empirical relationships to be obtained between microwave brightness temperature and soil moisture content. Other soil characteristics such as soil type, roughness and vegetation cover are observed as perturbing effects on these relationships. The limited nature of the radiometer measurements, and the difficulties encountered in obtaining accurate ground-truth measurements for comparison, have been the main limitations to the experimental work so far.

Understanding the effects of soil characteristics on microwave emission will enable techniques to be devised for retrieving surface soil moisture information from analyses of remotely-sensed microwave data. The success of the procedure depends on understanding which moisture parameters primarily affect the microwave emission (e.g., surface moisture, sub-surface moisture profile, etc.), and how these parameters are to be interpreted when roughness and vegetation are present, or when several different terrain types fall within the field of view. A further step is to evaluate the usefulness of the derived moisture parameters in their application to problems in agriculture, hydrology and climate, which is the ultimate goal of these studies.

The microwave soil moisture studies carried out at JPL have emphasized aspects of both theoretical modeling and experimental measurements. Theoretical models have been developed for bare soil surfaces with vertical moisture and temperature profiles. Experimental data have been obtained using JPL's van-mounted radiometers, operating at 0.6 to 0.9 GHz (tunable), 1.42 GHz and 10.69 GHz. The experimental data have been used to verify the calculations of the smooth surface model, and are being used to make empirical modifications to the model to account for effects of surface roughness.

Theoretical Background

Most soils can be adequately modeled at microwave frequencies as being isotropic and non-scattering, with vertically inhomogeneous dielectric constant and temperature profiles (figure 1). The dielectric constant profile is determined by the moisture profile, soil texture, and any discontinuities such as rock strata, etc. The most general approach to deriving a theoretical formulation for the brightness temperature of such a medium uses the theory of electromagnetic fluctuations and electromagnetic wave propagation. This approach was formulated by Stogryn (1970) for a medium with continuously varying vertical profiles. Stogryn's formulation can be modified to give the following expressions for the brightness temperature as a function of viewing angle for horizontal and vertical polarizations (Njoku and Kong, 1977):

$$T_{B_h}(\delta) = \frac{k}{\cos\delta} \int_{-\infty}^{0} T(z)\, \varepsilon_r''(z) |\psi(z)|^2 \, dz \qquad (1a)$$

$$T_{B_v}(\delta) = \frac{1}{k \cos\delta} \int_{-\infty}^{0} T(z)\, \varepsilon_r''(z) \left\{ \left| \frac{1}{\varepsilon_r(z)} \frac{d\phi(z)}{dz} \right|^2 + \left| \frac{1}{\varepsilon_r(z)} \; k \sin\delta \; \phi(z) \right|^2 \right\} dz \qquad (1b)$$

In these expressions T(z) is the temperature profile, $\varepsilon_r(z) = \varepsilon_r'(z) + i\varepsilon_r''(z)$ is the complex dielectric constant profile, k is the free-space wave number ($2\pi/\lambda$), and δ is the angle of observation from nadir. The functions $\psi(z)$ and $\phi(z)$ are obtained as solutions to two second-order differential equations:

$$\frac{d^2\psi(z)}{dz^2} + \{\varepsilon_r(z) - \sin^2\delta\}\ k^2\psi(z) = 0$$

$$\varepsilon_r(z)\ \frac{d}{dz}\ \{\frac{1}{\varepsilon_r(z)}\ \frac{d\phi(z)}{dz}\} + \{\varepsilon_r(z) - \sin^2\delta\}\ k^2\phi(z) = 0 \qquad (2)$$

These are the wave propagation equations within the medium, and must be solved in conjunction with appropriate surface boundary conditions. For a smooth surface, these boundary conditions are given by:

$$\frac{d\psi(z)}{dz} + i\ \{2 - \psi(z)\}\ k\cos\delta = 0, \text{ at } z = 0$$

$$\frac{d\phi(z)}{dz} + i\ \{2 - \phi(z)\}\ \varepsilon_r(z)\ k\cos\delta = 0, \text{ at } z = 0 \qquad (3)$$

For a rough surface the boundary conditions become complicated, and even the simplest forms of roughness result in solutions which are intractable for most applications. Thus, solutions of these general equations are usually restricted to the smooth surface case. For the smooth surface, solutions to equations 2 for $\psi(z)$ and $\phi(z)$ can be obtained in terms of known functions only for certain simple analytic profiles of $\varepsilon_r(z)$. Some of these general solutions have been described by Wait (1962). In most practical situations, profiles of $\varepsilon_r(z)$ as determined by the soil moisture profile $\theta(z)$ may be quite arbitrary, so that solutions for $\psi(z)$ and $\phi(z)$ cannot easily be obtained, and much less be integrated in equation 1 to obtain brightness temperature. The above formulation does however provide a useful framework against which to evaluate other models which may not be as accurate but afford much simpler computation in practical cases. These approximate models are discussed below.

Emissivity Model

The emissivity model is the simplest to use in concept. It assumes that the temperature in the medium is uniform, $T(z) = T$, so that the temperature can be removed from the integral of equation 1, and the brightness temperature expressed as:

$$T_{B_p}(\delta) = e_p(\delta)T \tag{4}$$

where $e_p(\delta)$ is the emissivity, and p refers to either vertical v or horizontal h polarization. Due to the reciprocal nature of the boundary conditions (Peake, 1959; Tai, 1971) the emissivity can be related to the reflectivity $r_p(\delta)$ by the relation:

$$e_p(\delta) = 1 - r_p(\delta) \tag{5}$$

In the case of a smooth surface over a homogeneous medium, $r_p(\delta)$ is obtained from the Fresnel reflection coefficients $R_p(\delta)$ (Kong, 1975):

$$r_p(\delta) = |R_p(\delta)|^2 \tag{6}$$

In the case of a rough surface, scattering coefficients can be used to compute the reflectivity using Peake's approach (Peake, 1959):

$$r_p(\delta) = \frac{1}{4\pi} \iint \left[\gamma_{pp}(o,s) + \gamma_{pq}(o,s)\right] d\Omega_s \tag{7}$$

where the integral is over the upper half-space, the $\gamma(o,s)$ are bistatic scattering coefficients from direction (s) into direction (o), and q refers to the polarization orthogonal to p.

For inhomogeneous media, techniques for computing reflectivity outlined by Wait (1962) can be used if the surface is smooth.

The emissivity model can be used with reasonable accuracy even for situations where the temperature profile is non-uniform, provided the temperature variation is small in the near-surface sensing depth region. In this case the temperature T can be taken as the surface temperature, or an "effective" average temperature over the sensing depth. For the lower microwave frequencies, significant soil temperature variations can occur within the greater sensing depths at these frequencies, hence the emissivity approach should not be used in these cases.

Radiative Transfer Model

The radiative transfer approach can be used to obtain approximate values of brightness temperature for media in which the dielectric constant profile is slowly-varying and in which the absorption is small (Njoku and Kong, 1977). It is fairly straightforward to implement, and is thus commonly used. To illustrate its applicability, it will be derived here as an approximation to the rigorous expression given in equation 1.

The differential equations (2) can be written in the concise form:

$$\frac{d^2\chi(z)}{dz^2} + g^2(z)\chi(z) = 0 \qquad (8)$$

where,

$$\chi(z) = \begin{cases} \psi(z), & \text{horizontal polarization} \\ \dfrac{\phi(z)}{\sqrt{\varepsilon_r(z)}}, & \text{vertical polarization} \end{cases}$$

and,

$$g^2(z) = \begin{cases} k^2[\varepsilon_r(z) - \sin^2\delta], \text{ horizontal polarization} \\ k^2[\varepsilon_r(z) - \sin^2\delta] - \sqrt{\varepsilon_r(z)}\ \dfrac{d^2}{dz^2}\left(\dfrac{1}{\sqrt{\varepsilon_r(z)}}\right), \text{ vertical polarization} \end{cases}$$

Equation 8 can be solved approximately using the WKB approach (Wait, 1962), which is valid in cases where the profile $\varepsilon_r(z)$ varies slowly over distances comparable to a wavelength in the medium. It can be shown that solutions of the form

$$\chi(z) = \frac{1}{\sqrt{g(z)}}\ e^{-i\int_0^z g(z')\,dz'} \tag{9}$$

will satisfy equation 8 under the slowly-varying conditions:

$$\frac{1}{\sqrt{\varepsilon_r(z)}}\ \frac{d}{dz}\ \{\sqrt{\varepsilon_r(z)}\} \ll g(z)$$

Using the boundary conditions of equation 3, and substituting into equation 1 the expression for brightness temperature is obtained:

$$T_B = (1-r)\int_{-\infty}^{0} \left\{2T(z)\ p(z)\ e^{-2\int_z^0 g''(s)ds}\right\}dz \tag{10}$$

where:

$$r = \begin{cases} \left| \dfrac{k\cos\delta - g(0)}{k\cos\delta + g(0)} \right|^2 & \text{, horizontal polarization} \\ \left| \dfrac{\varepsilon_r(0)\, k\cos\delta - g(0)}{\varepsilon_r(0)\, k\cos\delta + g(0)} \right|^2 & \text{, vertical polarization} \end{cases}$$

$$p(z) = \begin{cases} \dfrac{|g(0)|\, g'(z)}{|g(z)|\, g'(0)}\, g''(z) & \text{, horizontal polarization} \\ \left(\dfrac{(k\sin\delta)^2 + |g(z)|^2}{|\varepsilon_r(z)|^2} \right) \dfrac{|g(0)|}{|g(z)|} \dfrac{g'(z)}{g'(0)}\, g''(z) & \text{, vertical polarization} \end{cases}$$

$$g(z) = g'(z) + ig''(z) = k^2 \varepsilon_r(z) - \sin^2\delta$$

In this case, r is the surface reflectivity computed using the dielectric properties at the air-medium interface.

If the assumption is made that the imaginary part of g(z) is small so that $g''(z) \ll g'(z)$, then equation 10 can be reduced further to give the familiar equation (which can be derived directly from radiative transfer principles):

$$T_B = (1-r) \int_{-\infty}^{0} \left\{ 2T(z)\, g''(z)\, e^{-2 \int_{-\infty}^{0} g''(s)\, ds} \right\} dz \qquad (11)$$

That this result can be obtained using WKB solutions is to be expected, since radiative transfer theory is derived from concepts in geometric optics which provide first order solutions to electromagnetic wave propagation in inhomogeneous media (Bekefi, 1966).

For a given dielectric constant profile, equations 10 and 11 can be evaluated directly by numerical integration, or equivalently the medium can be

approximated as being made up of a large number of horizontal layers, within each of which the temperature and dielectric constant are assumed constant. By summing up the contributions from each layer the brightness temperature can be obtained. This approach has been used by Burke et al. (1979). Since propagation of radiation intensities only are considered in the radiative transfer approximation, coherent effects of layers in the medium and rapid profile changes are unaccounted for. This can lead to erroneous results in some cases when computing brightness temperatures from simulated moisture and temperature profiles. In practice, problems may arise where rapid drying in the top centimeter of soil has occurred, resulting in sharp moisture gradients. This is difficult to verify, since measurements of moisture variations within the top centimeter of soil are rather unreliable using currently available techniques. However, for many naturally-occurring moisture profiles, which do not vary too rapidly with depth, the radiative transfer approach should give valid results.

If rough surfaces are to be treated, then modifications must be made in the models for the surface reflectivity r. Valid theoretical expressions for r are in general very difficult to obtain. A simplified model for rough surfaces using the radiative transfer approach has been described by Choudhury et al. (1979).

Coherent Model

As discussed above radiative transfer solutions equivalent to equation 11 can be obtained by stratifying the medium into a large number of horizontal layers. Solutions can similarly be obtained, by stratification, to the precise formulation of equation 1. The difference is that coherent effects of reflections between layers are accounted for. By using a large number of thin

layers, arbitrarily-varying profiles can be approximated to high accuracy, and precise solutions for brightness temperature can be obtained.

The coherent stratified model can be described by reference to figure 2, which shows the medium divided into a large number n of horizontal layers. The lower region t, (extending theoretically to infinite depth), is at a depth from which very little radiation reaches the surface. Hence, it may be approximated as having a constant profile or some easily computed brightness temperature contribution. Within each ℓth layer the permittivity ε_ℓ and temperature T_ℓ have constant values. The derivations of the expressions for brightness temperature are analogous to those for equation 1. They have been described by Tsang et al. (1975), and thus only the results will be provided here.

$$
\begin{aligned}
T_{B_h}(\delta) = \frac{k}{\cos\delta} \sum_{\ell=1}^{N} \frac{\varepsilon_\ell'' T_\ell}{\varepsilon_0} \Bigg(& \frac{|A_\ell \exp(-ik_{\ell z} d_\ell)|^2}{2k_{\ell z}''} \{1 - \exp[2k_{\ell z}''(d_{\ell-1} - d_\ell)]\} \\
& - \frac{|B_\ell \exp(ik_{\ell z} d_\ell)|^2}{2k_{\ell z}''} \{1 - \exp[-2k_{\ell z}''(d_{\ell-1} - d_\ell)]\} \\
& - \frac{[A_\ell \exp(-ik_{\ell z} d_\ell)][B_\ell \exp(ik_{\ell z} d_\ell)]^*}{2ik_{\ell z}'} \{1 - \exp[-i2k_{\ell z}'(d_{\ell-1} - d_\ell)]\} \\
& + \frac{[A_\ell \exp(-ik_{\ell z} d_\ell)]^* [B_\ell \exp(ik_{\ell z} d_\ell)]}{2ik_{\ell z}'} \{1 - \exp[i2k_{\ell z}'(d_{\ell-1} - d_\ell)]\} \Bigg) \\
& + \frac{k}{\cos\delta} \frac{\varepsilon_t'' T_t}{\varepsilon_0} \frac{|T_h|^2 \exp(-2k_{tz}'' d_n}{2k_{tz}''}
\end{aligned}
\tag{12a}
$$

$$T_{B_v}(\delta) = \frac{k}{\cos\delta} \sum_{\ell=1}^{N} \frac{\varepsilon_\ell'' T_\ell}{\varepsilon_0 |k_\ell|^2} (|k_{\ell z}|^2 + k_x^2) \left[\frac{|C_\ell \exp(-ik_{\ell z} d_\ell)|^2}{2k_{\ell z}''} \{1-\exp[-2k_{\ell z}''(d_\ell - d_{\ell-1})]\} \right.$$

$$- \frac{|D_\ell \exp(ik_{\ell z} d_\ell)|^2}{2k_{\ell z}''} \{1 - \exp[2k_{\ell z}''(d_\ell - d_{\ell-1})]\} \qquad (12b)$$

$$+ \frac{|k_{\ell z}|^2 - k_x^2}{|k_{\ell z}|^2 + k_x^2} \left(\frac{[C_\ell \exp(-ik_{\ell z} d_\ell)][D_\ell \exp(ik_{\ell z} d_\ell)]^*}{2ik_{\ell z}'} \{1-\exp[i2k_{\ell z}'(d_\ell - d_{\ell-1})]\} \right.$$

$$\left. \left. - \frac{[C_\ell \exp(-ik_{\ell z} d_\ell)]^* [D_\ell \exp(ik_{\ell z} d_\ell)]}{2ik_{\ell z}'} \{1 - \exp[-i2k_{\ell z}'(d_\ell - d_{\ell-1})]\} \right) \right]$$

$$+ \frac{k}{\cos\delta} \frac{\varepsilon_t''(|k_{tz}|^2 + k_x^2) T_t}{\varepsilon_0 |k_t|^2} |T_v|^2 \frac{\exp(-2k_{tz}'' d_n)}{2k_{tz}''}$$

The notation is explained below:

δ = viewing angle from nadir

k = $2\pi/\lambda = \omega\sqrt{\mu_o \varepsilon_o}$, wave number in free-space, (λ = wavelength, ω = frequency in radians/sec)

ε_o = permittivity of free space

μ_o = permeability of free space

ε_ℓ = $\varepsilon_\ell' + i\varepsilon_\ell''$ = complex permittivity of ℓth layer; ($\varepsilon_\ell/\varepsilon_o$ = dielectric constant of ℓth layer)

T_ℓ = temperature in the ℓth layer

k_ℓ = $\omega\sqrt{\mu_o \varepsilon_\ell}$ = wave number in ℓth layer

$k_{\ell z} = k'_{\ell z} + ik''_{\ell z} = k\sqrt{\varepsilon_\ell/\varepsilon_o - \sin^2\delta}$ = $\hat{z}$ component of wave-number in ℓth layer

d_ℓ = depth below surface of interface between ℓth and $(\ell+1)^{th}$ layers

N = total number of layers

The constants A_ℓ, B_ℓ, C_ℓ, D_ℓ, T_h and T_v are wave amplitudes, and are related to one another by propagation matrices (Kong, 1975; Tsang et al., 1975). It is assumed that the surface of the medium is smooth.

The expressions 12a and 12b have been programmed on the JPL Univac 1108 computer, and require as basic inputs δ, λ, and the profiles ε_ℓ and T_ℓ. An equivalent formulation of the coherent stratified model has been developed independently by Wilheit (1978).

The model described above is most useful for calculations in which high accuracy is required for media with arbitrary profiles. Various concepts such as temperature sensing depth, moisture sensing depth, and effects of different profiles as functions of frequency, polarization and viewing angle can be studied using the model. As yet, only a smooth surface can be treated by the coherent model. Future work is being directed towards the addition of rough surface parameters based on theory and experimental data.

Coherent models are also required to explain the interference effects which occur in emission from layered media. These interference effects were first observed radiometrically in the experiments of Blinn et al. (1972), and were later thought to explain the anomalously low brightness temperatures measured by Skylab over the Utah Great Salt Lake Desert (Ulaby et al., 1975).

In some practical situations, problems may arise with the use of coherent models, due to imprecision in determining the moisture profile. Soil samples collected during field experiments are usually measured for average moisture content in given depth intervals. These measurements are then used to reconstruct as accurately as possible the true moisture profile by linear interpolation, polynomial fitting, etc. Any artificial discontinuities or sharp changes in profile caused by errors in profile reconstruction will be reflected as errors in calculated brightness temperatures, to a higher degree using a coherent model than using an incoherent model such as radiative transfer. Weighing these considerations with the reservations mentioned earlier against using the radiative transfer approach, it is clear that both coherent and incoherent models have their respective merits, and the models should be used with caution as appropriate to each particular circumstance.

Soil Dielectric Properties

The models described in the previous sections all require knowledge of the medium dielectric properties in order to compute brightness temperatures. Since moisture content is the soil parameter measured in the field and to be ultimately determined from the microwave data, relationships between moisture content and dielectric properties must be established. In these relationships soil texture (as determined by the three main components: sand, silt, and clay) plays an important part.

Laboratory measurements of dielectric constant have been made for a number of different soils, usually as a function of moisture content by weight (gravimetric), and at a limited number of frequencies (see for example Cihlar and Ulaby, 1974; Wang and Schmugge, 1978). From these measurements best-fit curves can be derived, some of which have been compared to theoretical and

empirical mixing formulas to understand the effects of the various soil components (Wang and Schmugge, 1978). The effects of the three components (soil, air, water) on the dielectric properties are complex and difficult to measure experimentally, as evidenced by differences between dielectric constant measurements of different investigators and the various mixing formulas. Uncertainties in the moisture-dielectric constant relationships are a significant factor in the overall modeling errors. It has been found that the variability in the relationships between different soil types can be reduced by expressing the moisture content as a percentage by volume (volumetric), rather than gravimetrically. This, however, requires a knowledge of the soil bulk density, which is difficult to measure accurately in the field and may thus add error to the data. More recently, it has been found that the variability due to soil type can also be reduced by relating the soil dielectric properties to the soil water pressure potential, expressed as a percentage of field capacity (Schmugge, 1980). As before, a certain amount of error may be introduced due to the uncertainty in the dependence of field capacity on soil texture. The advantages to be gained are significant however since universal curves for soil dielectric properties, independent of soil texture, may be obtained. There is a continuing need for more laboratory measurements to increase the data base from which reliable curves can be derived.

For illustration, a set of average curves of dielectric constant dependence on volumetric soil moisture content at 1.3 GHz is shown in figure 3. These average curves were derived from measurements on different soil types made by various investigators (Cihlar and Ulaby, 1974). Superimposed on these curves are data points from measurements of sand made independently by Njoku and Kong (1977).

Model Results for Theoretical Profiles

Results using the coherent stratified model to calculate brightness temperature of smooth surfaces with various moisture and temperature profiles have been summarized by Njoku and Kong (1977). Some of the important features will be discussed here. Figure 4 shows six moisture profiles of exponential form, roughly approximating conditions found in nature:

$$\theta(z) = \theta_s + \Delta\theta \frac{(e^{\beta z}-1)}{(e^{\beta d}-1)} \quad ; \; -d \leq z < 0 \qquad (13)$$

$$\theta(z) = \theta(-d) \quad ; \; z \leq -d$$

In these expressions, $\theta(z)$ is the volumetric moisture content expressed in decimal fraction, in percent, θ_s is the surface moisture content, $\Delta\theta$ is the increase in moisture content from the surface to depth d below the surface. The moisture content below depth d is considered to be uniform. Parameters θ_s, $\Delta\theta$, β, and d for the six profiles are given in Table I. To calculate brightness temperatures an exponential temperature profile, $T = 290 + 15 \exp(0.1z)$, is assumed for illustration (figure 5). The calculated brightness temperatures for the frequency range 0.25 to 25 GHz are shown in figure 6. The calculations were performed for $\delta = 0^o$ (nadir viewing), and dielectric constants for sand were used (Njoku and Kong, 1977).

Table I

Illustrative Moisture Profile Parameters

Profile	θ_s	$\Delta\theta$	β, m^{-1}	d, m
1	.30	-.05	10	0.5
2	.15	.10	50	0.5
3	.05	.18	20	0.5
4	.02	.18	5	0.5
5	.02	.10	30	0.5
6	.02	.20	-10	0.5

At the higher frequencies, the surface soil moisture and surface temperature are the factors that primarily determine brightness temperature. At lower frequencies however the moisture content and temperature variations below the surface have an increased effect on the brightness temperature. Thus, for example, profile 5 results in lower brightness temperatures than profile 4 at low frequencies, due to its greater near-surface moisture gradient, even though both profiles have the same surface moisture value. At high frequencies profile 5 results in higher brightness temperatures than profile 4, because the sensing depth is smaller, and the high surface temperature contributes more. These rather subtle combined effects of moisture and temperature profiles are discussed further in the following section on sensing depth. The generally lower brightness temperatures at lower frequencies for all curves in figure 6 are also partly due to the lower soil temperature below the surface as assumed by the model. To show the potential problems with the radiative transfer approach, brightness temperatures for profiles 5 and 6 have

been calculated using the radiative transfer model and compared with precise results using the coherent model (figure 7). It is apparent that below about 4 GHz the radiative transfer result for profile 5 does not account for the sharp curvature in the subsurface moisture profile, and for profile 6, does not show the oscillations caused by the discontinuity in moisture profile slope at 50 cm depth.

Sensing Depth

The results discussed above clearly point to the fact that the lower frequencies respond to moisture and temperature variations at greater depths in the soil than do the higher frequencies. From equation 1 it is evident that the moisture and temperature profiles have independent effects on the brightness temperature (ignoring second-order effects such as the dependence of dielectric constant on temperature). The depths below the surface over which moisture and temperature variations separately affect the emitted radiation are in general related though different. This gives rise to the concept of different moisture and temperature sensing depths.

The temperature sensing depth can be determined for different moisture profiles by studying the temperature weighting functions. These are determined by writing equation 1 in the form:

$$T_B(\delta) = \int_{-\infty}^{0} T(z)\, F\{\varepsilon_r(z),\, \delta\}\, dz \qquad (14)$$

where $F\{\varepsilon_r(z),\, \delta\}$ is the polarization-dependent weighting function, and is determined by the dielectric constant profile $\varepsilon_r(z)$ and viewing angle δ. By normalizing the weighting functions to have unity maximum value they can be compared on the same scale, as is shown for moisture profile 3 (figure 8).

For uniform moisture profiles, the weighting functions would be decreasing exponentials. However, this is not the case for non-uniform moisture profiles. Figure 8 shows that at lower frequencies, the weighting functions for profile 3 increase with depth below the surface to a peak value, and then decrease at greater depths. Thus, for example, 1.0 GHz radiation from a depth of 7 cm, at which the weighting function peaks, is the main contributor to the brightness temperature. The depth from above which (1 - 1/e) of the emitted radiation originates can be defined as the temperature sensing depth, and is obtained by integrating the normalized weighting function to the depth at which a value of 63% of the total integral is obtained, i.e. for sensing depth d_s:

$$\frac{\int_{-d_s}^{0} F\{\varepsilon_r(z), \delta\}\, dz}{\int_{-\infty}^{0} F\{\varepsilon_r(z), \delta\}\, dz} = 0.63 \qquad (15)$$

For an exponential weighting function the sensing depth would correspond to the depth at which the weighting function had decreased to 1/e of its value at the surface. The temperature sensing depths as functions of frequency for moisture profiles 1 to 5 are shown in figure 9. Note that these sensing depths are for sand, and will be somewhat different for other soil types, although the shape of the curves will be qualitatively the same.

Only a fraction of the radiation emitted in the bulk medium actually leaves the surface, the rest is reflected back and/or reabsorbed in the medium. The fraction that leaves the surface is determined by the medium reflectivity, which in turn depends on the dielectric constant variations in

the near-surface region. The question arises as to the depth below the surface over which moisture (i.e., dielectric constant) variations affect the reflectivity, and hence the surface emission. This moisture sensing depth is distinct from the temperature sensing depth, and is of primary interest in remote sensing. It is difficult to obtain a straightforward expression for moisture sensing depth, but some insight can be gained by plotting computed brightness temperatures against the average moisture in different depths of the soil. This has been done for the theoretical moisture profiles 1 to 5, and for three frequencies 0.25, 1.0, 5.0 GHz (figure 10). For each frequency, four curves have been plotted, corresponding to average moisture in depths 0 to 1, 0 to 2, 0 to 5, and 0 to 10 cm. There are five sets of points used to generate the plots corresponding to profiles 1 to 5. Straight line relationships are best obtained at 5 GHz by plotting brightness temperature against average moisture in the 0 to 1 cm layer (or less), whereas at 1.0 GHz it is the 0 to 2 cm layer and at 0.25 GHz the 0 to ~ 8 cm layer that provide the best linear correlations. Despite the limited number of points used to generate these plots, it is clear that the depth providing the best linear correlation with brightness temperature (which may be used to define the moisture sensing depth) is significantly less than the temperature sensing depth.

The conclusion to be drawn from this discussion is that the moisture content within the moisture sensing depth is the appropriate moisture parameter to be derived from microwave remotely sensed data, but in this derivation account must be taken of soil temperature variations within the temperature sensing depth. It is for this reason that we are combining the microwave and thermal infrared approach. The next section discusses the modeling designed to determine the soil temperature and moisture variations as a function of depth from infrared measurements.

A NUMERICAL MODEL FOR HEAT AND MOISTURE FLOW IN SOILS

Equations, Boundary and Initial Conditions

Soil is a mixture of substances that occur in three phases: solid (rock, mineral particles, ice, organic material), liquid (water), and gas (air, water vapor). The flow of heat and moisture in soils is described by a second order partial differential equation of parabolic form, viz.,

$$\frac{\partial U_i}{\partial t} = a_i(\bar{x},t)\bar{\nabla}^2 U_i - 2b_i(\bar{x},t)\bar{\nabla}U_i + c_i(\bar{x},t)U_i - d_i(\bar{x},t), \qquad (16)$$

with $a_i(\bar{x},t) > 0$. For U_i, the subscript i denotes temperature when i = 1 and volumetric water content when i = 2. Actually, the heat and moisture flow equations are coupled through the coefficients a_i, b_i, c_i, d_i which are functions of temperature and moisture (see below). Assuming horizontal homogeneity in the temperature and moisture fields, equation 16 reduces to a one-dimensional form in the vertical ($\bar{x} \cdot \hat{z} = z$) whose solution is uniquely specified when the initial and boundary conditions are given,

$$U_i(z,0) = f_i(z) \qquad (17a)$$

$$U_i(0,t) = g_i(t) \qquad (17b)$$

$$U_i(D,t) = h_i(t). \qquad (17c)$$

Figure 11 shows a block diagram of the soil model that is described by equations 16 and 17. The transport equations pertain to a medium composed of solid material, water, and air. Depending upon the moisture content, the model consists of a medium (water or air) in which soil particles (solid

material and air or solid material and water, are imbedded. For moist soils the medium is water, and for dry soils, air.

The upper soil boundary (z = 0) condition on temperature is prescribed by an energy balance equation

$$R_N = Q_E + Q_S + Q_G$$

where,

R_N = net radiative heat flux,

Q_E = latent heat flux,

Q_S = sensible heat flux,

Q_G = soil heat flux.

Then, equation 17b is expressed as $U_i(0,t) = g_i(R_N, Q_E, Q_S, Q_G)$. Figures 12 and 13 show, respectively, how R_N is partitioned and how each of the fluxes typically behaves day and night. R_N has solar and terrestrial components. For clear skies, R_N (solar) depends, in part, upon the amount of solar radiation incident at the top of the atmosphere, the ground albedo, zenith angle of the Sun, and the amount of atmospheric scattering and absorption. The upward surface flux of R_N (terrestrial) depends only upon the surface temperature when the ground is assumed to be a perfectly black radiator. The downward flux of R_N (sky), or long-wave sky radiation, can be estimated from the near surface temperature and water vapor content. During the day, R_N is generally directed toward the ground while the other fluxes tend to remove either heat or moisture, or both, from the surface. At night, the upward component of R_N (terrestrial) dominates R_N so heat is lost from the surface, while the other fluxes tend to add heat to the surface. The parameterization of R_N, Q_E, and Q_S is given in Appendix I. The calculation of Q_G is given in the section on

heat flux. For moisture, q = E, at the surface. Here q is the moisture flux density in the soil and E is the evaporative flux density.

At the lower boundary (z = D), it is assumed the diurnal variations of heat and moisture do not penetrate that far (D = 2 m). This means the temperature and moisture content are constant at the lower boundary. Therefore,

$$U_i(D,t) = \text{constant}.$$

Moisture Flux

The variation of soil moisture is described formally by equation 16, which is obtained from the requirement of mass continuity,

$$\frac{\partial \theta}{\partial t} = -\overline{\nabla}_z \cdot (\overline{q}/\rho), \tag{18}$$

where ρ is the density of liquid water (= 1 gm cm^{-3}), θ is the volumetric soil water content (fractional volume of water in total volume of soil), and $\overline{q}$ is the moisture flux density,

$$\overline{q} = -\rho(D_\theta \overline{\nabla}_z \theta + D_T \overline{\nabla}_z T + K\hat{z}). \tag{19}$$

D_θ and D_T are the moisture and thermal diffusivities, respectively; both have liquid and vapor components, and both depend upon moisture and temperature variations,

$$D_\theta = (D_\theta)_{liq} + (D_\theta)_{vap}$$
$$D_T = (D_T)_{liq} + (D_T)_{vap}. \tag{19a}$$

K is the hydraulic conductivity (cm/sec). Substituting equation 19 into equation 18 gives

$$\frac{\partial \Theta}{\partial t} = \bar{\nabla}_z \cdot (D_\Theta \bar{\nabla}_z \Theta) + \bar{\nabla}_z \cdot (D_T \bar{\nabla}_z T) + \frac{\partial K}{\partial z} . \tag{20}$$

Expanding equation 20 produces an equation identical to equation 16:

$$\begin{aligned} U_2 &= \Theta \\ a_2 &= D_\Theta \\ b_2 &= -\tfrac{1}{2} (\partial D_\theta / \partial z) \\ c_2 &= 0 \\ d_2 &= -\frac{\partial}{\partial z} (D_T \frac{\partial T}{\partial z}) - \frac{\partial K}{\partial z} . \end{aligned} \tag{21}$$

Note that equation 20 depends upon T as well as Θ. In the next section, a similar equation for the heat flux is developed which also depends upon both T and Θ. This requires that both equations be solved simultaneously. This is shown in a later section.

The parameters D_Θ and D_T are given below. Details concerning their derivation are discussed in Philip and de Vries (1957) and Philip (1957).

Moisture Diffusivity (D_Θ)

The liquid component of the moisture diffusivity is

$$(D_\Theta)_{liq} = K(\Theta) \partial \psi / \partial \Theta \tag{22}$$

where ψ is the capillary potential (cf. Hillel, 1971).

The energy of the soil water is defined by ψ. ψ is a potential function (negative for unsaturated soils) based on a unit weight of water and has the dimensions of length (cm). For a solute-free solution of water, the liquid and vapor phases are related by

$$h = \exp(g\psi/RT)$$

where h is the relative humidity, R is the gas constant of water vapor ($= 4.615 \times 10^6$ erg gm^{-1} $^oC^{-1}$) and g is gravitational acceleration ($= 981$ cm/sec^2).

The inverse of K is a measure of the soil's resistivity to the flow of water. Some of the major factors determining K are the total porosity of the soil, the distribution of soil pore size, soil tortuosity (or pore geometry), fluid conductivity, and fluid viscosity (cf. Childs, 1967). For saturated soils K is constant while it varies with Θ for unsaturated soils. K varies with Θ in a non-linear way: for Θ near saturation and decreasing Θ, the largest pores empty first so that K decreases approximately with the square of the pore radius and K drops rapidly with Θ. When Θ is small, K is low; therefore, the flow of moisture is not very great over a small period of time, e.g. a few hours, unless the gradient in Θ is large.

The variation of K and ψ with Θ has been modelled empirically for a number of soil-types by Clapp and Hornberger (1978). Figure 14 shows curves of K and ψ versus Θ using their models.

The vapor component of the moisture diffusivity is

$$(D_\Theta)_{vap} = D_{atm} v a g \rho_w (\partial\psi/\partial\Theta)/PRT, \qquad (23)$$

where D_{atm} is the diffusivity of air, ν is the ratio of total atmospheric pressure (P) to the partial pressure of dry air, a is the porosity (or volumetric air content in cm^3 of air/cm^3 of total soil volume) and ρ_w the water vapor density.

The elements in equation 23 were given the following values

$$D_{atm} = (5.89 \times 10^{-4} T^{2.3})/P$$

where P is given in mb and T in ^oK (Krishner and Rohnalter, 1940). Values of porosity, a, for different soil types are given in Table II-1, Appendix II. Because the partial pressure of water vapor (e) is ordinarily much less than the total air pressure,

$$\nu = P/(P-e) \cong 1.$$

The water vapor density is obtained from

$$\rho_w = h\rho_s$$

where ρ_s is the water vapor density for saturated conditions,

$$\rho_s = (f_w e_s)/RT,$$

f_w is a correction factor to account for the departure of moist air from ideal conditions (= 0.622) and e_s is the saturation vapor pressure in mb (Saucier, 1955):

$$e_s = (6.11 \times 10^{\alpha}),$$

$$\alpha = (7.5\ T - 2049)/(T-35.9)$$

with T in ^oK.

Thermal Diffusivity (D_T)

The liquid component of the thermal diffusivity is

$$(D_T)_{liq} = K(\partial\psi/\partial T). \quad (24)$$

The derivative can be approximated by

$$\frac{\partial\psi}{\partial T} = \gamma\psi,$$

where $\gamma = -2.11 \times 10^{-3}\ ^{o}C^{-1}$, over the range 10 - 60°C which is appropriate for most conditions. This obtains from: 1) the equation of capillarity,

$$\psi = -2\mu/r$$

where μ is the surface tension of liquid water and r is effective radius of the pore spaces (cf. Hillel, 1971); and 2.) by differentiating ψ with respect to T, i.e.,

$$\frac{\partial\psi}{\partial T} = -\frac{2}{r}\ \frac{\partial\mu}{\partial T}\ .$$

Figure 15 shows that γ is nearly linear between 10 - 60°C,

$$\frac{\partial\psi}{\partial T} = \gamma\psi$$

where $\gamma = A_1/\mu$. At 30°C, $\gamma = -2.11 \times 10^{-3}\ ^{o}C^{-1}$ and over the range 10 - 60°C, γ does not vary from this value by more than 5%.

The vapor component of the thermal diffusivity is

$$(D_T)_{vap} = D_{atm}\nu\alpha h\beta n/\rho_w. \quad (25)$$

The factor β is the coefficient of thermal expansion,

$$\beta \equiv d\rho_s/dt$$

$$= \rho_s\left[\frac{4098}{(T-35.9)^2} - \frac{1}{T}\right],$$

where T is in ^{o}K. Figure 16 shows β versus T between 10^{o} and $60^{o}C$. α is a tortuosity factor = 2/3, (Philip and de Vries, 1957).

The factor η takes into account the interaction of water vapor with the liquid and solid phases in the soil. The simple theory of water vapor transfer in soils assumes $\eta = 1$; calculations of $(D_T)_{vap}$ with this value of η do not agree with experimental results (Philip and de Vries, 1957). When liquid continuity is absent in the soil, moisture transport takes place by a series-parallel arrangement of liquid and vapor movement. Simple theory regards the separate pockets of liquid water as barriers to the vapor flow when, in fact, they offer little resistance to it. It has also been found that the heat transfer through air-filled pores is about twice the rate it is through the soil medium itself. These two considerations will cause $\eta > 1$.

An empirical expression is derived for η based on the work of Philip and de Vries (1957) (Appendix III). Table III-1 in Appendix III shows the variation of η with θ for a sandy clay loam soil.

Appendix II. lists the physical characteristics of several soil types used in the model.

Heat Flux

In unsaturated soils, heat flow is complicated by moisture movement in both the liquid and vapor phases. The diffusion of water vapor from one point in the soil to another is caused by differences in the local vapor pressure

which are engendered by soil temperatue gradients. This creates a latent heat transfer in the soil which results in an enhanced thermal conductivity in the gas-filled, pore space. Furthermore, the vapor movement is accompanied by a distillative process: liquid water evaporates in one place and reforms as a condensate in another place. To account for this, a term is added to the Fourier heat conduction equation, i.e.,

$$C \frac{\partial T}{\partial t} = \bar{\nabla}_z \cdot (\lambda \bar{\nabla}_z T) + Q(\theta, T) \tag{26}$$

where C (Cal cm^{-3} $^oC^{-1}$) is the volumetric heat capacity of the soil, λ (Cal sec^{-1} cm^{-1} $^oC^{-1}$) is the thermal conductivity, and Q is the distillative term. Q is heat transferred from vapor diffusion by moisture gradients and is a heat source (sink) when it is expressed as a convergence (divergence),

$$Q = \bar{\nabla}_z \cdot \left(\rho L (D_\theta)_{vap} \bar{\nabla}_z \theta\right) \tag{27}$$

where L (Cal/gm) is the latent heat of condensation (evaporation). L varies linearly with temperature over the range 0^oC to 60^oC (Smithsonian Meteorological Tables, 1951),

$$L = 597.38 - 0.57\ T$$

where T is in ^oC. In our calculations, we use L = 585 cal/gm over the whole range which amounts to an error in L of not more than 4%.

Expanding equation 26 produces an equation identical to equation 16:

$$U_1 = T$$

$$a_1 = \lambda/C$$

$$b_1 = -\frac{1}{2}\frac{\partial}{\partial Z}(\lambda/C)$$

$$c_1 = 0$$

$$d_1 = -Q(\Theta,T)/C.$$

The thermal conductivity (λ) is computed by the method of de Vries (1963), denoted by DV in the following text. The bulk conductivity of the soil is expressed as a weighted sum of the individual soil components,

$$\lambda = \frac{\sum_{i=0}^{N} k_i x_i \lambda_i}{\sum_{i=0}^{N} k_i x_i} \qquad (28)$$

where N is the number of soil components, x_i is the volume fraction of component i, λ_i is the conductivity of component i, and k_i is the ratio of the average temperature gradient in component i to the temperature gradient in the medium (i=0, either air or water), which can be expressed as:

$$k_i = \frac{1}{3}\sum_{j=a,b,c}\left[1 + \left(\frac{\lambda_i}{\lambda_0} - 1\right)g_j\right]^{-1}. \qquad (29)$$

The expression for k_i is based on the assumption that the soil particles (solid material) are ellipsoidal in shape and that they are spaced sufficiently far apart that their local temperature fields are not distorted by the presence of other particles.

The shape factors (g_a,g_b,g_c) correspond to the axes of the ellipsoids, and their sum is

$$g_a + g_b + g_c = 1.$$

For all calculations with solid material, we use the values $g_a = g_b = 0.125$, $g_c = 0.750$ which were obtained from DV(pg. 217). For water, we assume, that over a certain range, it is the medium in which the soil particles (air, solids) are imbedded so that k_0=1. The range of Θ, over which water is the soil medium, is shown in Table II for different soils. Values for Θ_{sat}, Θ_f, Θ_c are computed from the empirical models of Clapp and Hornberger (1978). The

Table II.

Soil Moisture Volumetric Constants

Soil type	Θ_c	Θ_f	Θ_{sat}
sand	0.020	0.173	0.395
loamy sand	0.024	0.178	0.410
sandy loam	0.041	0.247	0.435
silt loam	0.070	0.367	0.485
loam	0.061	0.312	0.451
sandy clay loam	0.087	0.204	0.420
silty clay loam	0.114	0.356	0.477
clay loam	0.139	0.390	0.476
sandy clay	0.135	0.316	0.426
silty clay	0.175	0.408	0.492
clay	0.185	0.399	0.482

range is from saturation (all pore spaces filled with liquid water, $\theta = \theta_{sat}$) to critical content (value of θ below which liquid continuity is absent, $\theta = \theta_c$). Between these limits, the shape factors for the air-filled pores vary with θ. From DV, we use the following expressions for the g_a of air particles in soil of 30°C, which is representative of mean soil temperatures in arid regions,

$$g_a = 0.333(1 - a/\theta_{sat}) + 0.050\ a/\theta_{sat}, \qquad \theta_f \leq \theta \leq \theta_{sat}$$

$$= 0.0165(1 - \theta/\theta_f) + 0.10\theta/\theta_f, \qquad \theta_c \leq \theta \leq \theta_f.$$

Between θ_{sat} and θ_c, we define θ_f as the volumetric water content at field capacity. Although the term field capacity is applied to the water content at which internal drainage stops, it is not a true physical property of soils and its meaning is arbitrary (Hillel, 1971). For our purposes, we define it as the lower limit, θ_f, of the range ($\theta_{sat} \leq \theta \leq \theta_f$) where the soil air is saturated with water vapor (i.e., h=1.00). The values of θ_f in Table II are calculated by assuming that $\psi_f = -346$cm (cf. Millar et al, 1965). Finally, we calculate k_{air} from the above expression for g_a and the equation, derived from equation 29,

$$k_{air} = \frac{1}{3}\left[\frac{2}{1 + (r-1)g_a} + \frac{1}{1 + (r-1)(1-2g_a)}\right]$$

where $r = \lambda_{air}/\lambda_{water}$ and $\lambda_{air} = \lambda_{dry\ air} + \lambda_{water\ vapor}$.

When $\theta > \theta_c$, λ is calculated from equations 28 and 29; for $\theta < \theta_c$, λ is calculated by linear interpolation between the values of λ for $\theta=0$ and $\theta=\theta_c$. Quite often in dry soils, the ratio λ_i/λ_o exceeds 100. This causes an error

of about 25% in the calculation of λ. Therefore, whenever $\lambda_i/\lambda_0 > 100$, λ computed from equation 28 is multiplied by a factor of 1.25.

In moist soils, heat transfer is affected by: (a) moisture gradients, the Q term in equation 26, and (b) temperature gradients. The last effect produces an apparent increase in the thermal conductivity of the air-filled pore spaces. This must be accounted for in calculating the bulk conductivity of the soil, and is done so by adding the term

$$\lambda_{vapor} = LD_{atm} \nabla h \beta$$

to the value of the air's conductivity, i.e.,

$$\lambda_{air\ pores} = \lambda_{air} + \lambda_{vapor}.$$

The volumetric soil heat capacity (C) is the algebraic sum of the individual components in a unit volume (1 cm^3) of soil. Each volume fraction per unit volume is given by s (solid material of dry soil), θ (water), and a (air),

$$s + \theta + a = 1.$$

The total pore space is defined when the soil is completely dry ($\theta = 0$), and the air-filled pore space varies as a function of θ,

$$a = (1 - s) - \theta.$$

C is the product of soil bulk density (ρ_b) and specific heat capacity (C). (Values of density (ρ_i) and specific heat capacity (C_i) are given in Appendix II, Table II-2 for a number of substances.) The bulk volumetric heat capacity is comprised of the sum of the triple product of each soil constituent,

$$C = \rho c$$
$$= s\rho_s c_s + \Theta c_w + a\rho_a c_a \tag{30}$$

The last term is usually several orders of magnitude smaller than the first two terms and can be neglected.

Numerical Solution of the Equations

The moisture flux and heat flux equations are written,

$$\frac{\partial \Theta}{\partial t} = \frac{\partial}{\partial z}\left(D_\Theta \frac{\partial \Theta}{\partial z} + D_T \frac{\partial T}{\partial z} + K\right) \tag{31}$$

$$C \frac{\partial \Theta}{\partial t} = \frac{\partial}{\partial z}\left(\lambda \frac{\partial T}{\partial z} + Q \frac{\partial \Theta}{\partial z}\right). \tag{32}$$

The parameters A and B are defined as,

$$A = \frac{\partial D_\Theta}{\partial z}\frac{\partial \Theta}{\partial z} + \frac{\partial D_T}{\partial z}\frac{\partial T}{\partial z} - \frac{\partial K}{\partial z} \tag{33}$$

$$B = \frac{\partial \lambda}{\partial z}\frac{\partial T}{\partial z} + \frac{\partial Q}{\partial z}\frac{\partial \Theta}{\partial z} \tag{34}$$

Equations 31 and 32 are then rewritten,

$$\frac{\partial \Theta}{\partial t} = A + D_{\Theta} \frac{\partial^2 \Theta}{\partial z^2} + D_T \frac{\partial^2 T}{\partial z^2} \tag{35}$$

$$C \frac{\partial T}{\partial t} = B + \lambda \frac{\partial^2 T}{\partial z^2} + \frac{\partial^2 \Theta}{\partial z^2} . \tag{36}$$

These equations, coupled through derivatives of Θ and T, are solved by the Du Fort and Frankel method, which is an explicit finite difference technique of unrestricted stability.

A grid is set up in t and z (logarithmic spacing). On the grid, each point is specified by a pair of numbers (z_i, t_j):

$$z_i = hi, \; i = 0, 1, 2 - - - - - N + 1$$
$$t_j = jk, \; j = 0, 1, - - - - - - \quad .$$

The parameters h and j are constants which are defined by the interval (distance) between consecutive periods of time (points in space),

$$h = z_{i+1} - z_i$$

$$k = \Delta t = t_{j+1} - t_j$$

Figure 17 shows the computational molecule for solving equations 35 and 36 on this grid. Note that h is rewritten as

$$h_+ = z_{i+1} - z_i$$

$$h_- = z_i - z_{i-1}$$

$$h_0 = (h_+ + h_-)/2.$$

For a logarithmic grid, the Laplacian at $\Theta_{i,j}$ is approximated by

$$\bar{\nabla}_z^2\Theta \doteq \frac{\frac{(\Theta_{i+1,j} - \Theta_{i,j})}{h_+} - \frac{(\Theta_{i,j} - \Theta_{i-1,j})}{h_-}}{h_0} .$$

The Du Fort-Frankel substitution

$$\Theta_{i,j} = \frac{\Theta_{i,j-1} + \Theta_{i,j+1}}{2},$$

is then substituted in the above equation with the result

$$\bar{\nabla}_z^2\Theta \doteq \frac{h_-\Theta_{i+1,j} - h_0\Theta_{i,j+1} - h_0\Theta_{i,j-1} + h_+\Theta_{i-1,j}}{h_0h_+h_-}.$$

The Laplacian in T is developed in the same way. Therefore, the finite difference forms of equations 35 and 36 are

$$\frac{\Theta_{i,j+1} - \Theta_{i,j-1}}{2k} = A+D_\Theta\left[\frac{h_-\Theta_{i+1,j}-h_0\Theta_{i,j+1}-h_0\Theta_{i,j-1}+h_+\Theta_{i-1,i}}{h_0h_+h_-}\right] \qquad (37)$$

$$+ D_T\left[\frac{h_-T_{i+1,j}-h_0T_{i,j+1}-h_0T_{i,j-1}+h_+T_{i-1,j}}{h_0h_+h_-}\right]$$

$$\frac{C(T_{i,j+1}-T_{i,j-1})}{2k} = B+\lambda\left[\frac{h_-T_{i+1,j}-h_0T_{i,j+1}-h_0T_{i,j-1}+h_+T_{i-1,j}}{h_0h_+h_-}\right] \qquad (38)$$

$$+ Q\left[\frac{h_-\Theta_{i+1,j}-h_0\Theta_{i,j+1}-h_0\Theta_{i,j-1}+h_+\Theta_{i-1,j}}{h_0h_+h_-}\right]$$

These equations are then solved for $\Theta_{i,j+1}$ and $T_{i,j+1}$ subject to a given set of initial and boundary conditions.

DESCRIPTION OF THE EXPERIMENTS

Introduction

The experiments were conducted to establish a satisfactory data base in order to initialize, parameterize, and validate the microwave and thermal models. Three separate objectives were set: (1) to study the microwave (MW) and infrared (IR) radiation emitted from a bare, dry soil, (2) to study the effect of surface roughness on these emissions, and (3) to study these emissions during a drying cycle. Each objective was accomplished in two parts. The first experiment was done during a three week period in 1978, May 1-20, at a test site about 16 miles south of Bakersfield, California. The second experiment was done during a four week period in 1979, April 10 - May 10, at a different site about 8 miles southeast of the first one (see figure 18). Both sites were located on bare agricultural fields. During both experiments, measurements, consisted of: (1) soil microwave emission (using the van radiometers), (2) subsurface temperature and moisture at several depths, (3) micrometeorological factors, e.g., air temperature and humidity, and (4) emissions of soil infrared energy. The equipment used in the experiments and the characteristics of the test sites are described below.

Equipment

Microwave Emission

The JPL microwave radiometry field van is shown schematically in figure 19. The van and equipment were originally used for ground-based radiometer experiments in the early 1970's (Blinn et al., 1972), and have been upgraded since then for the present soil moisture applications. There are three dual-polarized Dicke-type radiometers operating at center frequencies of

0.6 to 0.9 GHz (tunable), 1.42 GHz and 10.69 GHz. The two lower-frequency radiometers share a 2.4 m parabolic reflector antenna, while a lens-loaded circular horn is used for 10.69 GHz. The radiometer and antenna characteristics are summarized in Table III.

Table III. Radiometer and Antenna Characteristics

Center Frequency, GHz	0.6-0.9	1.42	10.69
Wavelength, cm	50-33	21	2.8
Bandwidth, MHz	30	220	220
Polarization	V,H	V,H	V,H
Integration time, s	2	2	2
RMS sensitivity, K	0.3	0.6	0.3
Antenna type	2.4 m parabolic reflector (log-periodic feed)		Lens-loaded horn

The radiometer/antenna system is calibrated by a two-point external calibration: viewing clear sky and then microwave absorber at ambient temperature placed in front of the antennas. In addition, instrument temperatures are monitored during the experiment and, together with prior knowledge of the component losses, are used to calibrate the effects of instrument temperature and gain variations during the experiment. Short-term calibration of the radiometers alone is accomplished by switching between two internal reference loads. It is estimated that an absolute antenna temperature accuracy of 3 K is achievable by this method.

The radiometers and antennas are positioned by a hydraulically operated boom assembly mounted on the front of the van. Under normal operating condi-

tions the antennas are positioned 3.7 m above ground level and 4.6 m from the front of the van. This places the viewing target in the far field of the horn antenna but in the near field of the parabolic dish. The viewing angle can be continuously varied from 25 deg off nadir to zenith. The van contains the radiometer controls and data processing electronics, including a PDP/8L computer for real-time data reduction. Printed output consists of raw data, calibration data, and calibrated antenna temperatures. The data is also stored on computer-compatible tape for further processing. The antenna temperatures at this stage are not corrected for antenna pattern effects. A backup system prints out raw data on paper tape, and in addition, the radiometer output levels are displayed continuously on strip chart recorders. A functional block diagram of the system is shown in figure 20.

The microwave van is fully mobile and self-contained. In field operation the equipment is powered by two 4-kilowatt generators. Over short distances the van can travel with the antennas in the deployed position (figure 21) while for longer distances, the 2.4 m antenna is removed and towed on a separate trailer, with the hydraulic boom folded back on top of the van.

Subsurface Temperature and Moisture

In the 1978 experiments subsurface measurements were taken at two to four sites on each plot. All temperatures were measured at depths of 3, 8, 15, 25, 40, and 50 cm. The latter reading was obtained at just a few sites in order to mark the lower limit of the diurnal heating wave. Soil samples were obtained by the gravimetric method. Cylindrical coring devices were used to obtain samples at 0-2, 2-5, 5-9, 9-15, and 15-30 cm depths; the samples were placed in paper cups, sealed, dried in a 1000-watt microwave oven, and weighed before and after drying to ascertain moisture content. Temperature measure-

ments and soil samples were taken more frequently during the first week than during the remainder of the period. Soil temperatures were measured on an almost hourly basis from 0500 to 2100 LT with an additional measurement at 0100. Soil samples were taken about every three hours. After the first week, temperature measurements were scheduled less frequently (10 times per day) and mostly during the daylight hours; soil moisture samples were collected 3 times per day (0500, 1400, 2100 LT). Similar procedures for soil sampling were followed in the 1979 experiments, except that the moisture content samples were obtained somewhat more frequently than in 1978, and a specially-designed trowel was used in order to obtain the samples more accurately in the upper soil layers. Complete descriptons of the data gathering procedures and schedules, including site descriptions and a list of all soil temperature and moisture measurements, are included in the reports on the experiments written by the Geography Remote Sensing Unit of the University of California at Santa Barbara (O'Neill and Atwater, 1978; Atwater and O'Neill, 1979).

Micrometeorology

The wind speed, air temperature, and humidity were obtained at several different altitudes over an 8-meter layer above the surface. Two portable weather stations were set up. The JPL Micrometerological Mast (Kahle et al, 1977) measured wind speed, dry-bulb air temperature, and wet-bulb air temperature at the 1/8, 1/4, 1/2, 1, 2, 4, and 8 meter levels. The data were 16-minute averages. A mechanical weather station (manufactured by Meteorology Research Inc.) was located near the JPL Mast and continuously recorded dry-bulb air temperature, relative humidity, wind speed, and direction at a 2-meter height. Sensible and latent heat fluxes at the surface were calculated as a function of time from both data sets by means of the methods described in

Appendix I. Additionally, the net radiation flux and the soil heat flux at the surface were monitored throughout the experiment by a Thornthwaite net radiometer-recorder and a soil heat flux sensor-recorder, respectively.

Infrared Emission

The IR measurements were obtained concurrently with the sub-surface temperature measurements. Either a Barnes PRT-5 Radiation Thermometer or a Barnes Instatherm Radiation Thermometer was used to measure the IR surface emission (8-14 μm) as an equivalent black-body temperature. Both instruments measured temperatures to within 0.5°C accuracy.

1978 Experiment

The weather during the 1978 experiment was characterized by warm days and cool nights with mostly clear skies. The average air temperatures ranged from a maximum of 30°C to a minimum of 15°C. No rain fell at the test site, although Bakersfield recorded 0.02 inch on May 1 and no precipitation the rest of the period. The test site was a flat fairly homogeneous agricultural field bounded on the south by an asphalt road and on the north, east, and west by vegetable crops (see figure 22). The soil was a sandy clay loam composed of 49% sand, 28% silt, and 23% clay. The micrometeorological instruments were located on the south side of the site, while two plots about 20 by 20 meters square were set aside on the north side for the MW and IR measurements.

During the first week, one plot was prepared by smoothing and tamping the surface. This was done to study the radiative characteristics of the MW-IR emissions over a 48-hour period. For the second week, both plots were kept dry but their surfaces were altered. First, they were ploughed into small furrows (about 0.16 meters high from trough to crest and with "wavelengths,"

crest to crest, of about 0.9 meter). The furrows on one plot ran north to south, while on the other they ran east to west. Next, after a series of measurements, both were ploughed into large furrows (0.32 m high and 1 m wavelength), again with north-south and east-west orientations. To conclude the surface roughness studies, both plots were reploughed to produce two surfaces of random roughness with large clods of soil (10-15 cm in size) covering one plot and small clods (5-7 cm in size) covering the other. Finally, the plots were wetted for 7 hours and then allowed to dry so that the effect of the moisture changes on the radiative emissions could be observed. One plot was prepared with east-west furrows about 0.20 meters high and with a wavelength of about 0.9 meter. The other was maintained as a relaively smooth surface. Some problems developed during this phase and it proved difficult to wet the surfaces uniformly. In particular, the crests dried more rapidly than the troughs in the furrowed plot and the smooth plot was spotted with a few dry areas. The experimental data are reported in detail in O'Neill and Atwater (1978).

1979 Experiment

The objective of the 1979 experiment was to study the drying cycle of two surfaces with different roughness characteristics, but with the same soil composition. One surface was initially rough and the other smooth. Ostensibly, the effects of surface roughness and soil moisture content were to be examined separately so that the variation of soil moisture content on the strength of the microwave emissions could be studied in detail. The weather during the 1979 experiment was generally warm and dry with occasional periods of cloudiness and drizzle or light rain. The temperature range varied from a maximum of about 30°C to a minimum of about 7°C. The location of the test

site was near the windward (western) side of the Tehachapi Mountains and this factor probably contributed to the occurrence of intermittent sprinkles there. Not enough precipitation fell to cause any delay in proceeding with the experiment. The test site was a section of field on the Tejon Ranch (figure 23). The soil was a sandy loam with a composition of 65% sand, 19% silt, and 16% clay. Two adjacent plots were prepared with clods randomly distributed on the surface: one plot was covered with clods about 5 to 15 cm in diameter and the other with clods less than 5 cm in diameter. The plots were irrigated by a sprinkler system until the soil was saturated to a depth of about 30 cm. As in the previous experiment, some ponding of water occurred in small depressions on the surface, and these were filled in with loose soil to allow the surface to dry uniformly. Furthermore, both plots became smoother as the experiment progressed, particularly the rough plot, because of the effects of wind and occasional rain. By the end of the four weeks, weeds several cm in height had spread over most of the field. Despite these problems, the data were of a uniformly good quality. A detailed description of the experiment is contained in the final ground truth data report of Atwater and O'Neill (1979).

EXPERIMENTAL RESULTS

Microwave

Introduction

The data measured using the JPL microwave van radiometers during the 1978 and 1979 field experiments were obtained at nominal viewing angles of 25°, 35°, and 45° from nadir, vertical and horizontal polarizations, and frequencies of 10.69 GHz, 1.42 GHz, and UHF. The tunable UHF radiometer affords some degree of frequency selectivity to avoid radio-frequency interference (RFI). In the 1978 experiments the frequency chosen was 0.85 GHz (35.3 cm wavelength), but significant amounts of RFI were unavoidable. Subsequently most of the 1978 UHF data had to be discarded. In the 1979 experiments, a narrowband (30 MHz) filter was added, and the radiometer was operated at 0.775 GHz (38.7 cm wavelength). This proved to be a major improvement and the majority of the 1979 data were RFI-free.

The microwave and ground truth data analysis has proceeded in two parts. The first part has been a comparison of the measured microwave brightness temperatures with brightness temperatures calculated from a theoretical model using ground truth data as inputs. The second part has been a direct correlation of the microwave data with ground truth measurements of the soil moisture content at specific depths. Initial results of this latter work have been reported by O'Neill (1979).

Comparison of Observed and Calculated Brightness Temperatures

In order to establish the validity of the theoretical models, calculations of brightness temperature based on these models were compared directly with brightness temperatures measured by the microwave van radiometers. Only

data from the 1979 smooth fields have been included in the initial comparisons, and the coherent model (discussed in a previous section) was used in the theoretical calculations.

The ground truth measurements of moisture content and temperature were made daily at different times. These times were interpolated to the same times as the radiometer measurements, for use in the brightness temperature calculations. Continuous depth profiles of moisture and temperature were generated from the ground truth data by piecewise polynomial fits. Figure 24 shows typical moisture profiles generated from the ground truth measurements. The measurements represent averages over depths of 0 - 2, 2 - 5, 5 - 9, 9 - 15, and 15 - 30 cm. Continuous profiles generated from these averaged data may deviate somewhat from the true profiles. This is especially the case for the near-surface region where the moisture profile gradient is an important parameter, and errors may be introduced into the comparisons due to incorrect determination of this near-surface gradient. The smooth fields had a residual roughness ($\lesssim$ 2 cm rms height variance), which had some effect on the measurements, especially at 10.69 GHz. Approximate dielectric constants for use in the calculations were obtained from soil dielectric data compiled by Wang and Schmugge (1978), using soil types which closely approximated the textural composition of the Bakersfield soils.

Figure 25 shows the results of plotting the observed vs. calculated brightness temperatures for the three frequencies: 0.775, 1.4 and 10.69 GHz, at vertical and horizontal polarization. Each plot includes data over a range of viewing angles between 20° and 45° from nadir. Since the fields were fairly smooth, good agreement with the smooth surface model was expected (i.e., plotted points should lie along a 45° line). The 0.775 and 1.4 GHz vertical polarization data plots (a) and (c) show good linearity. The slope is greater

than 45° however, indicating that for high moisture contents the calculations are somewhat overestimating the T_B's. It is also possible that the calibration of the radiometers has an offset bias at low brightness temperatures which would alter the slope of the comparisons. This possibility is being investigated, and will be further checked in the forthcoming 1980 experiments. At 10.69 GHz vertical (e) the scatter is greater and the slope somewhat nonlinear, possibly due to the fields appearing rougher at this shorter wavelength. Similar features are evident in the horizontal polarization comparisons (b), (d) and (f), although in these cases the scatter is greater than for the vertical. For off-nadir angles the soil surface is more reflective at horizontal than at vertical polarization, and thus is more sensitive to modeling errors caused by neglecting roughness and small atmospheric contributions. This may explain the larger scatter observed in the horizontal data plots. It is also quite probable that a number of the high observed points at 0.775 GHz horizontal in particular, may be due to low-level radio-frequency interference (RFI) from local area transmitters. Considering the complexity of the modeling problem, the agreement exhibited by the plots of figure 25 is reasonable. This agreement was obtained as plotted for a wide range of conditions: (1) moisture profiles, with surface moisture contents ranging from 3% to 15% by volume; (2) temperature profiles, with surface temperatures ranging from 14°C to 48°C; and (3) viewing angles of 20° to 45° from nadir. Future work will generate similar comparisons using a radiative transfer model to determine whether uncertainties in the near-surface moisture profile are adversely affecting the coherent model results.

Comparison of Measured T_B with Moisture in the Top 2 cm

In figures 26, 27, and 28 the measured brightness temperatures have been plotted against average moisture in the top 2 cm of soil. It is expected that a decrease in measured T_B should occur as a function of increasing moisture content. However, these comparisons neglect variations in soil temperature, hence plots of T_B vs. moisture will show some scatter due to these variations. Figure 26 shows the results of the 1978 smooth field experiment at viewing angles from nadir of: (a) 25°, (b) 35°, (c) 45°. The notations LH and LV refer to the L-band (1.4 GHz) horizontal H and vertical V channels, and similarly XH and XV refer to the X-band (10.69 GHz) channels. No data are displayed for the 1978 UHF radiometer channels UH and UV since they were contaminated by RFI. The 1978 data were measured during the night in the hopes of avoiding RFI, thus the soil temperature variations during the measurement period ranged only between about 7° and 25°C. The T_B points thus show good correlation with decreasing moisture content. No data points were obtained between moisture contents of 8 and 14 percent due to the short duration of the experiment. The slope of T_B with decreasing moisture content is fairly linear in the L-band case, except for the points clustered at the low moisture content end. A knee in such curves at low moistures has been observed by other investigators, and the hump may be contributed to by temperature effects in the dry field. The X-band data show a smaller slope, with a knee extending to higher moisture contents. The step-like appearance is artificial, however, and may be caused by ground truth sampling problems. The 10.69 GHz antenna footprint is less than a meter in diameter as compared with the approximately 3 m diameter of the 1.4 GHz antenna footprint. For the higher moisture contents, the water tended to collect in localized areas. Hence, the

ground truth moisture averages for the entire field may not have been a good representation of the soil moisture viewed by the narrow 10.69 GHz antenna beam. It is clear, however, that the sensitivity of X-band to moisture content is much less than at L-band, as evidenced by the smaller overall slope. Of all the plots, the greatest slope (i.e., sensitivity) is shown by the LH channel at 25°. However, the disadvantage of operating at a viewing angle too close to nadir is that little can be gained from using H and V polarizations to obtain roughness information when viewing rough fields.

The smooth field data from the 1979 experiment are shown in figure 27, including data from the UHF radiometers operating at 0.775 GHz. More scatter is evident in these data than for 1978, probably due to two reasons: (1) the microwave data were measured throughout the day, during which time surface temperature variations of about 14 to 48°C typically occurred. (2) In order to speed up the data taking procedure, less time was spent in positioning the antennas at precise angles of 25°, 35°, and 45°. Instead, viewing angles were clustered approximately around three angles as shown in figure 29. The accuracy of the viewing angle determination itself was estimated at about a half a degree.

At L-band the general slope is about the same as for the 1978 experiment, except that a smaller range of moisture was obtained in 1979. This was no doubt due to the higher clay content of the 1978 fields. The knee is not particularly evident at L-band but is visible at about 7 percent moisture in the X-band data. The UHF data appear to exhibit a knee in the opposite direction, i.e., the slope is steeper for moistures less than 7 percent than for moistures above 7 percent, although there are unfortunately fewer points at the high moisture values. The non-linearities in slope are explainable on the

basis of the calculated results shown in figure 10. The slopes are most linear for 1.0 GHz (figure 10(b)) when plotted vs. moisture in the 0 - 2 cm depth. At lower frequencies, however (e.g., 0.25 GHz, figure 10(a)), the 0 - 2 cm curve shows a much steeper slope below the 8 percent moisture level. Conversely, the 0 - 2 cm curve for higher frequencies (figure 10(c)) shows a decrease in slope at low moistures. These non-linearities indicate the need to find appropriate moisture sensing depths for each frequency to obtain the best linear correlations of brightness temperature with moisture content.

The rough field data from 1979 are shown in Figure 28. When initially ploughed, the field had surface clods of approximately 5 - 15 cm dimensions. However, after irrigating the field with sprinklers, and on further weathering of the surface during the experiments, the rough field became almost as smooth as the smooth field (which itself was not quite smooth). For this reason the data in figure 28 look very similar to those in figure 27. Another difference in the two data sets was that measurements of the smooth fields were always made in the morning between 9:00 A.M. and 11:00 A.M., and the rough fields were observed in the afternoon between 2:30 P.M. and 4:30 P.M. In order to study roughness effects adequately, future experiments will be performed on soils with higher clay content so that the rough surface clods will be more likely to retain their sizes without weathering for the duration of the experiment. Further analysis of the 1978 and 1979 data sets is currently in progress to quantify the roughness effects.

Infrared

The numerical model for heat and moisture flow in soils predicts the temperature and moisture history of the soil from a given set of initial and

boundary conditions. The results given below pertain to a three day period during the third week of the 1978 experiment when the soil had been wetted and was in the process of drying. The model predictions are compared with the field observations.

The initial soil temperature and moisture profiles and the near-surface, meteorological boundary conditions are shown in figures 30 and 31. The initial conditions (figure 30) are for May 17, 1978 at 0100 LT (Local Time). Initial conditions from the surface to 0.5 m are obtained from field measurements (cf. previous section); from 0.5 m to the lower boundary at 2.0 m, initial conditions are obtained by extrapolation. The temperature profile is assumed to be isothermal below 0.5 m. The moisture profile from 0.5 to 2.0 m is obtained by connecting a straight line between the 0.5 m measurement and the 2.0 m value of 0.20 cm^3/cm^3 which is assumed to be constant with time.

Figure 3 shows the meteorological conditions at a height of 2 meters above the surface. The sensible and latent heat fluxes are important components of the surface boundary conditions and they are calculated from the meteorological conditions shown here. The sensible heat component is dominant when the soil is dry; conversely, when the soil is nearly saturated, the latent heat component is more important. Then, latent heat not only supplies most of the daytime surface heat loss, but also it modulates the distribution and the rate of change of soil moisture in the near-surface layers.

The observations of the soil temperature and moisture content are shown in figures 32 and 33. The temperature values represent measurements at six discrete levels: 0.00, 0.03, 0.08, 0.15, 0.25, and 0.40 m. The moisture content values are measurements of five layers of different thicknesses: 0.00 - 0.02, 0.02 - 0.05, 0.05 - 0.09, 0.09 - 0.15, 0.15 - 0.30 m. (The 0.15 -

0.30 m measurement at 0900 LT on May 18 in figure 33 is anomalous and probably an error.) The drying trend is evident in both figures. The temperature curves show an increase in the diurnal maxima and minima as the soil dries. The difference between maxima and minima also increases but this effect is not as pronounced at the lower depths. This is because: (1) the thermal inertia of water is higher than that of dry soil, and the lower layers contain more moisture than the upper ones; and (2) the diurnal heating wave does not penetrate very effectively to these depths. Note that the 0.4 m temperature curve has a small variation ($\leq 2^{o}C$) in amplitude which supports the argument that the damping depth of the diurnal heating is about 0.5 m.

The results of the modeling are shown in figures 34 and 35. The computed temperatures correspond quite well with the observations, although they have somewhat higher values than them. The trends are also similar. In both sets of curves, there is a phase lag that increases with depth between the surface and lower level values.

The moisture curves show less specific agreement. This is expected since model results pertain to discrete levels and observations represent moisture content in layers of finite thickness. Moreover, soil moisture content measurements are inherently more difficult to make than soil temperature measurements, and therefore they exhibit quite a bit of variability. Nonetheless, the general trends are alike. Both show the migratory character, denoted by the series of maxima and minima superimposed on the decreasing trend line, of the near-surface moisture regime. In these layers, a moisture gradient directed toward the surface usually exists. During the day, more moisture is lost from the upper layers, by evaporation to the atmosphere, than is gained from below. The result is a net loss of moisture with a minimum in

moisture content occurring in the evening hours. At night, evaporative losses are usually small and moisture migrates toward the surface with a maximum in moisture content occurring in the mid-morning hours. The model results show this effect to be severely damped with depth, but the observations indicate otherwise. This discrepancy is probably due to the simple parameterization scheme that is used in the model to describe the evaporation process.

The variation of temperature and moisture profiles with time is shown in figures 36 and 37. These are results of the modeling. For the 20 hour period, the moisture curves show less change than the temperature curves. Both exhibit greater variability near the surface than at lower depths. The temperature range is about 30°C at the surface and only 4°C at 0.4 m. The moisture content varies by about 0.02 cm^3/cm^3 at the surface and hardly varies at all at 0.4 m. Again, the moisture curves illustrate the migration of water toward the surface with a maximum occurring at night.

Finally, figures 38, 39, and 40 show profile variations of the hydraulic conductivity (K), and the moisture (D_θ) and thermal (D_T) diffusivities. All three elements determine the soil-moisture flux density (see equation 19). Note that the scales are different for each diagram. K is mainly a function of soil-moisture content (θ) and shows a decrease with time. D_θ drives moisture toward the surface in the upper layers, and does not vary much in the lower layers. The powerful influence of evaporative forcing is evident in the profile at 1400 LT. D_T varies widely in the dry, upper layers. Under such conditions, the vapor component of D_T becomes important, whereas, at lower, more moist depths, D_T depends more on the liquid component.

When θ drops below a critical value, θ_c, liquid continuity is not present in the soil and the vapor component of D_T is scaled with respect to ξ, as

discussed earlier. We have tried two values of ξ in all our calculations: first, ξ is assumed to be constant with a value representative of moist soils; second, ξ is calculated by the method of Appendix III so that its dependency upon θ is taken into account. Neither calculation gave significantly different results. Therefore, there seems to be no advantage in calculating ξ for soil-moisture studies of this kind.

Although the results described above are fairly good, we are continuing to refine the soil heat-moisture model. Improvements are being made in parameterizing the surface boundary conditions, especially the heat transfer by sensible and latent processes and the moisture transfer by evaporation. Currently, these elements are computed by use of an algorithm that employs meteorological measurements made at one height above the ground. A calculation of this sort is not generally as accurate as one that is obtained by an algorithm employing meteorological measurements made at several levels (see Appendix I). The latter kinds of calculations are now being incorporated into the model. Further experiments are planned to test the efficiency of the Du Fort-Frankel numerical algorithm by comparing it with other numerical techniques such as the method of lines, and the solution of diffusion-type equations through the use of spline functions.

FUTURE WORK

During 1978 and 1979 separate efforts were made to develop (1) microwave soil emission models, and (2) models for heat and moisture flux in soils. The joint field experiments which took place in each of these two years enabled data to be collected for verification and refinement of the respective models. These data were collected by microwave, infrared, and meteorological equip-

ment, and by ground truth sampling of soil moisture content, temperature, and texture. Although the data sets have been presented and analyzed separately in this report, this is only a first step in the joint project. Once the models have been individually verified, the objective is to use the microwave and flux models together to arrive at an improved technique for remotely determining soil moisture.

As a general approach, the microwave model can be expressed as:

$$T_B(\delta, p, \nu, t) = \int_{-\infty}^{0} T(z,t)\, F\{\varepsilon(\nu,z,t), \delta, p\}\, dz \qquad (39)$$

where the brightness temperature can be measured with variable viewing angle δ, polarization p, frequency ν, and time t. The integrand involves the soil temperature T (z,t) which varies with depth z and time t, and a function F of the soil dielectric constant ε, viewing angle, and polarization. The dielectric constant is itself a function of frequency, depth, and time, and can be related to the soil moisture profile θ (z,t) through a modeled function H:

$$\varepsilon(\nu, z, t) = H\{\theta(z,t), \nu, S\} \qquad (40)$$

where S denotes the dependence of the relationship on soil type. The heat and moisture flux models impose a constraint on the independent variability of the moisture and temperature profiles. This constraint can be expressed generally by a function W, so that:

$$T(z,t) = W\{\theta(z,t), S, E\} \qquad (41)$$

where E represents environmental conditions which affect moisture and heat fluxes across the air-soil boundary.

Analytic inversion of equations 39 and 40 is considered infeasible. However, with a sufficient amount of representative experimental data, empirical or regression techniques may be used to derive a moisture parameter retrieval function G, so that:

$$\theta_o(t) = G\left\{T_B(\delta, p, \nu, t), T_S(t)\right\} \qquad (42)$$

In this expression, θ_o might be the average moisture in a given depth or the moisture gradient for example. The function G would operate on the brightness temperatures and surface temperature (if available), and can be derived using the constraint of equation 41. If other environmental conditions can be determined a priori, e.g., soil type if location is known, then these can be included in the function G. The data sets obtained during the 1978 and 1979 experiments, together with results from the current 1980 experiments, will enable initial steps to be taken in the general approach outlined above.

ACKNOWLEDGEMENTS

Several people have contributed to the experimental work and data analysis described herein. Nob Yamane was responsible for coordinating the successful operation of the microwave field van and radiometers. Eva Kuiper performed much of the microwave data calibration and model calculations. Ron Alley wrote and implemented the computer model for heat and moisture flow in soils. Warren Rachwitz and Richard Machida maintained the micrometeorological instruments, and Mr. Rachwitz also helped with the field work. Peggy O'Neill and Sue Atwater of the Geography Remote Sensing Unit, U.C. Santa Barbara, were responsible for the experimental field site preparations, surface truth data collection and data analysis. Helen Paley carefully read the manuscript, and James Conel reviewed it.

REFERENCES

Atwater, S. G. and P. E. O'Neill, Ground truth data report: 1979 Kern County, California microwave/thermal-infrared soil moisture experiment, Final Report, JPL Contract No. 955032, Geography Remote Sensing Unit, University of California, Santa Barbara, October 1979.

Bekefi, G., Radiation Processes in Plasmas, John Wiley & Sons, New York, 1966.

Blinn, J. C., J. E. Conel, and J. G. Quade, Microwave emission from geologic materials: Observations of interference effects, J. Geophys. Res., 77, pp. 4366-4378, 1972.

Burke, W. J., T. Schmugge, and J. F. Paris, Comparison of 2.8- and 21-cm microwave radiometer observations over soils with emission model calculations, J. Geophys. Res., 84, pp. 287-293, 1979.

Businger, J. A., J. C. Wyngaard, Y. Izumi, and E. F. Bradley, Flux-Profile relationships in the atmospheric surface layer, J. Atmos. Sci. 20, pp. 181-189, 1971.

Childs, E. C., Soil moisture theory, Advan. Hydroscience, 4, pp. 73-117, 1967.

Choudhury, B. J., T. J. Schmugge, A. Chang, and R. W. Newton, Effect of surface roughness on the microwave emission from soils, J. Geophys. Res., 84, pp. 5699-5706, 1979.

Cihlar, J., and F. T. Ulaby, Dielectric properties of soils as a function of moisture content, RSL Tech. Rep. 177-47, Univ. of Kansas Center for Res. Inc., Lawrence, 1974.

Clapp, R. B., and G. M. Hornberger, Empirical equations for some soil hydraulic properties, Water Resourc. Res., 14, pp. 601-604, 1978.

Clark, S. P., Handbook of Physical Constants, Geol. Soc. of Amer., New York, 1966.

Davis, S. N., and R. J. De Wiest, Hydrogeology, John Wiley & Sons, New York, 1966.

deVries, D. A., Simultaneous transfer of heat and moisture in porous media, Trans. Amer. Geophys. Union, 39, pp. 909-916, 1958.

deVries, D. A., Thermal properties of soils, Physics of Plant Environment, Edited by W. R. van Wyk, Wiley, New York, pp. 210-223, 1963.

Eagleman, J. R., and W. C. Lin, Remote sensing of soil moisture by a 21-cm passive radiometer, J. Geophys. Res., 81, pp. 3660-3666, 1976.

England, A. W., Thermal microwave emission from a half-space containing scatteres, Radio Science, 9, pp. 447-454, 1974.

Glinka, K. D., Treatise on Soil Science, Translation by the Israel Program for Scientific Translation, LTD., Jerusalem, 1963.

Glossary of Geology, Edited by M. Gary, R. McAfee Jr., and C. Wolf, Amer. Geol. Inst., Washington, D. C., 1972.

Gustafson, A. F., Soils and Soil Management, McGraw-Hill, New York, 1941.

Hillel, D., Soil and Water, Academic Press, New York, 1971.

Ingersoll, L. R., O. J. Zobel, and A. C. Ingersoll, Heat Conduction with Engineering, Geological, and Other Applications, U. of Wisconsin Press, Madison, 1954.

Iribarne, J. V., and W. L. Godson, Atmospheric Thermodynamics, D. Reidel Publishing Company, Dordrecht, Holland, 1973.

Kahle, A. B., A simple thermal model of the earth's surface for geologic mapping by remote sensing, J. Geophys. Res., 82, pp. 1673-1680, 1977.

Kahle, A. B., J. Schieldge, and H. N. Paley, JPL Field Measurements at the Finney County, Kansas, Test Site, October 1976: Meteorological Variables, Surface Reflectivity, Surface and Subsurface Temperatures, JPL

Publication 77-1, Jet Propulsion Laboratory, California Institute of Technology, Pasadena, Calif., 1977.

Kondratyev, K. Ya., Radiation in the Atmosphere, p. 562, Academic Press, New York, 1969.

Kong, J. A., Theory of Electromagnetic Waves, Ch. 4, Wiley-Interscience, New York, 1975.

Krischer, O., and H. Rohnalter, Warmeleitung und Dampfdiffusion in feuchten Gutern, V.D.I. Forschungsheft, 402, 1940.

Manabe, S., and F. Moller, On the radiative equilibrium and heat balance of the atmosphere, Mon. Weather Rev. 89, 503-532, 1961.

McFarland, M. J., The correlation of Skylab L-band brightness temperatures with antecedent precipitation, Proc. Conf. Hydrometeorol., Fort Worth, Texas, 1976.

Meneely, J. M., Application of the Electrically Scanning Microwave Radiometer (ESMR) to classification of the moisture condition of the ground, Earth Satellite Cooporation, Final Report, Contract NAS5-22328, Washington, D.C., 1977.

Millar, C. E., L. M. Turk, and H. D. Foth, Fundamentals of Soil Science, John Wiley & Sons, New York, 1965.

Newton, R. W., Microwave remote sensing and its application to soil moisture detection, Tech. Report RSC-81, Remote Sens. Center, Texas A & M Univ., College Station, Texas, 1976.

Njoku, E. G., and J. A. Kong, Theory for passive microwave remote sensing of near-surface soil moisture, J. Geophys. Res., 82, pp. 3108-3118, 1977.

O'Neill, P. E., Ground-based microwave radiometric measurements of soil moisture under bare field conditions in the southern San Joaquin Valley,

M. A. Thesis, Dept. of Geography, University of California, Santa Barbara, December 1979.

O'Neill, P. E. and S. G. Atwater, Ground truth data report: 1978 Kern County, California microwave/thermal-infrared soil moisture experiment, Final Report, JPL Contract No. 955032, Geography Remote Sensing Unit, University of California, Santa Barbara, July 1978.

Peake, W., Interaction of electromagnetic waves with some natural surfaces, IRE Trans. Antennas Propagat., AP-7, pp. S324-S329, 1959.

Philip, J. R., Evaporation and moisture and heat fields in the soil, J. Meteorol., 14, pp. 354-366, 1957.

Philip, J. R., and D. A. deVries, Moisture movement in porous materials under temperature gradients, Trans. Amer. Geophys. Union, 38, pp. 222-228, 1957.

Poe, G., A. Stogryn, and A. T. Edgerton, Determination of soil moisture content using microwave radiometry, Final Report 1648 FR-1, DOC contract O-35239, Aerojet General Corp., El Monte, Calif., 1971.

Saucier, W. J., Principles of Meteorological Analysis, University of Chicago Press, Chicago, 1955.

Schmugge, T., Effect of soil texture on the microwave emission from soils, NASA Tech. Memo 80632, Goddard Space Flight Center, Greenbelt, MD, 1980.

Schmugge, T. J., P. Gloersen, T. Wilheit, and F. Geiger, Remote sensing of soil moisture with microwave radiometers, J. Geophys. Res., 79, pp. 317-323, 1974.

Schmugge, T. J., T. Wilheit, W. Webster, and P. Gloersen, Remote sensing of soil moisture with microwave radiometers II, NASA Tech. Note TND-8321, Washington, D. C., 1976.

Smithsonian Meteorological Tables, prepared by R. J. List, Smithsonian Institution, Washington, D. C., 1951.

Stogryn, A., The brightness temperature of a vertically structured medium, Radio Science, 5, pp. 1397-1406, 1970.

Tai, C. T., Dyadic Green's Functions in Electromagnetic Theory, Intext Educational, Scranton, PA, 1971.

Tsang, L., and J. A. Kong, The brightness temperature of a half-space random medium with nonuniform temperature profile, Radio Science, 10, pp. 1025-1033, 1975.

Tsang, L., and J. A. Kong, Emissivity of a half-space random medium, Radio Science, 11, pp. 593-598, 1976.

Tsang, L., E. Njoku, and J. A. Kong, Microwave thermal emission from a stratified medium with nonuniform temperature distribution, J. Appl. Phys., 46, pp. 5127-5133, 1975.

Ulaby, F. T., L. F. Dellwig, and T. Schmugge, Satellite microwave observations of the Utah Great Salt Lake Desert, Radio Science, 10, pp. 947-973, 1975.

Wait, J. R., Electromagnetic Waves in Stratified Media, Pergamon, New York, 1962.

Wang, J. R., and T. J. Schmugge, An empirical model for the complex dielectric permittivity of soils as a function of water content, NASA Tech. Memo. 79659, Goddard Space Flight Center, Greenbelt, MD, 1978.

Wilheit, T. T., Radiative Transfer in a plane stratified dielectric, IEEE Trans. Geosci. Electron., GE-16, pp. 138-143, 1978.

Yaglom, A. M., Comments on wind and temperature flux-profile relationships, Boundary-Layer Meteorol., 11, pp. 89-102, 1977.

FIGURES

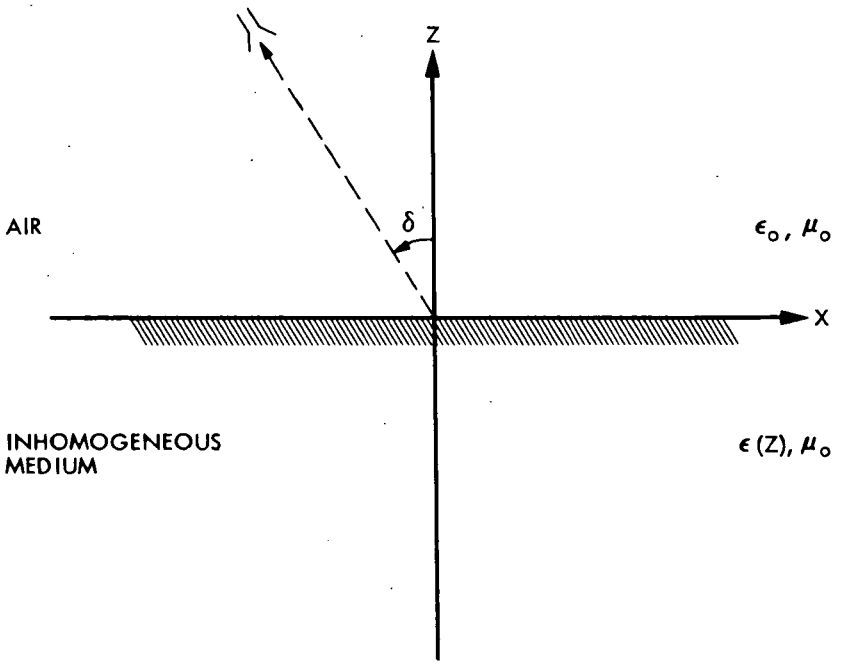

Figure 1. Geometrical Configuration for Emission from Inhomogeneous Half-Space

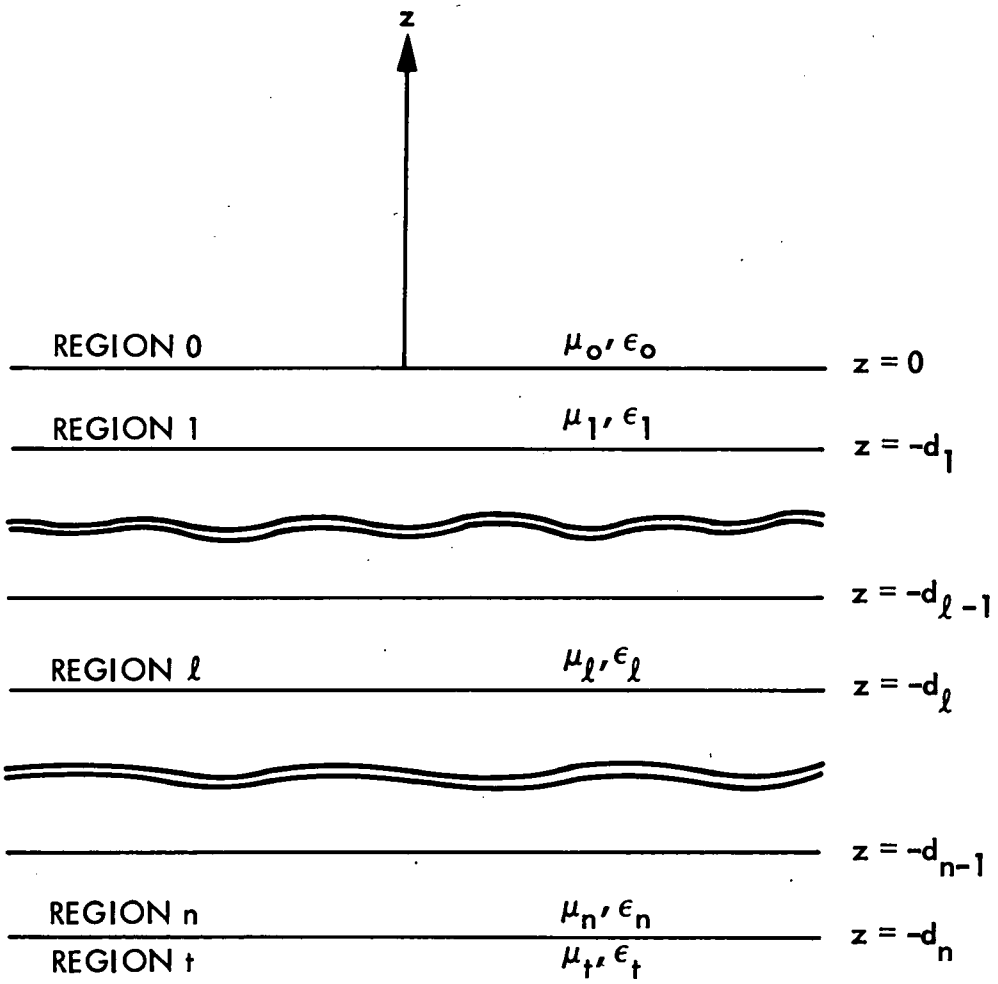

Figure 2. Geometrical Configuration for Emission from Stratified Half-Space

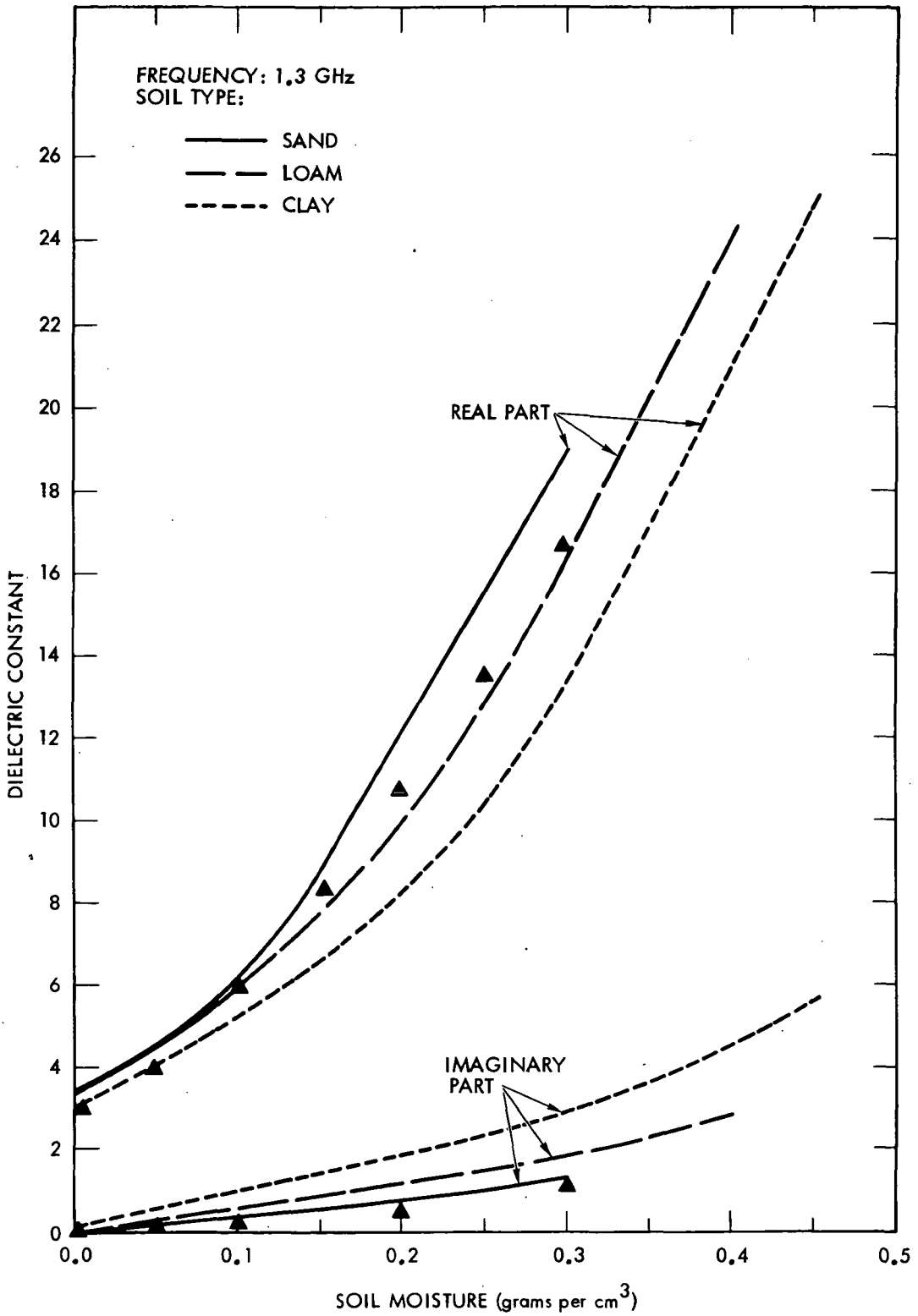

Figure 3. Typical Curves for the Dependence of Soil Dielectric Constant on Volumetric Moisture Content at 1.3 GHz (Cihlar and Ulaby, 1974). Superimposed Data Points are from Measurements of Sand (Njoku and Kong, 1977)

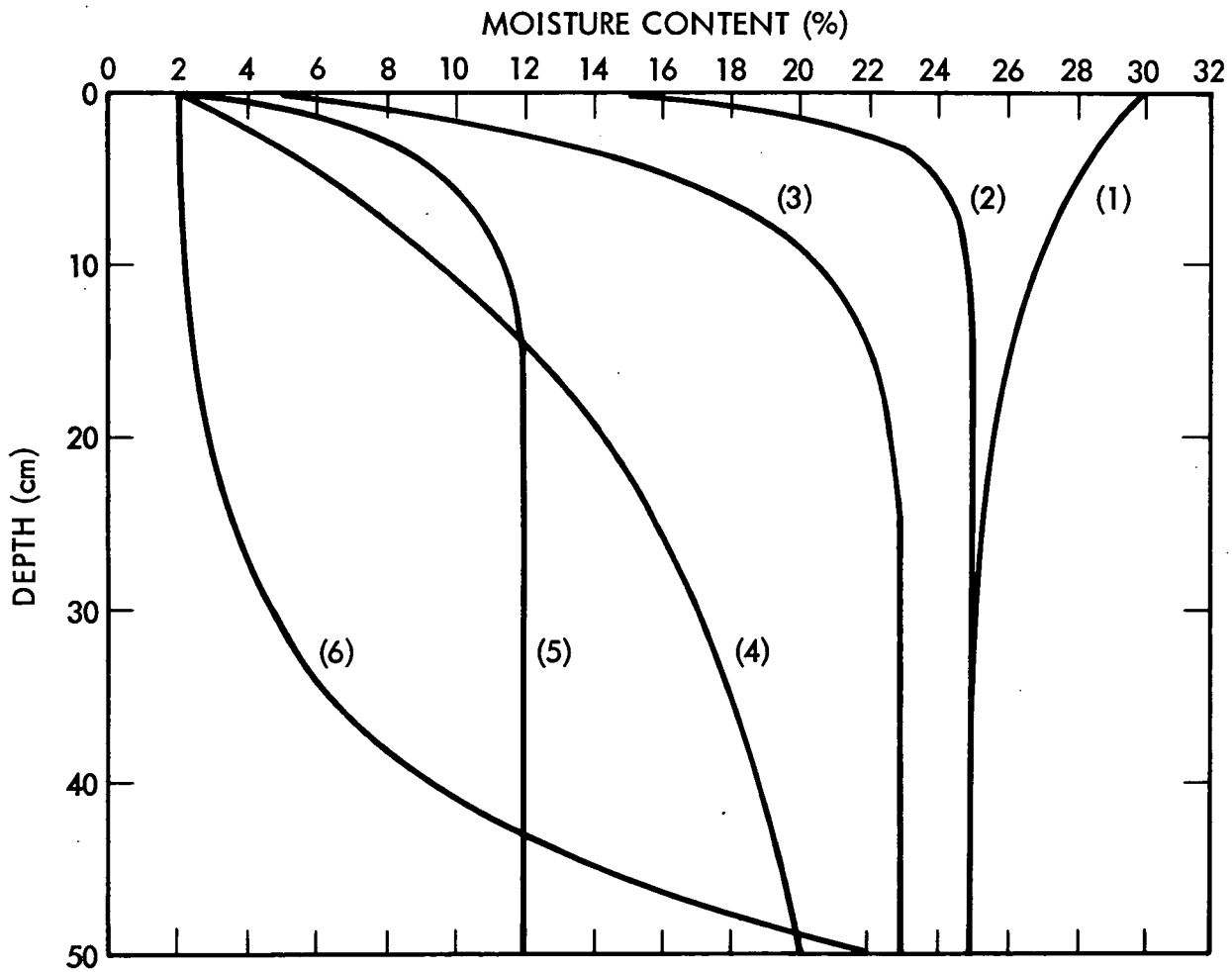

Figure 4. Analytical Soil Moisture Profiles Used in Theoretical Microwave Emission Model Calculations

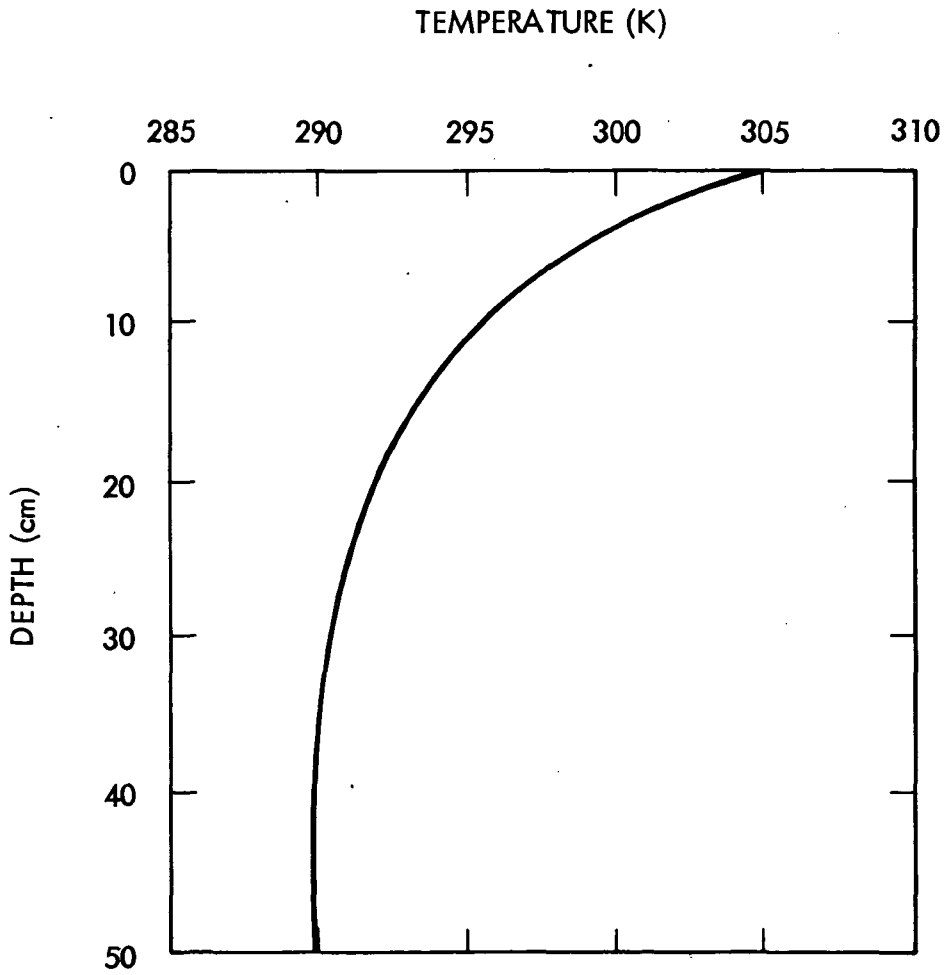

Figure 5. Temperature Profile Used in Theoretical Microwave Emission Model Calculations

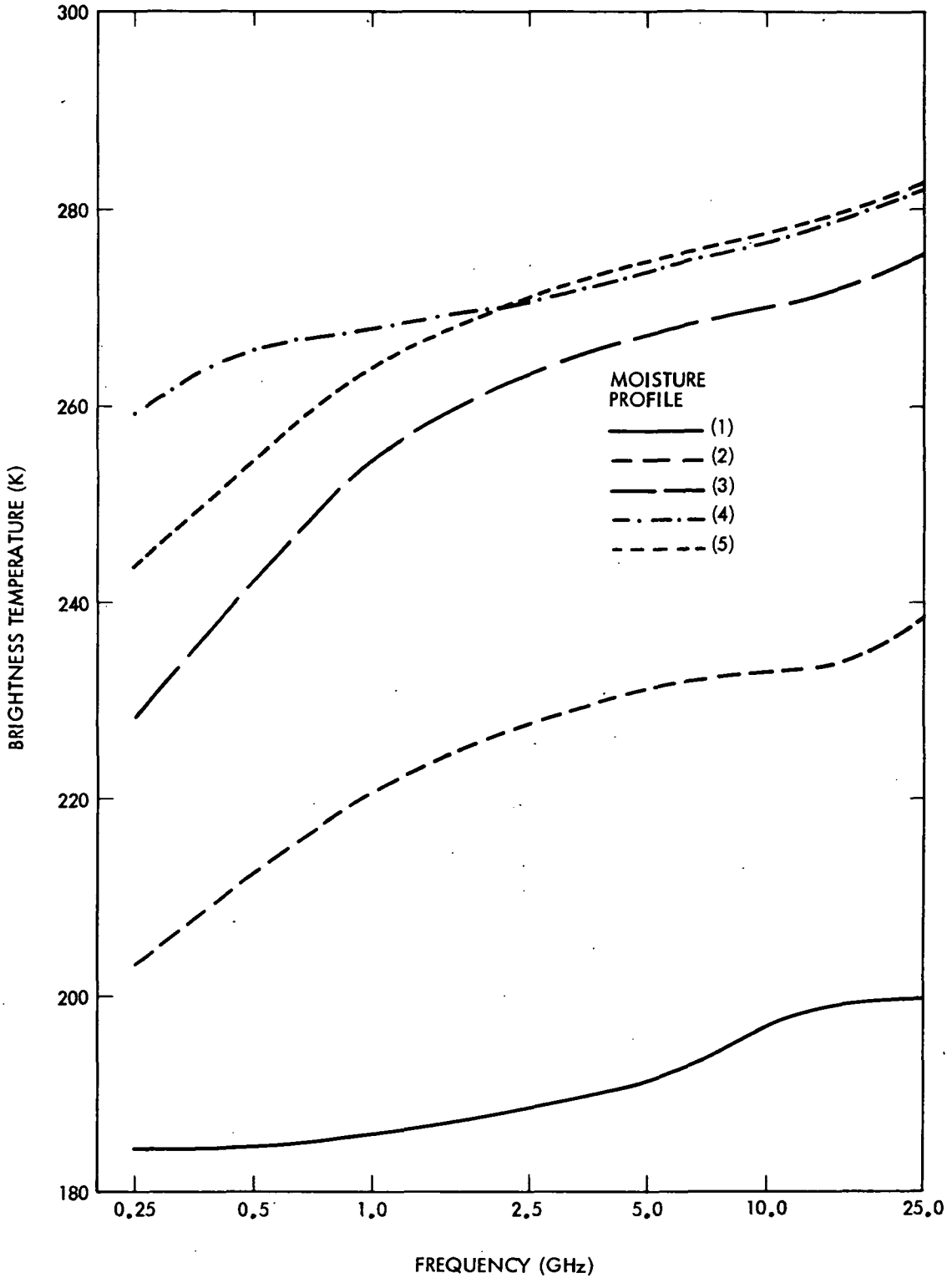

Figure 6. Results of Theoretical Calculations Using Coherent Model Showing Brightness Temperature as a Function of Frequency. Calculations were Performed for Nadir View ($\delta = 0^{o}$), and Dielectric Constants of Sand were Used (Njoku and Kong, 1977)

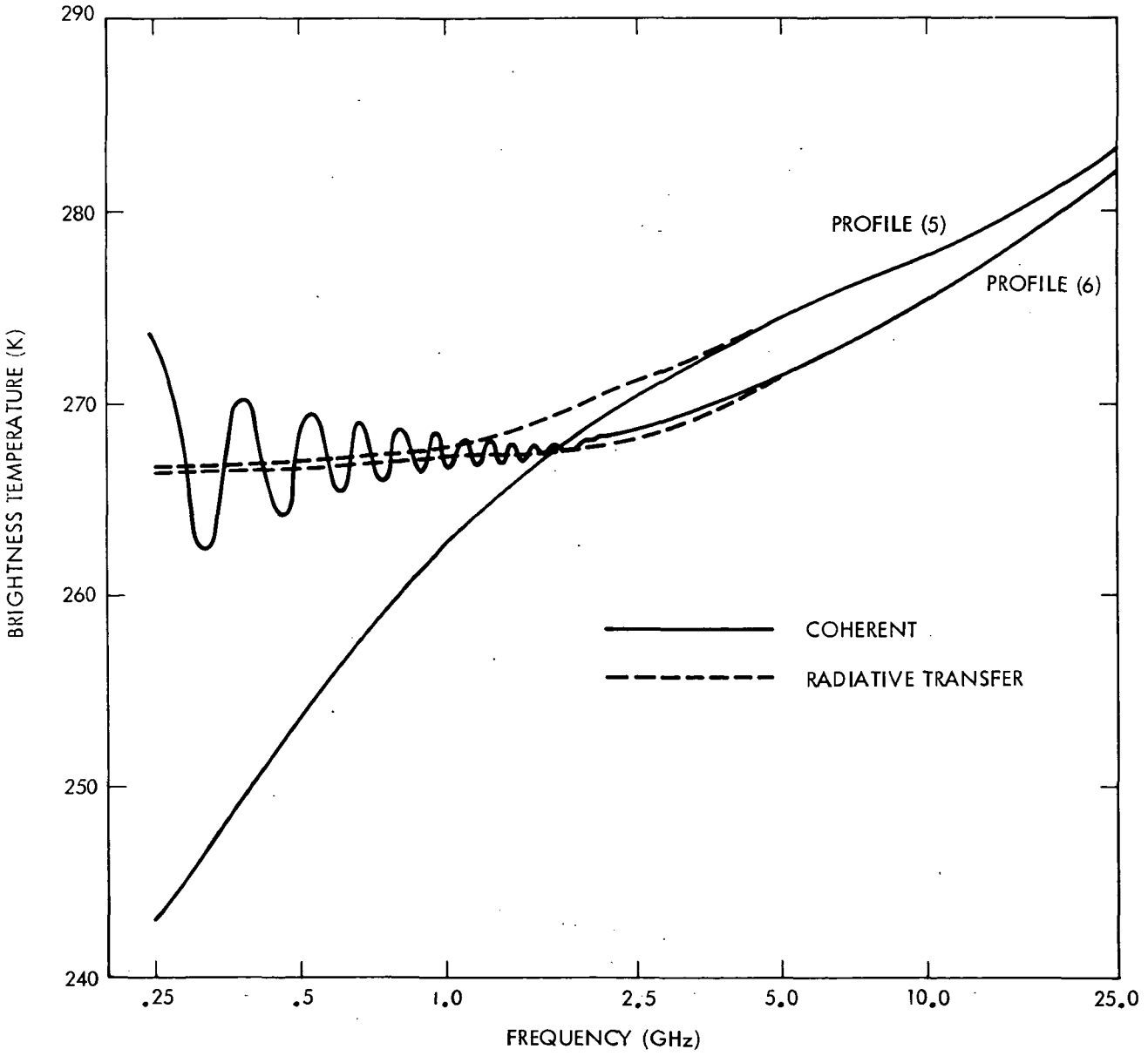

Figure 7. Results of Theoretical Calculations Comparing Radiative Transfer and Coherent Models ($\delta = 0^{o}$, Sand Dielectric Constants)

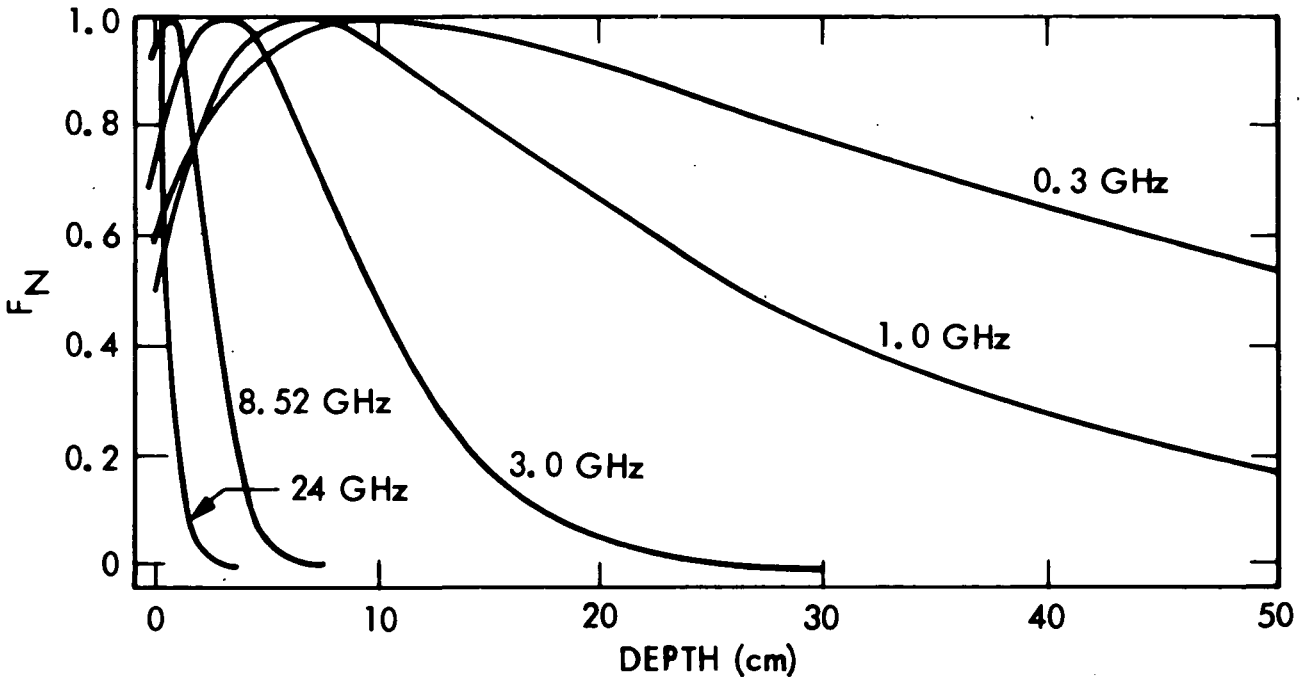

Figure 8. Normalized Temperature Weighting Functions for Moisture Profile 3 ($\delta = 0^o$)

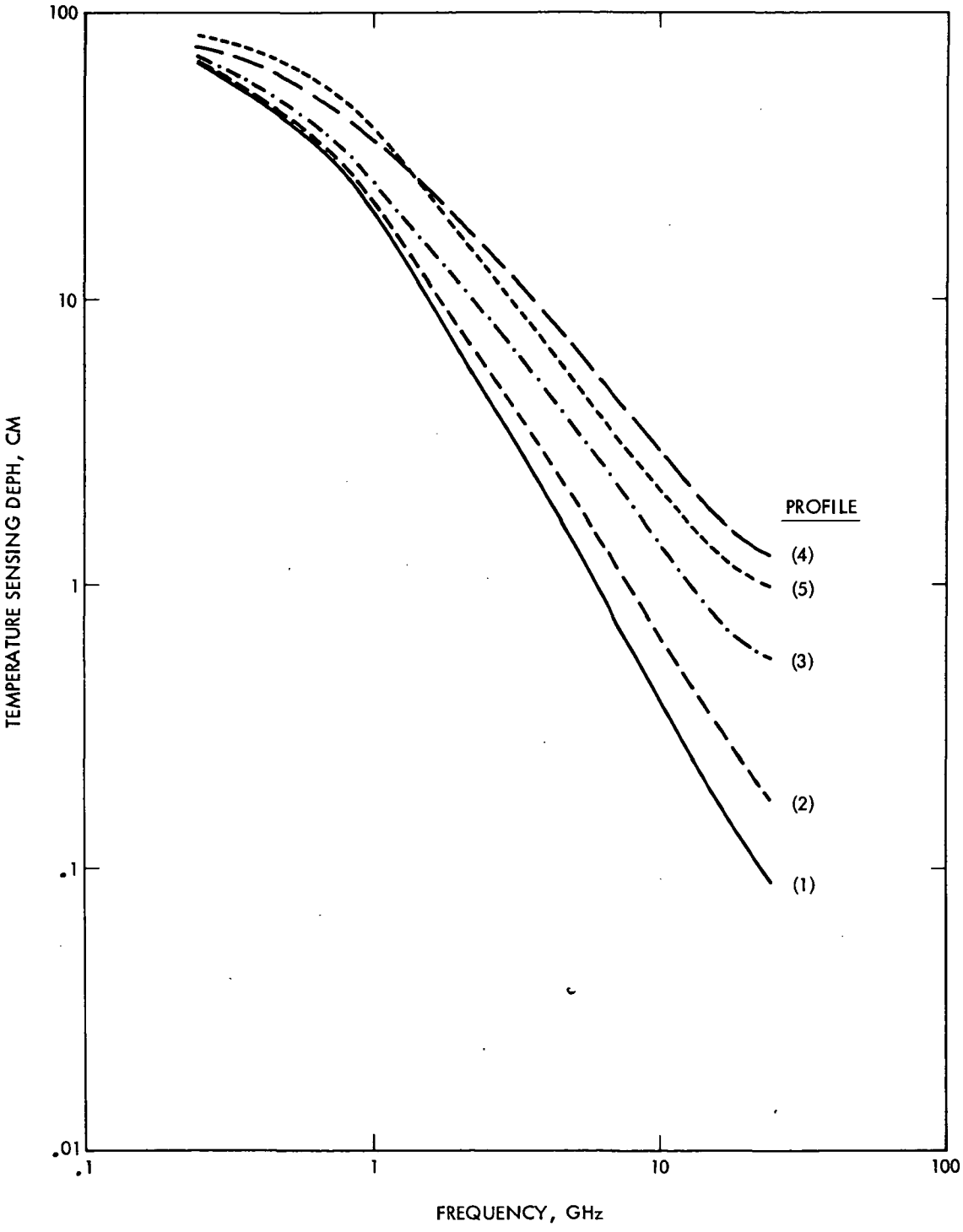

Figure 9. Temperature Sensing Depth for Sand as Function of Frequency for Moisture Profiles 1 to 5

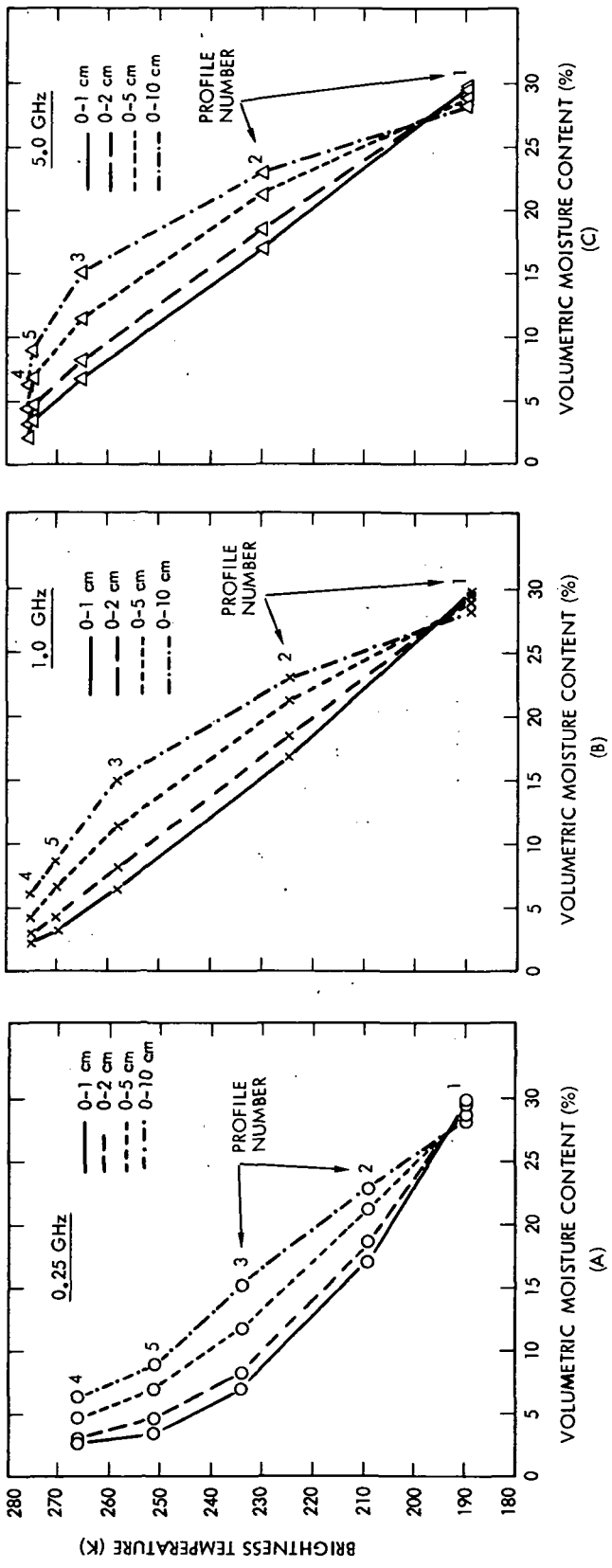

Figure 10. Theoretical Relationships Between Brightness Temperature and Average Volumetric Moisture Content in Top Layers of Soil, Using Moisture Profiles 1 to 5 and Sand Dielectric Constants at (a) 0.25 GHz, (b) 1.0 GHz, and (c) 5.0 GHz

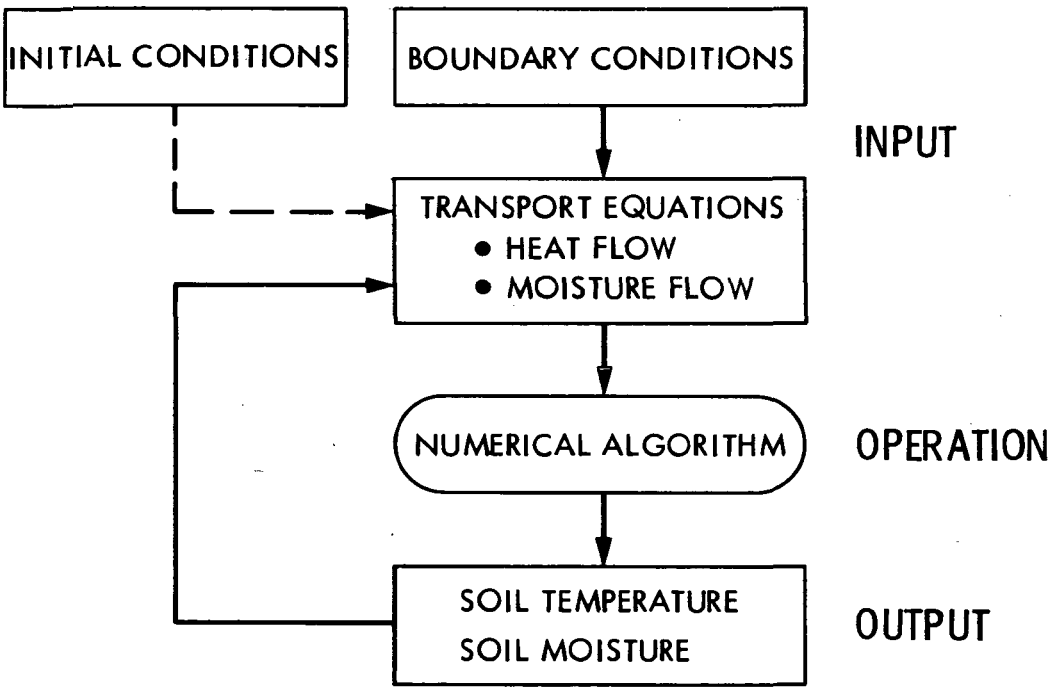

Figure 11. Block Diagram of Numerical Model

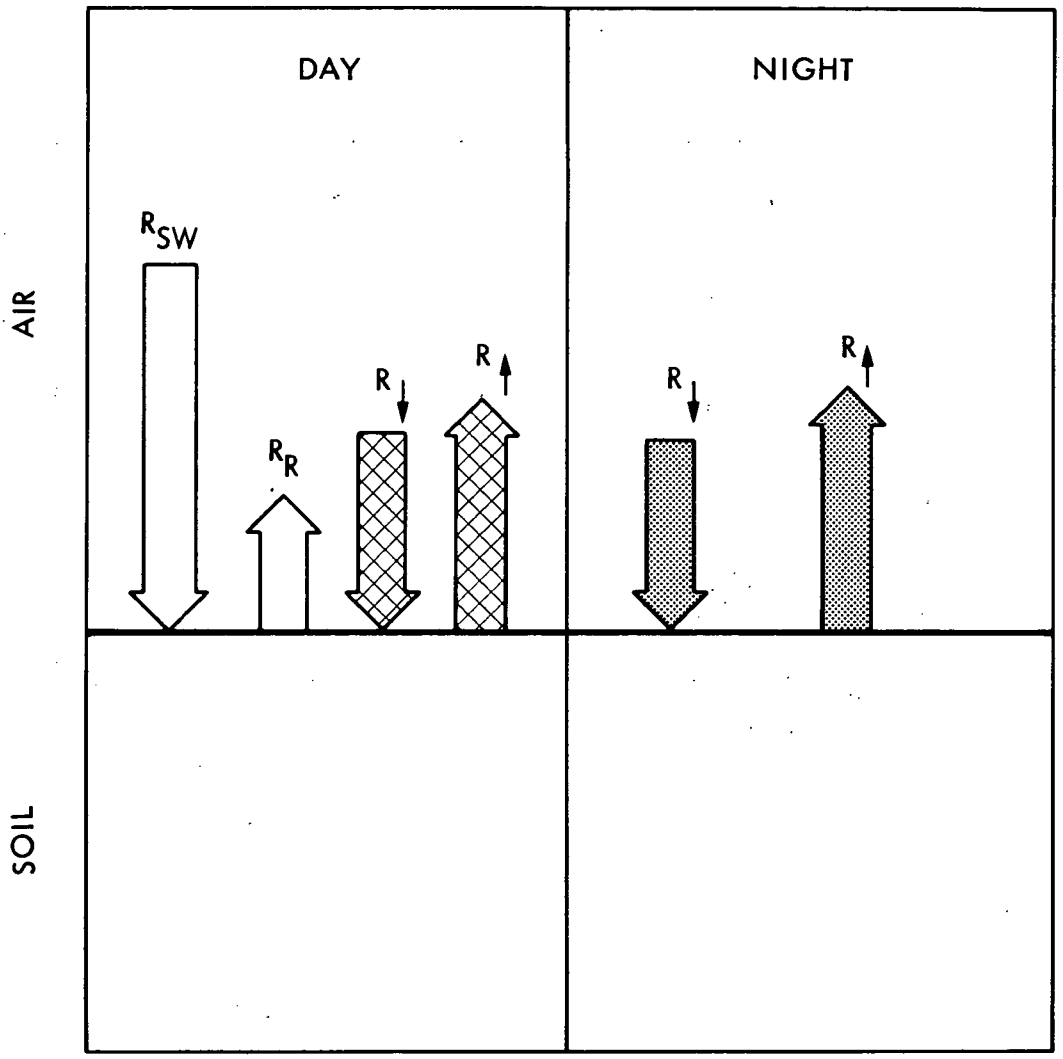

Figure 12. The Daytime and Nighttime Radiation Balance at the Surface. R_{SW} is the Incoming Shortwave Component; R_R is the Reflected Shortwave Radiation; $R_\downarrow$ and $R_\uparrow$ are the Downward and Upward Longwave Components

$$R_N = Q_S + Q_E + Q_G$$

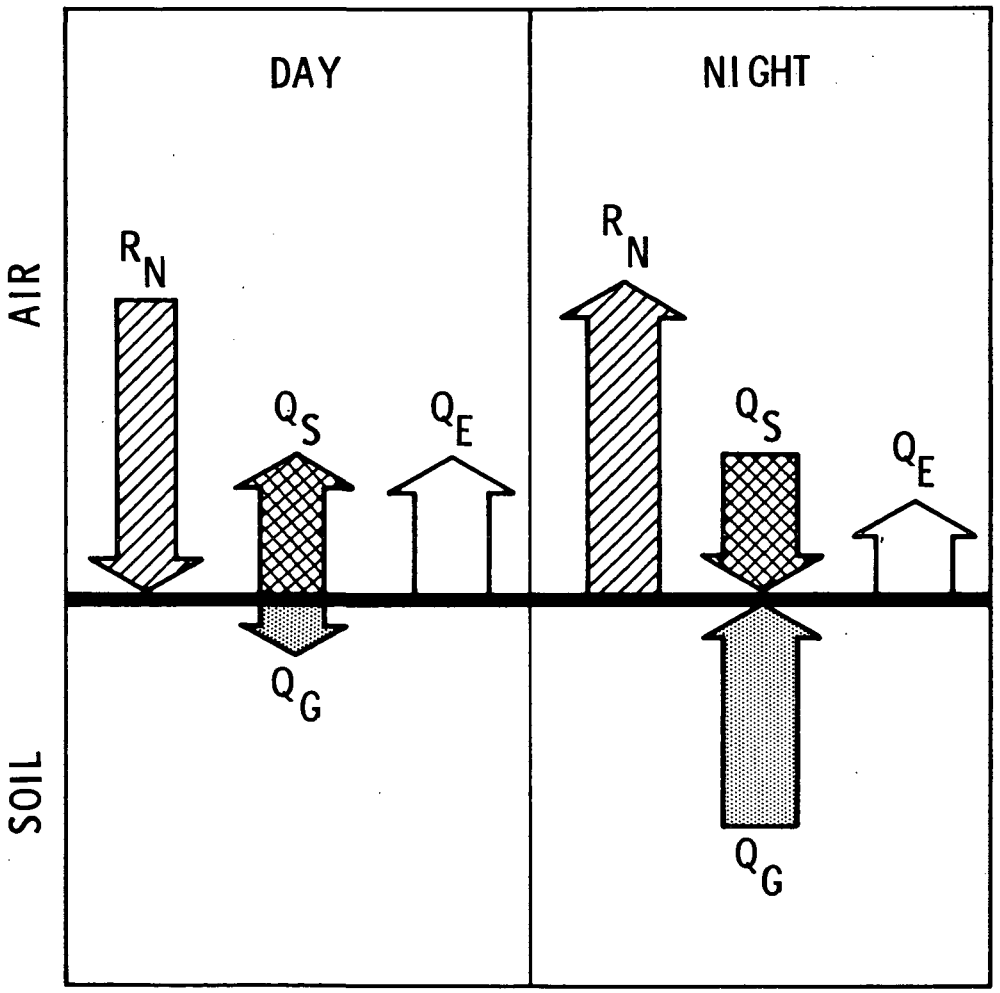

Figure 13. Components of the Surface Energy. R_N is the Net Radiation; Q_S is the Sensible Heat Flux; Q_E is the Latent Heat Flux; Q_G is the Soil Heat Flux

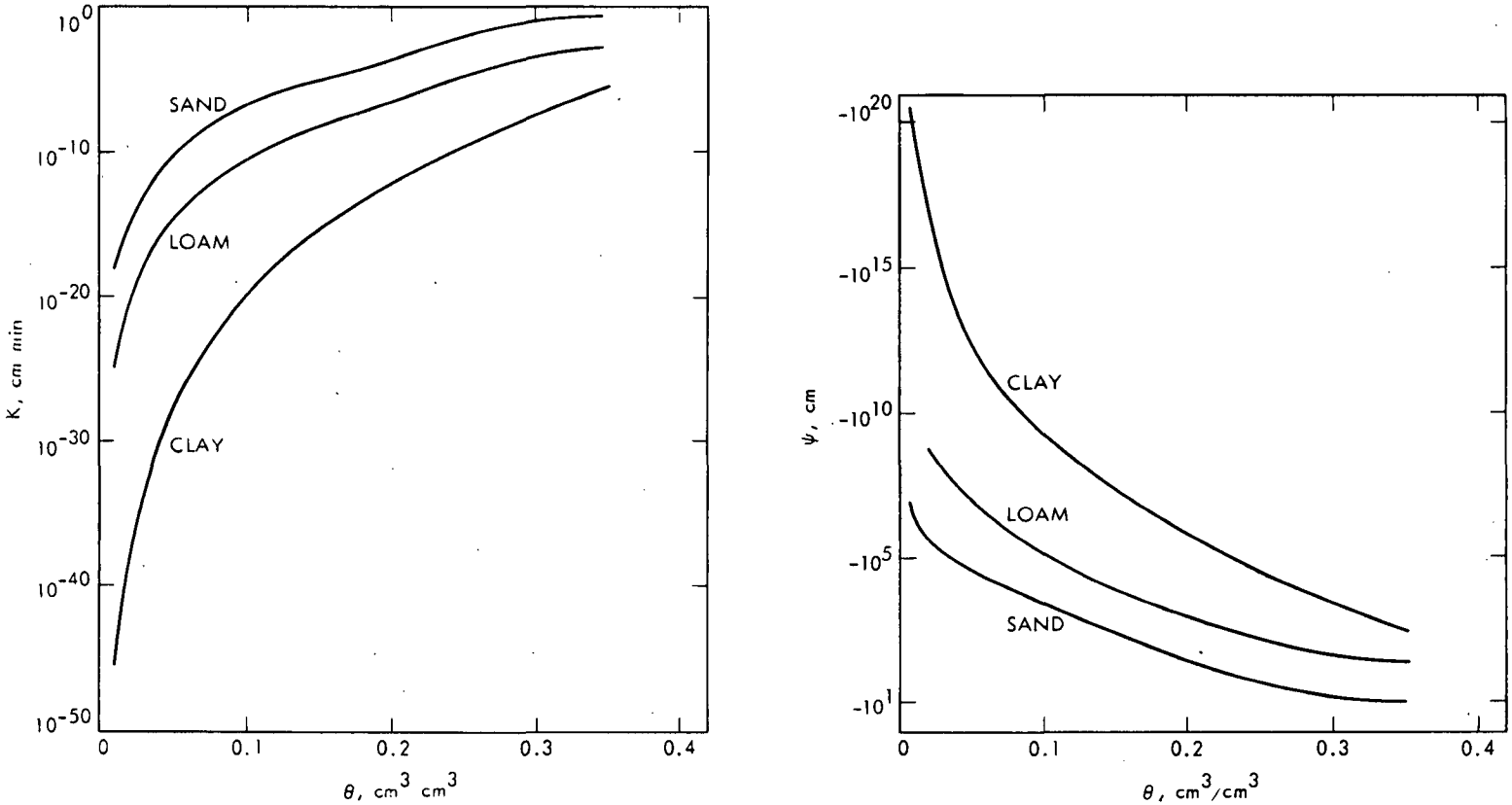

Figure 14. Hydraulic Conductivity Versus Soil Moisture Content and Capillary Potential Versus Soil Moisture Content

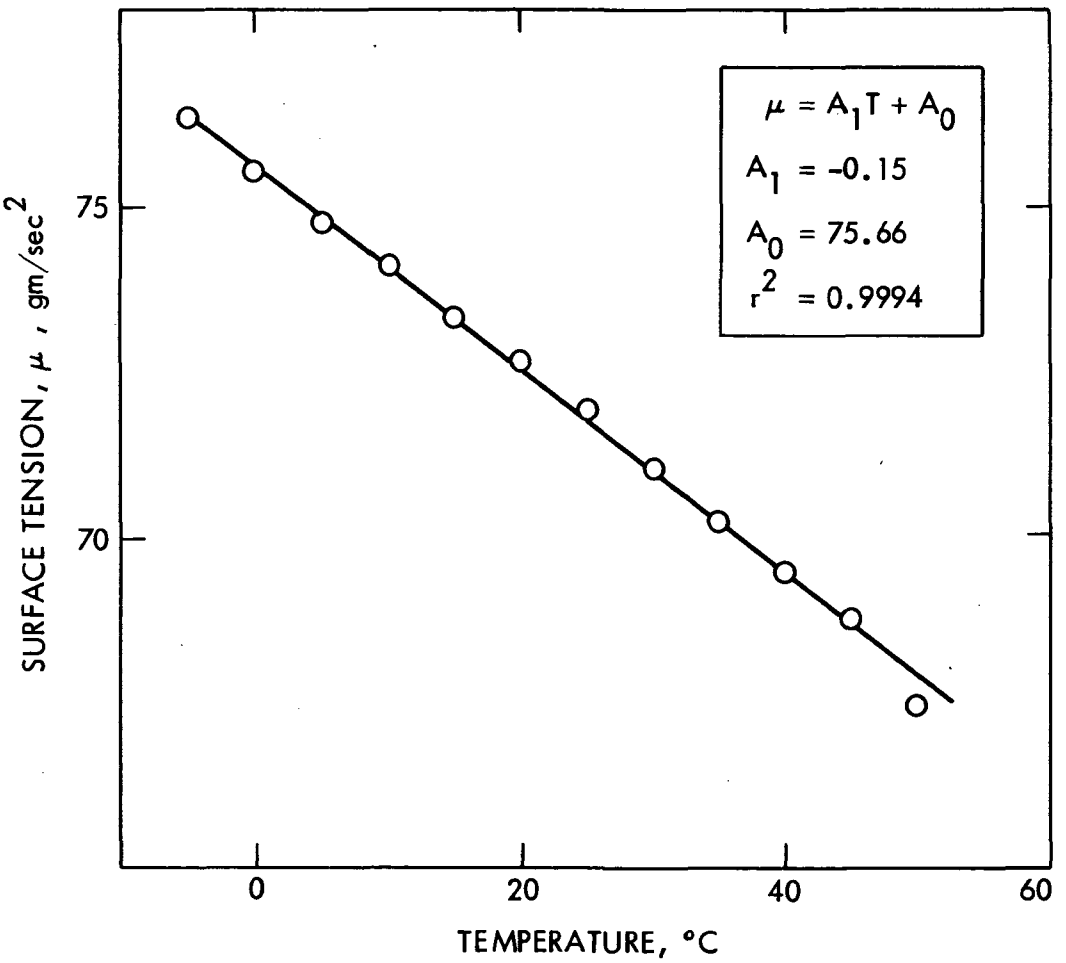

Figure 15. Surface Tension Versus Temperature. The Relationship is Quite Linear ($r^2 = 1.000$ is a perfect fit)

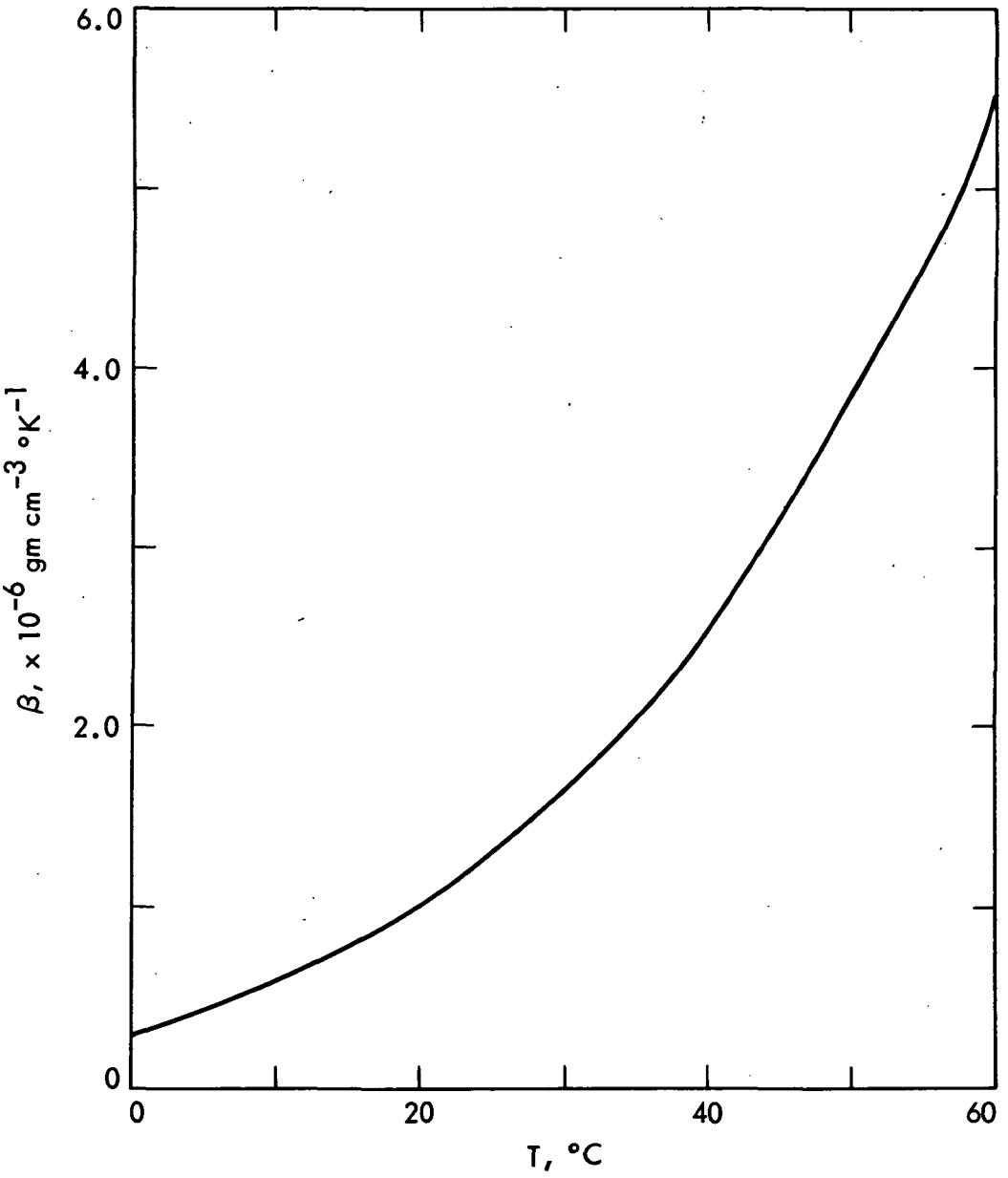

Figure 16. Coefficient of Thermal Expansion as a Function of Temperature

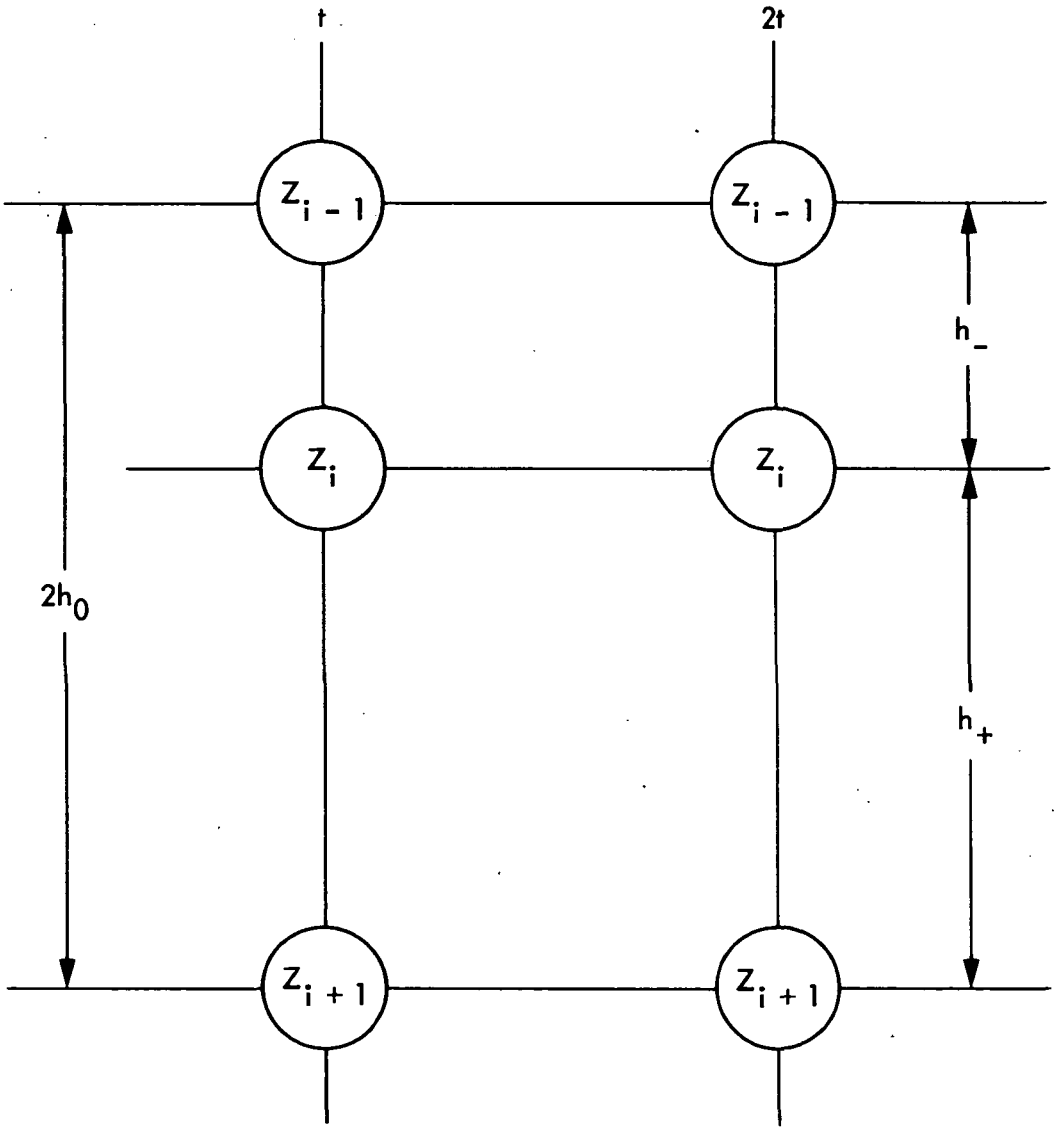

Figure 17. Computational Molecule for the Numerical Model. Time is Denoted by t, Space by z.

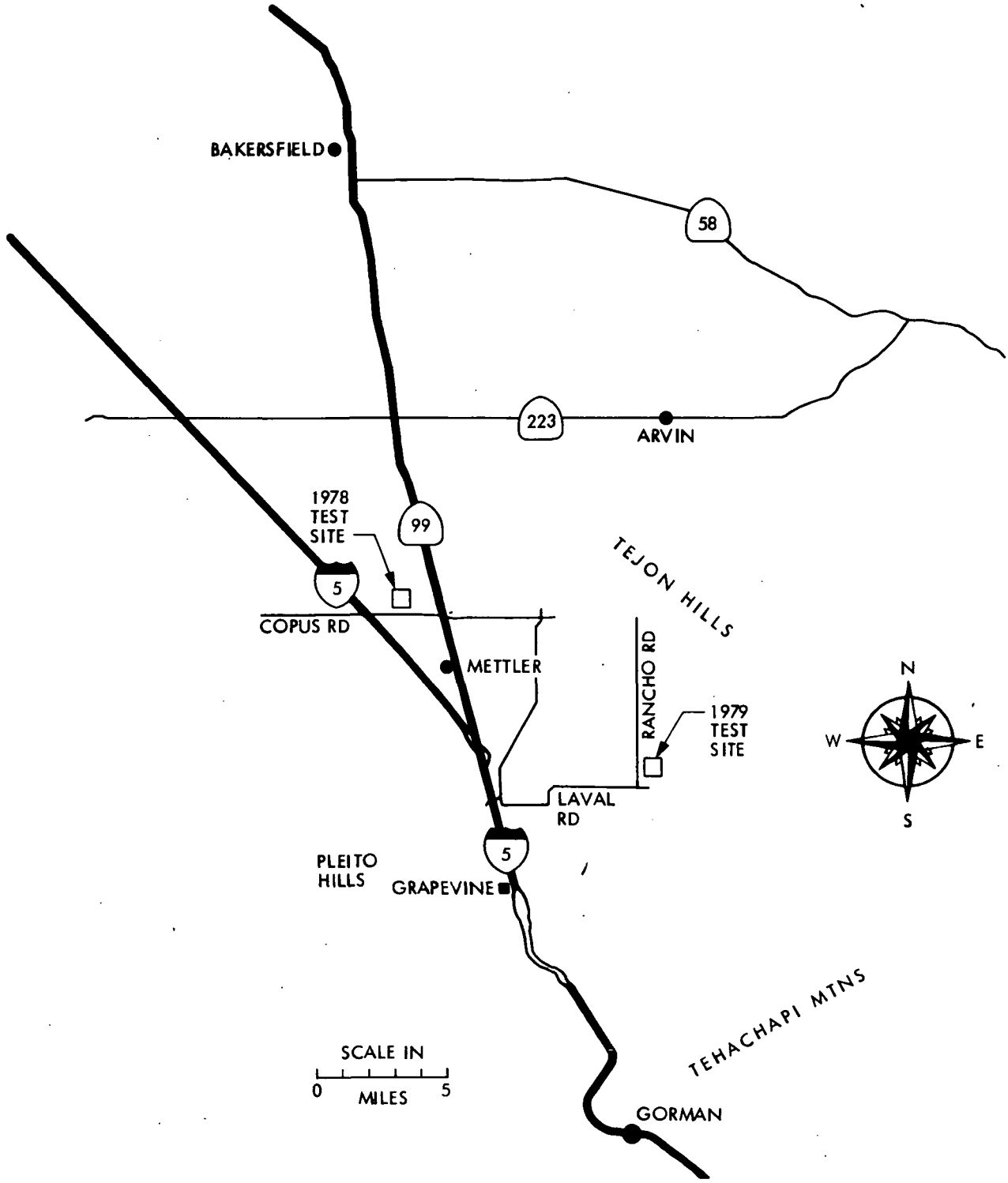

Figure 18. Location Map of 1978 and 1979 Test Sites

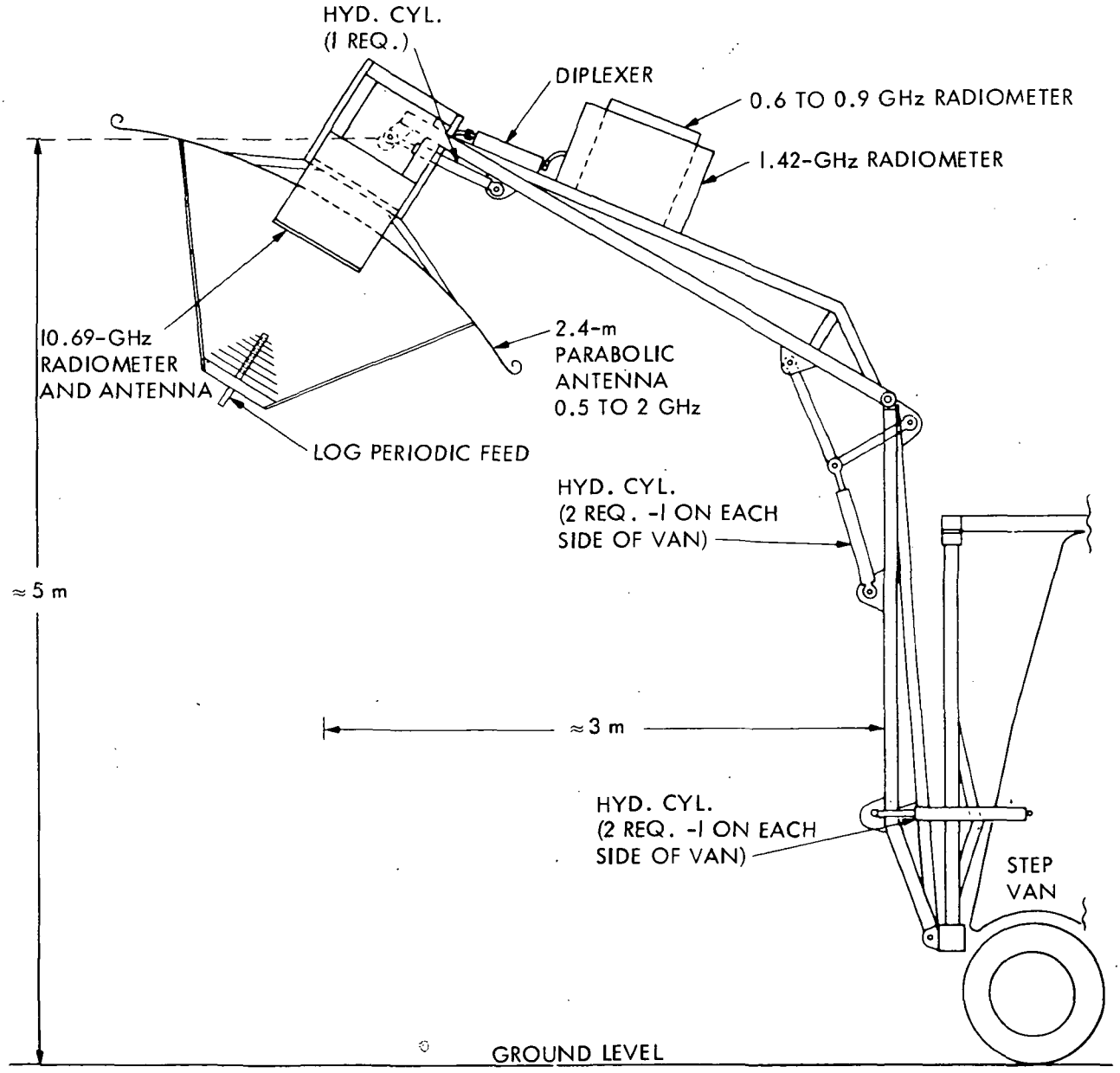

Figure 19. Sketch of JPL Microwave Radiometry Field Van Antenna and Radiometer Assembly

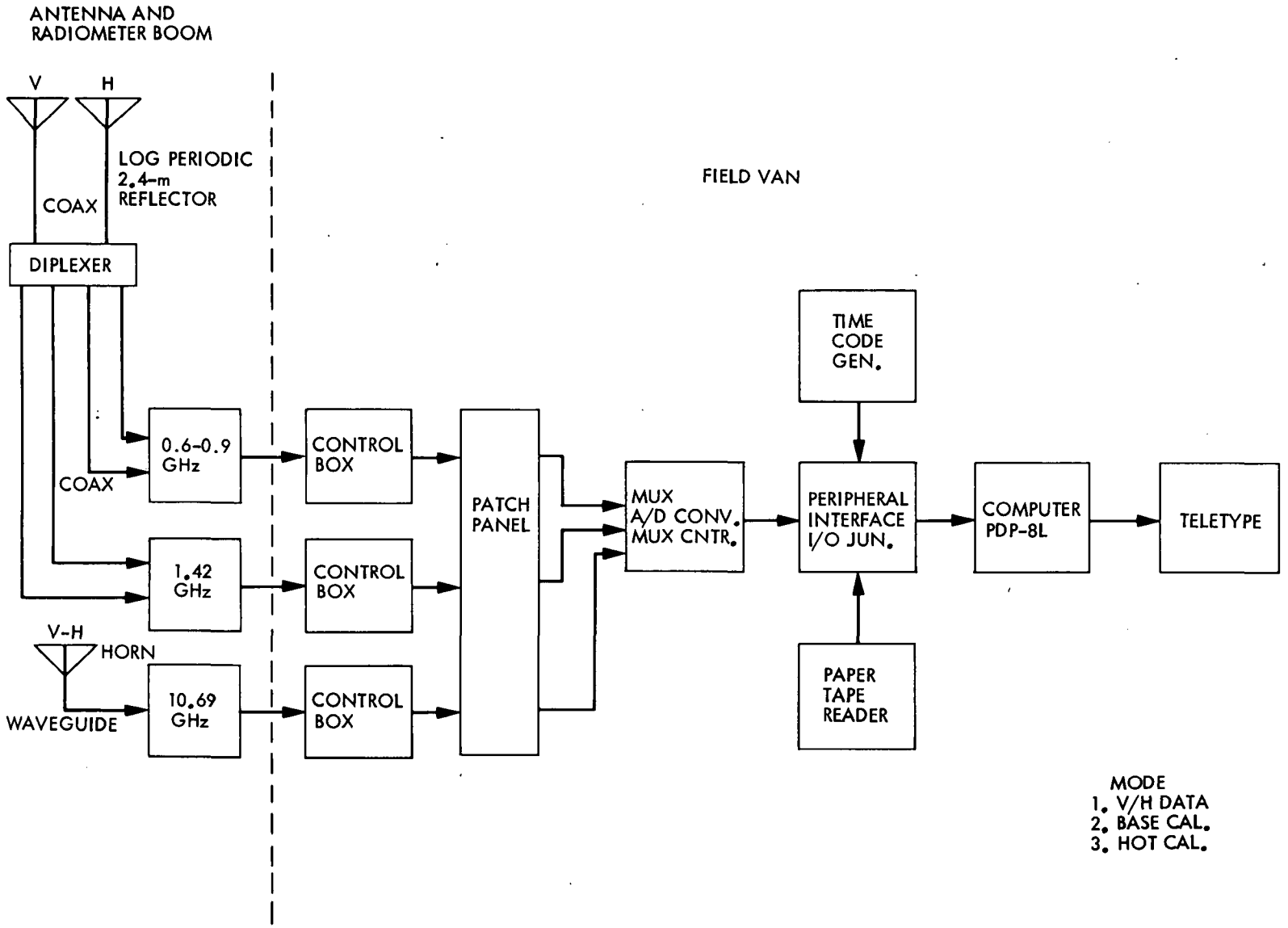

Figure 20. Functional Block Diagram of Radiometer Measurement System

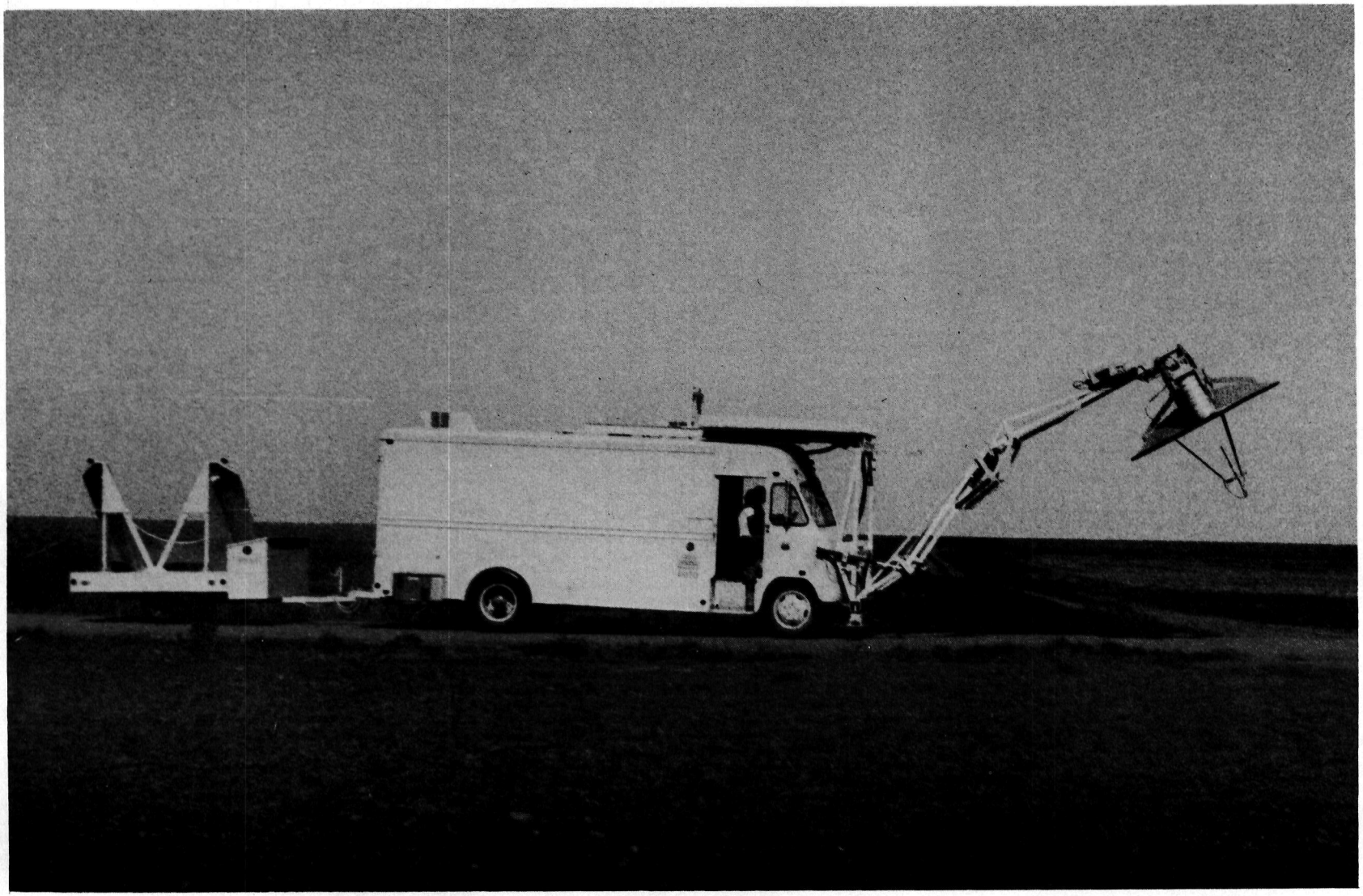

Figure 21. Photograph of Microwave Field Van in Transit with Antennas in Deployed Position

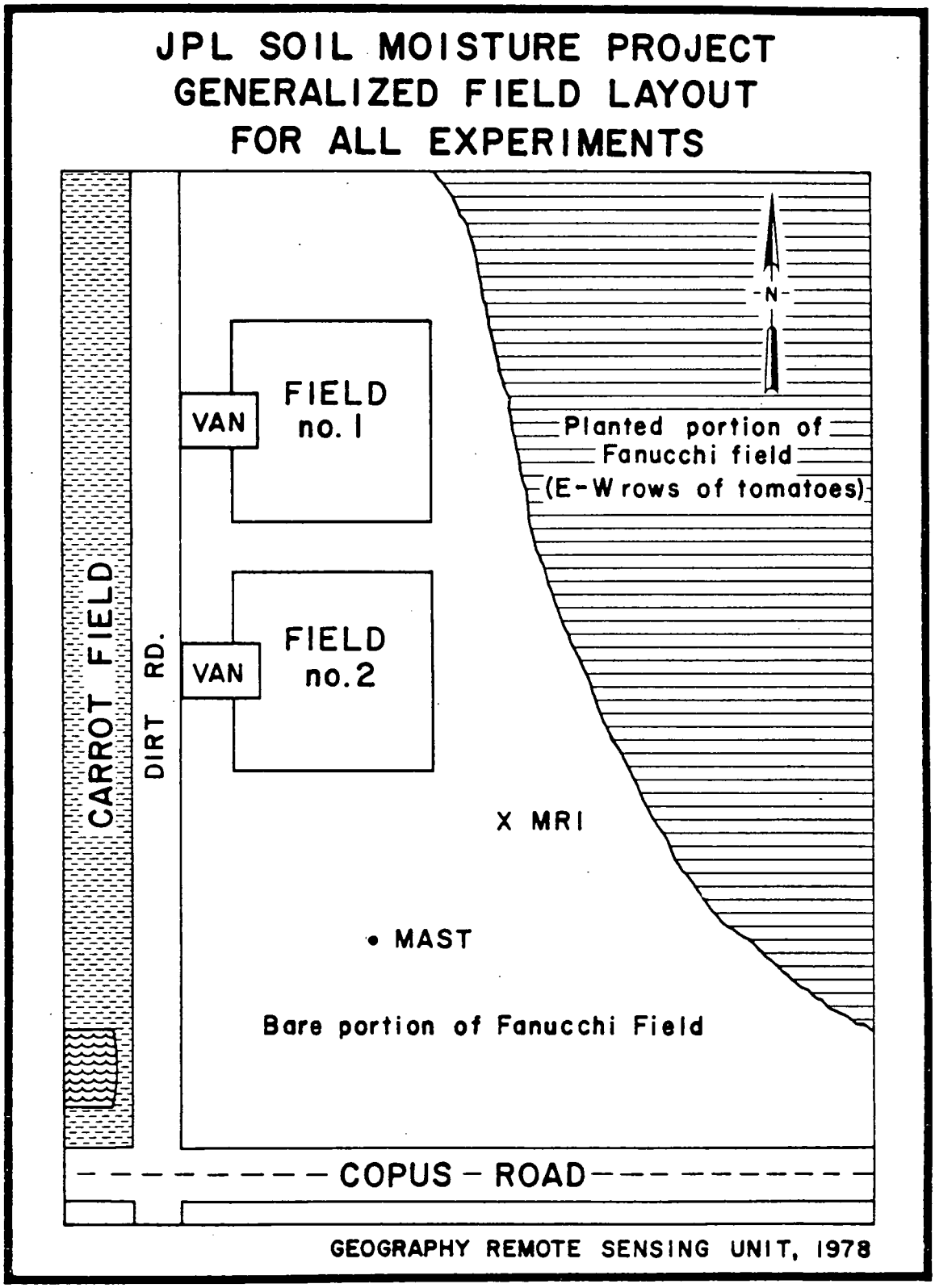

Figure 22. Generalized Field Layout of the 1978 Soil Moisture Experiment (from O'Neill and Atwater, 1978)

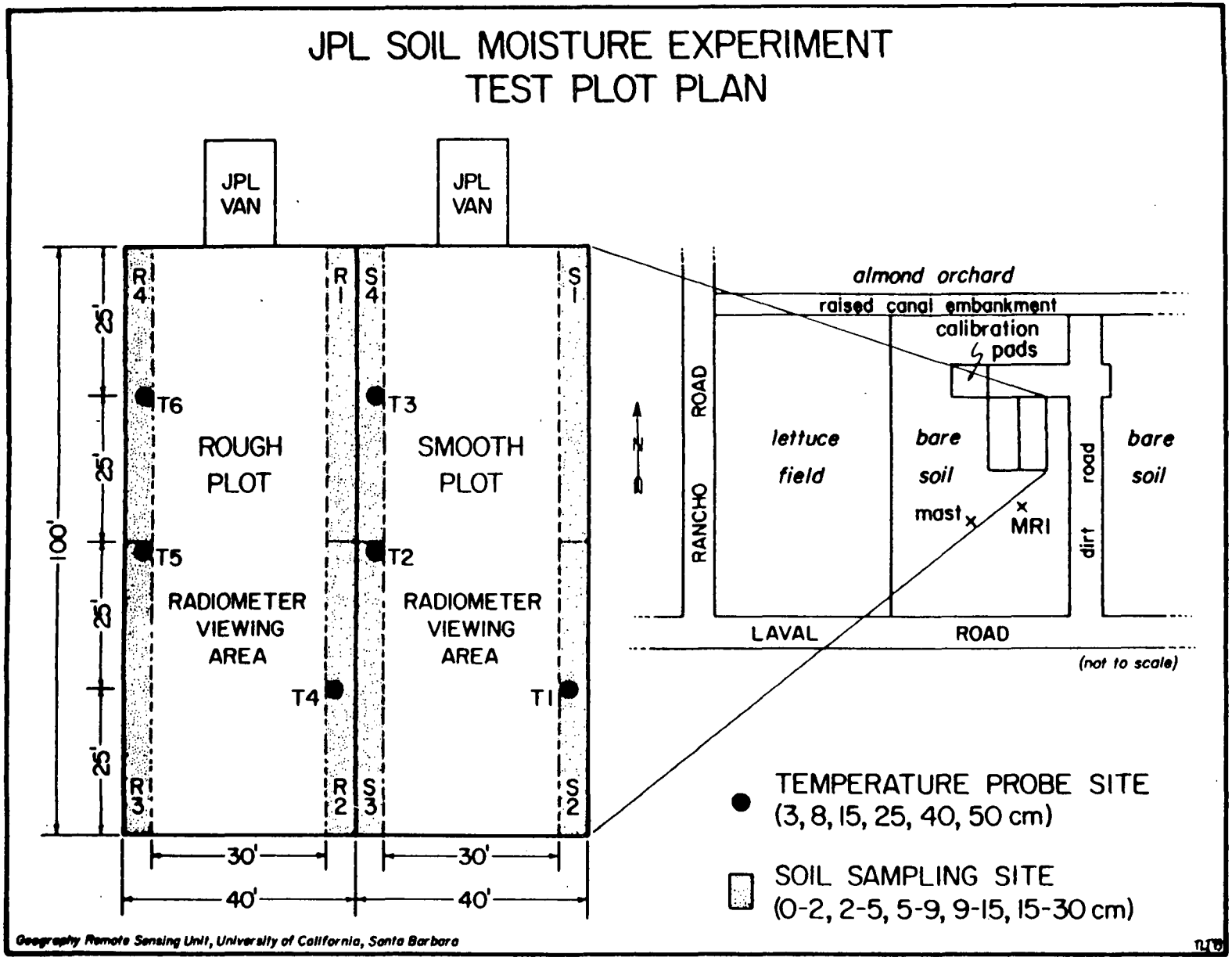

Figure 23. Generalized Field Layout of the 1979 Soil Moisture Experiment (from Atwater and O'Neill, 1979)

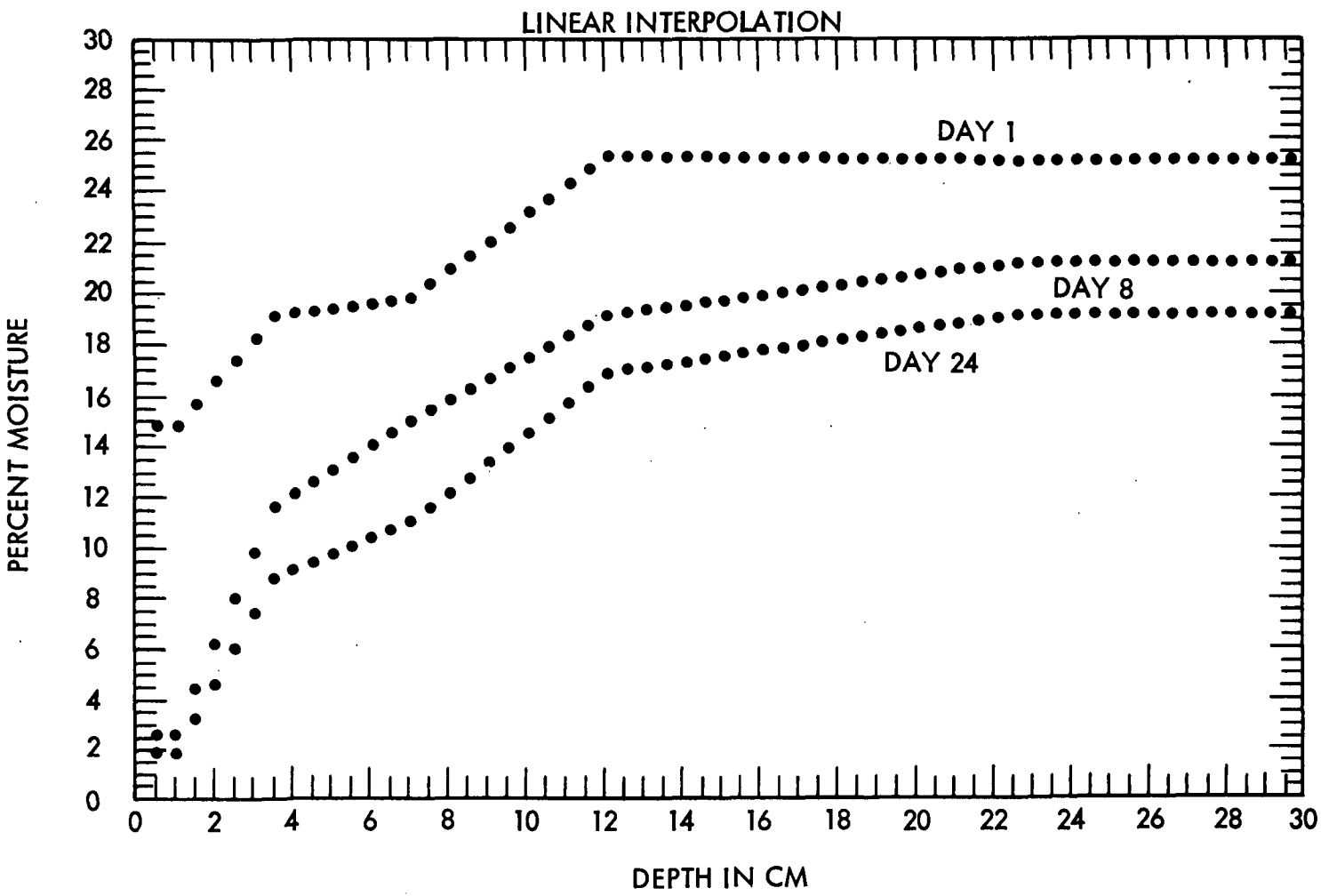

Figure 24. Moisture Profiles Reconstructed by Interpolation from Ground Truth Data Samples. Days Shown are for Days After Irrigation

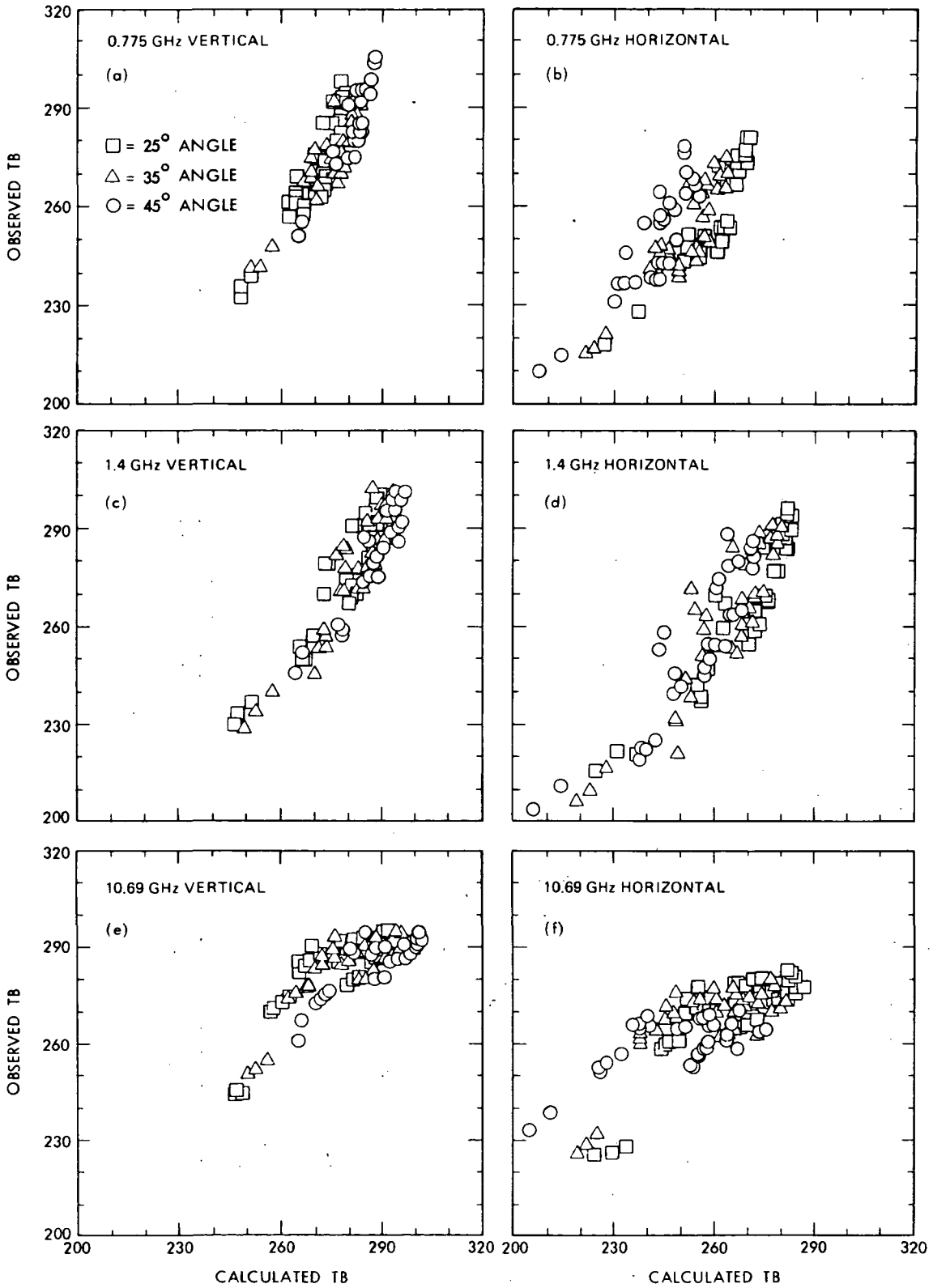

Figure 25. Observed Versus Calculated Brightness Temperatures at 0.775, 1.4, and 10.69 GHz Vertical and Horizontal Polarization (at Angles of 25°, 35°, and 45°)

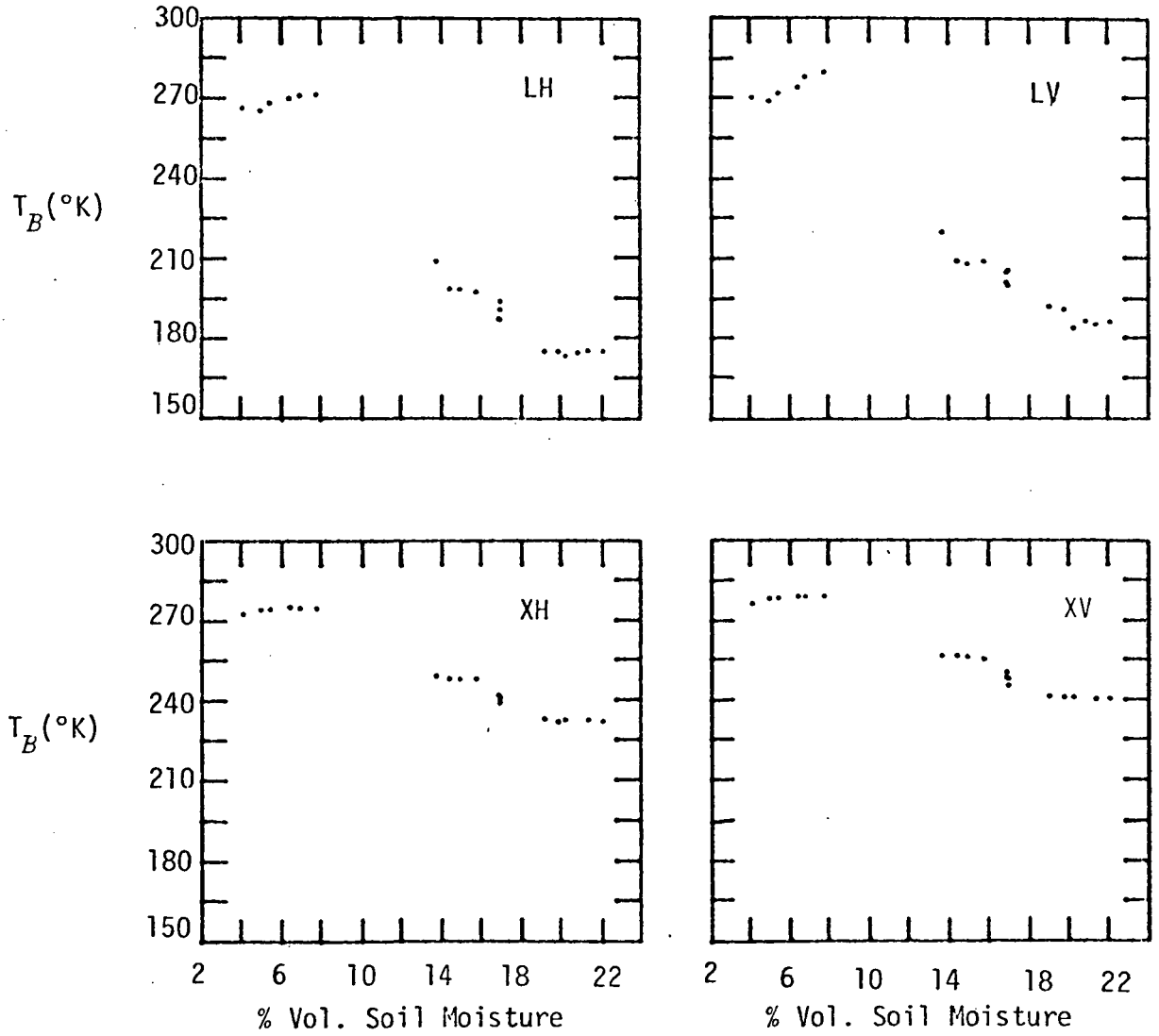

Figure 26(a). Microwave Brightness Temperature Versus Volumetric Soil Moisture in Top 0 - 2 cm for 1978 Smooth Field at a 25° Viewing Angle (L = 1.4 GHz, X = 10.69 GHz, V = Vertical Polarization, H = Horizontal Polarization)

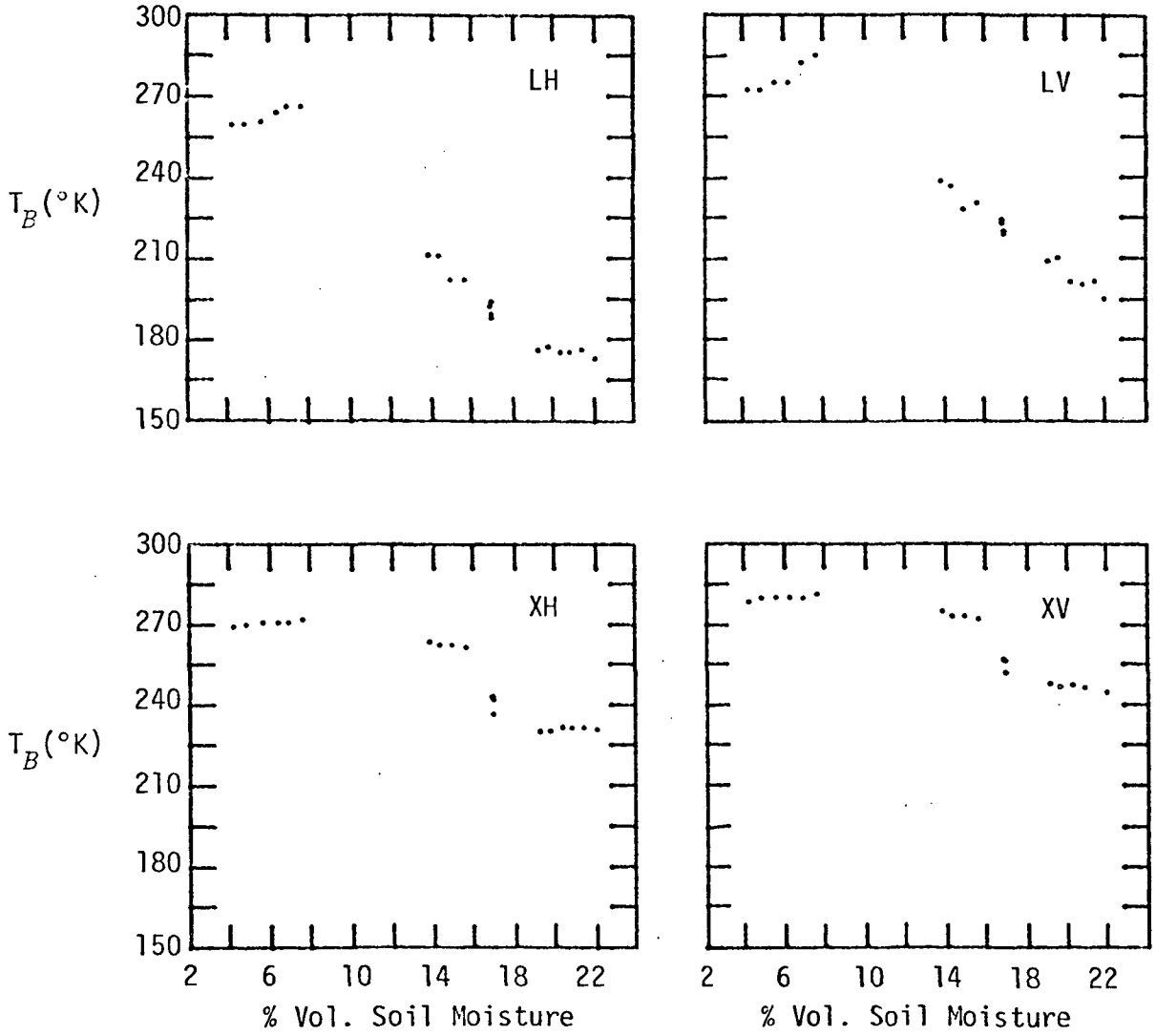

Figure 26(b). Microwave Brightness Temperature Versus Volumetric Soil Moisture in Top 0 - 2 cm for 1978 Smooth Field at a 35° Viewing Angle (L = 1.4 GHz, X = 10.69 GHz, V = Vertical Polarization, H = Horizontal Polarization)

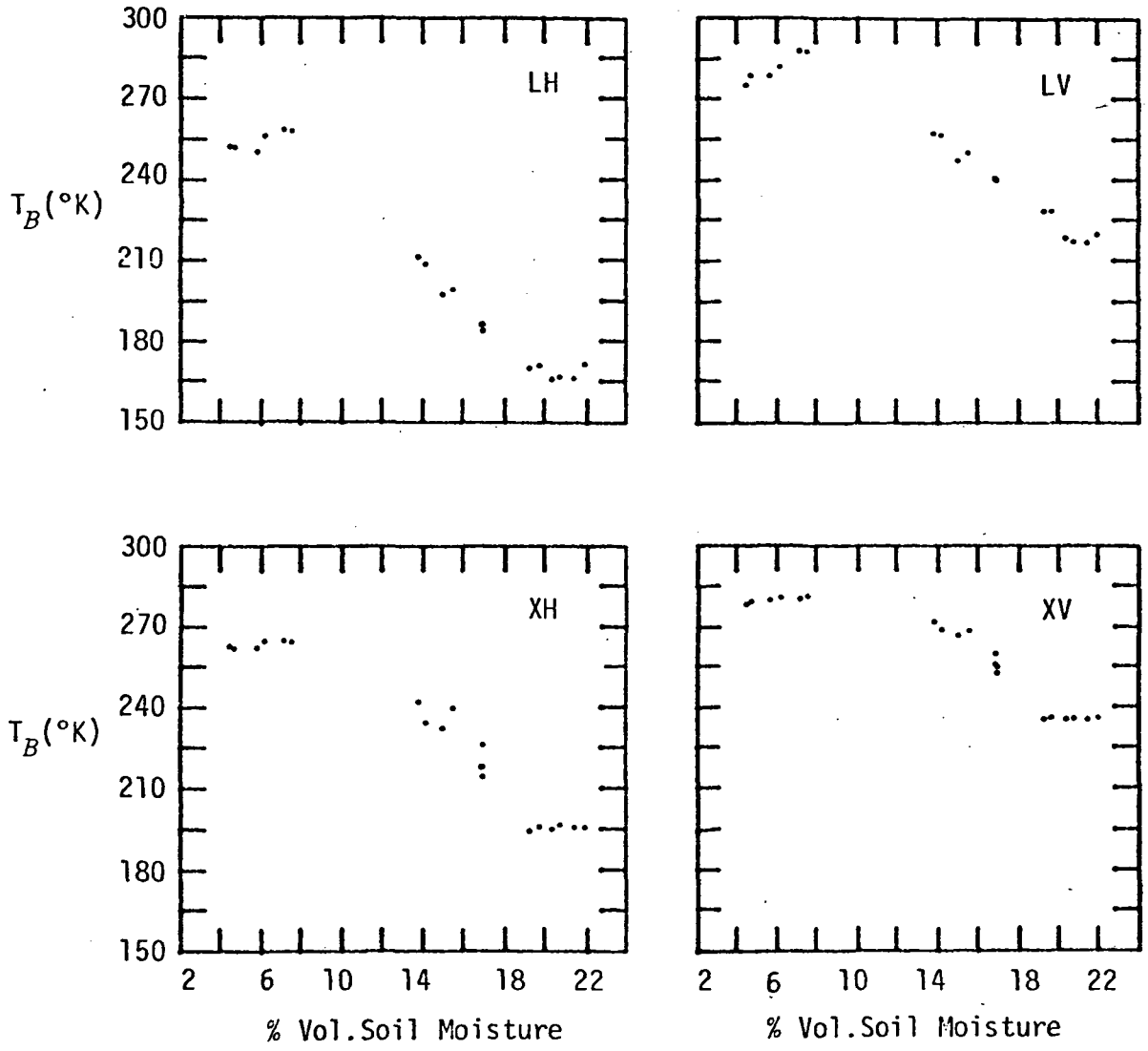

Figure 26(c). Microwave Brightness Temperature Versus Volumetric Soil Moisture in Top 0 - 2 cm for 1978 Smooth Field at a 45° Viewing Angle (L = 1.4 GHz, X = 10.69 GHz, V = Vertical Polarization, H = Horizontal Polarization)

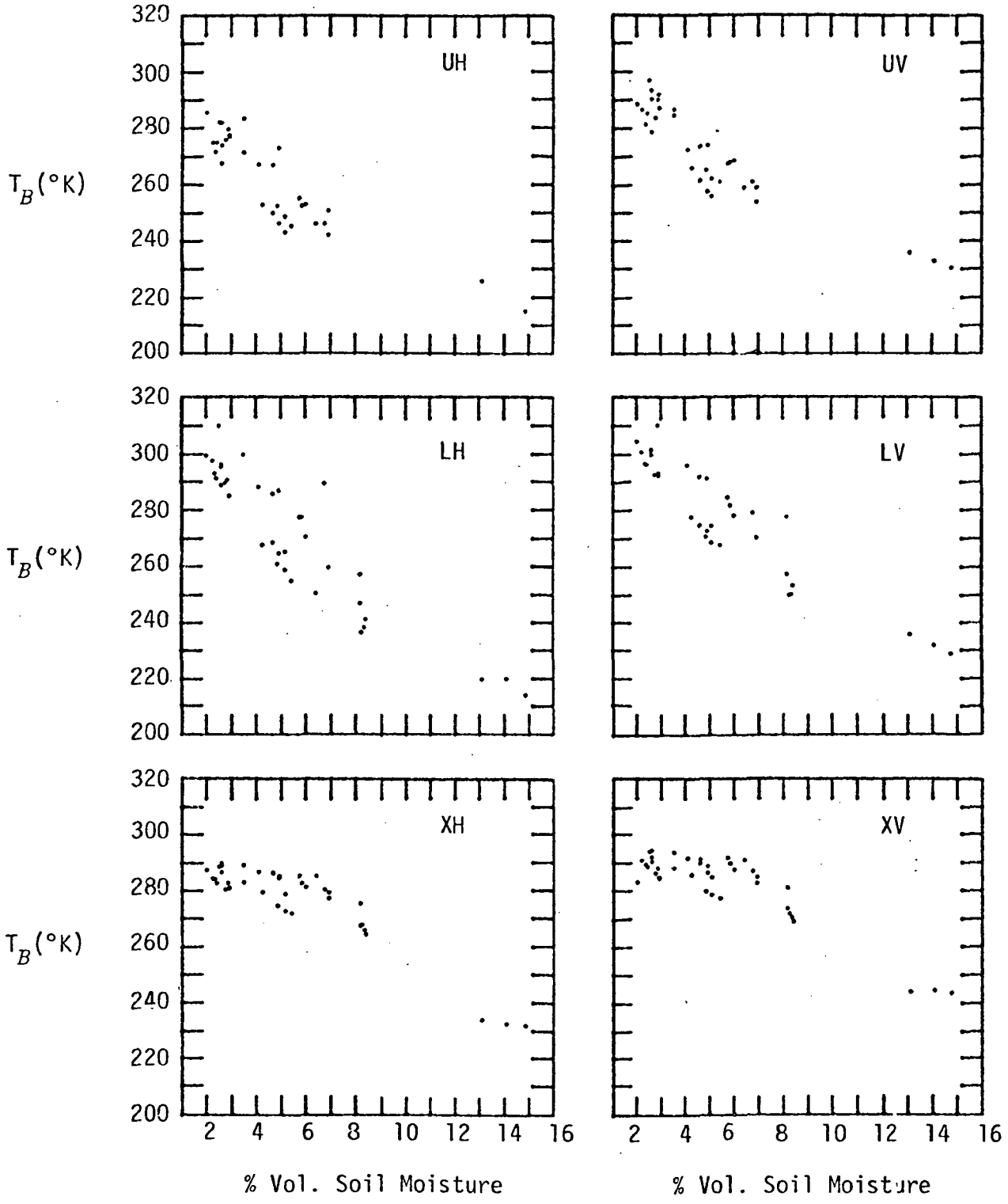

Figure 27(a). Microwave Brightness Temperature Versus Volumetric Soil Moisture in Top 0 - 2 cm for 1979 Smooth Field at a 25° Viewing Angle (U = 0.775 GHz, L = 1.4 GHz, X = 10.69 GHz, H = Horizontal Polarization, V = Vertical Polarization)

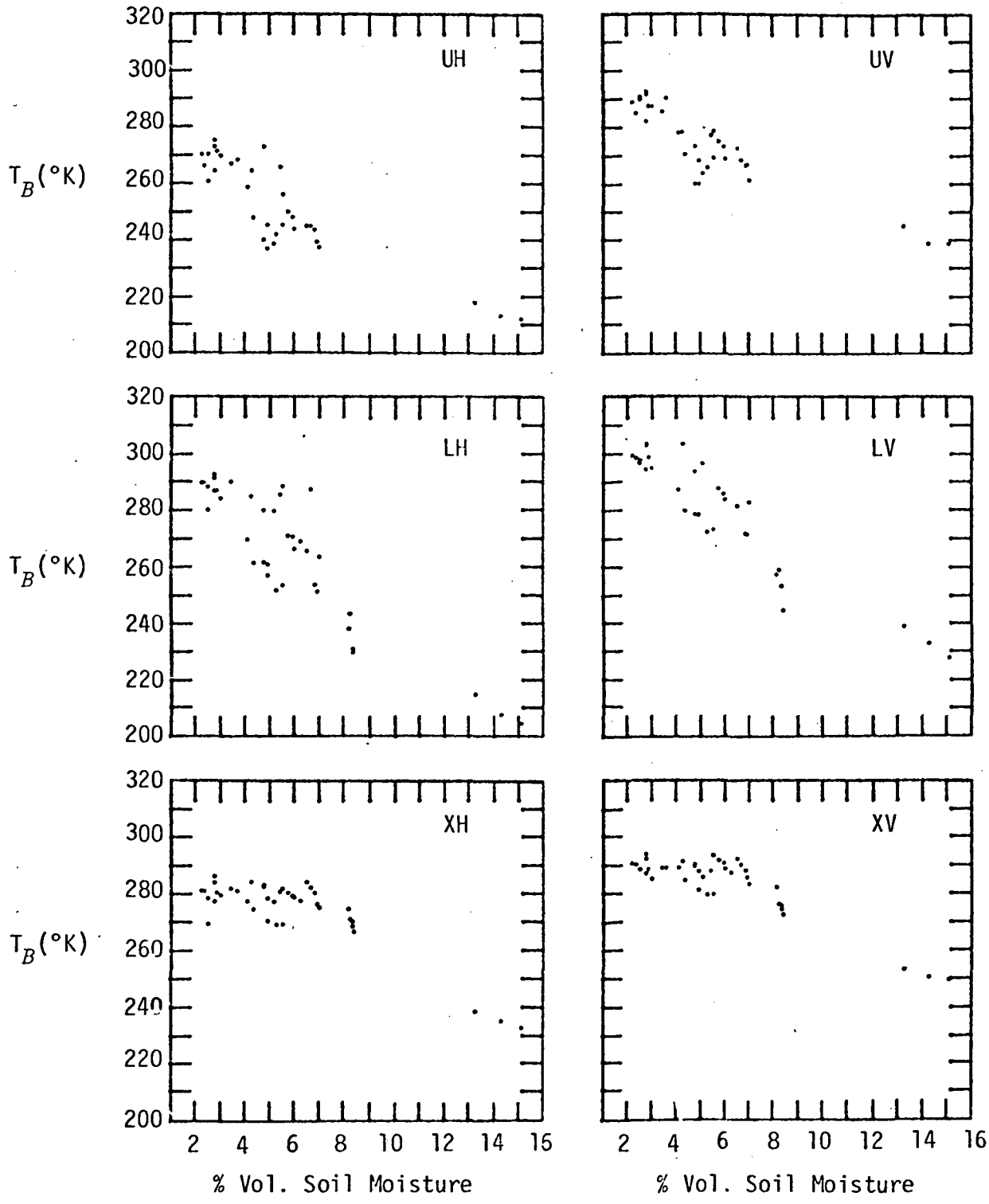

Figure 27(b). Microwave Brightness Temperature Versus Volumetric Soil Moisture in Top 0 - 2 cm for 1979 Smooth Field at a 35° Viewing Angle (U = 0.775 GHz, L = 1.4 GHz, X = 10.69 GHz, H = Horizontal Polarization, V = Vertical Polarization)

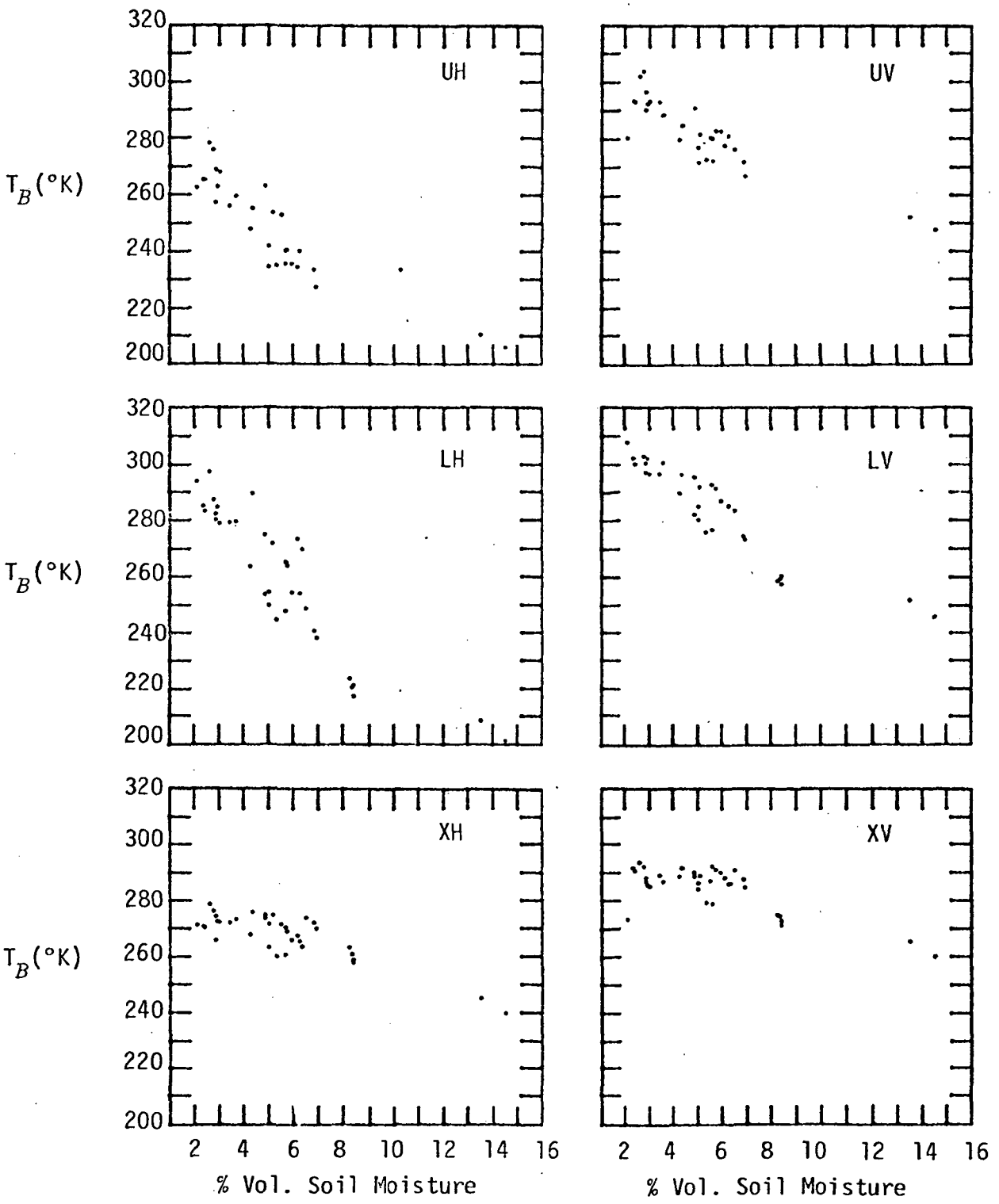

Figure 27(c). Microwave Brightness Temperature Versus Volumetric Soil Moisture in Top 0 - 2 cm for 1979 Smooth Field at a 45° Viewing Angle (U = 0.775 GHz, L = 1.4 GHz, X = 10.69 GHz, H = Horizontal Polarization, V = Vertical Polarization)

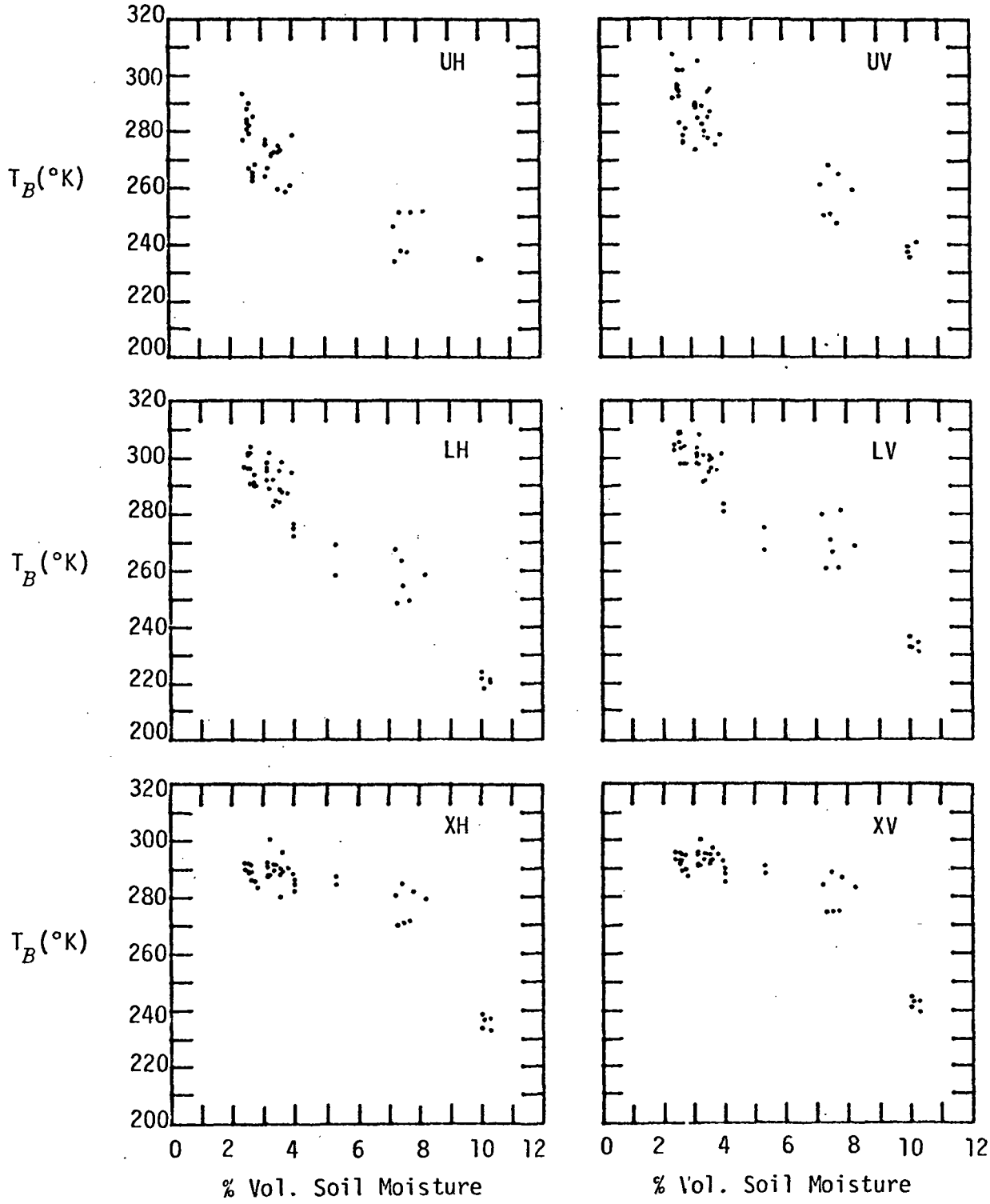

Figure 28(a). Microwave Brightness Temperature Versus Volumetric Soil Moisture in Top 0 - 2 cm for 1979 Rough Field at a 25° Viewing Angle (U = 0.775 GHz, L = 1.4 GHz, X = 10.69 GHz, H = Horizontal Polarization, V = Vertical Polarization)

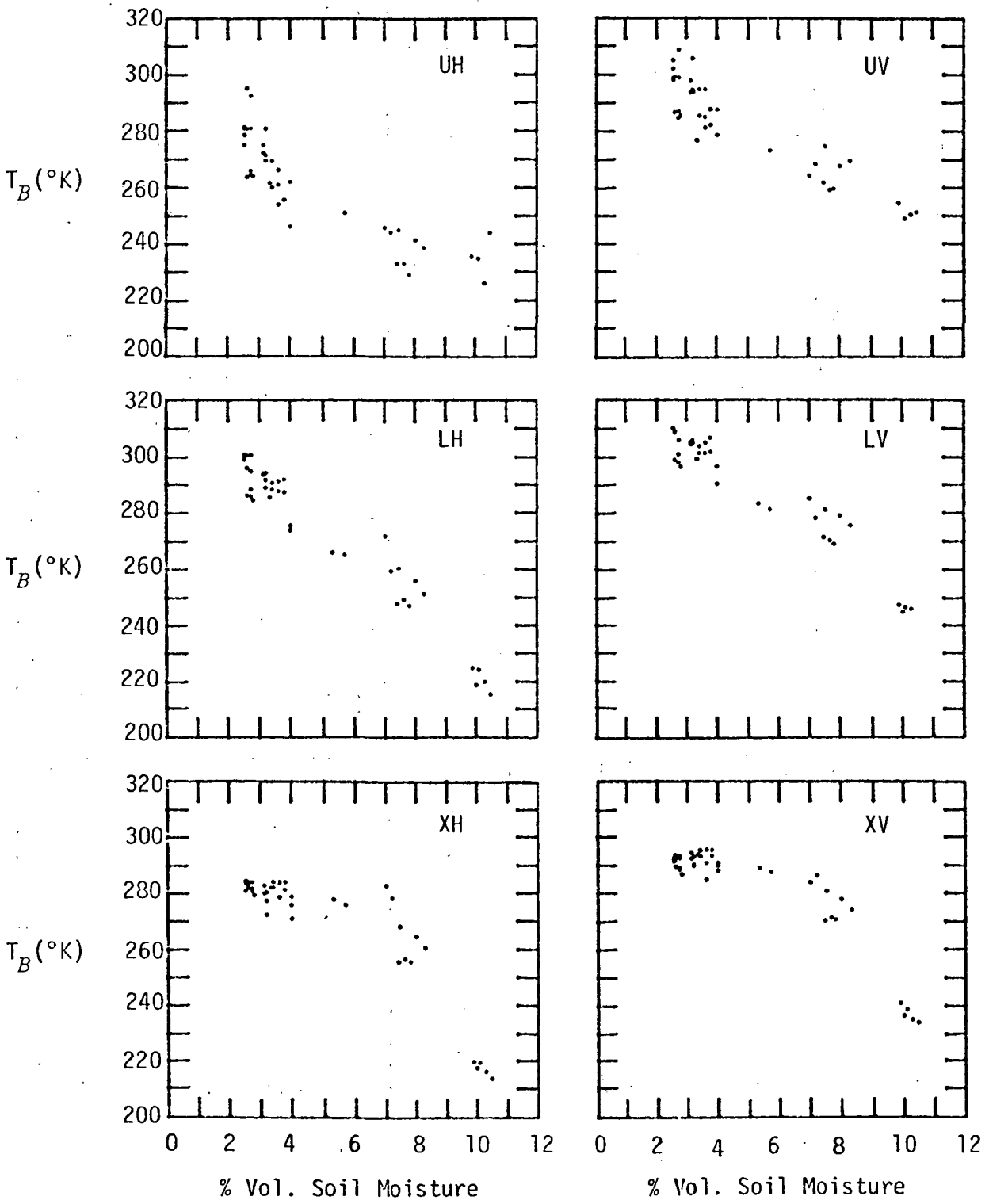

Figure 28(b). Microwave Brightness Temperature Versus Volumetric Soil Moisture in Top 0 - 2 cm for 1979 Rough Field at a 35° Viewing Angle (U = 0.775 GHz, L = 1.4 GHz, X = 10.69 GHz, H = Horizontal Polarization, V = Vertical Polarization)

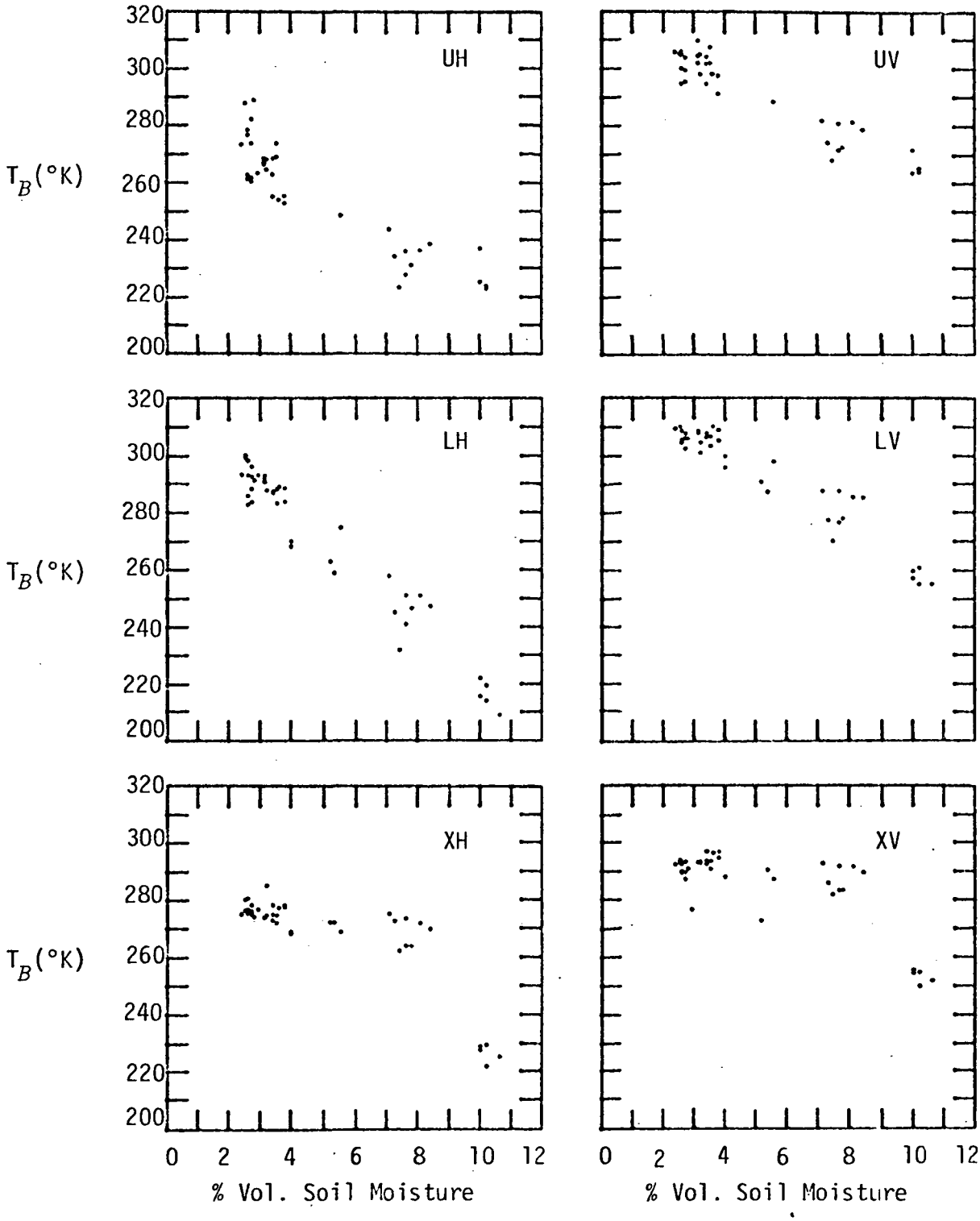

Figure 28(c). Microwave Brightness Temperature Versus Volumetric Soil Moisture in Top 0 - 2 cm for 1979 Rough Field at a 45° Viewing Angle (U = 0.775 GHz, L = 1.4 GHz, X = 10.69 GHz, H = Horizontal Polarization, V = Vertical Polarization)

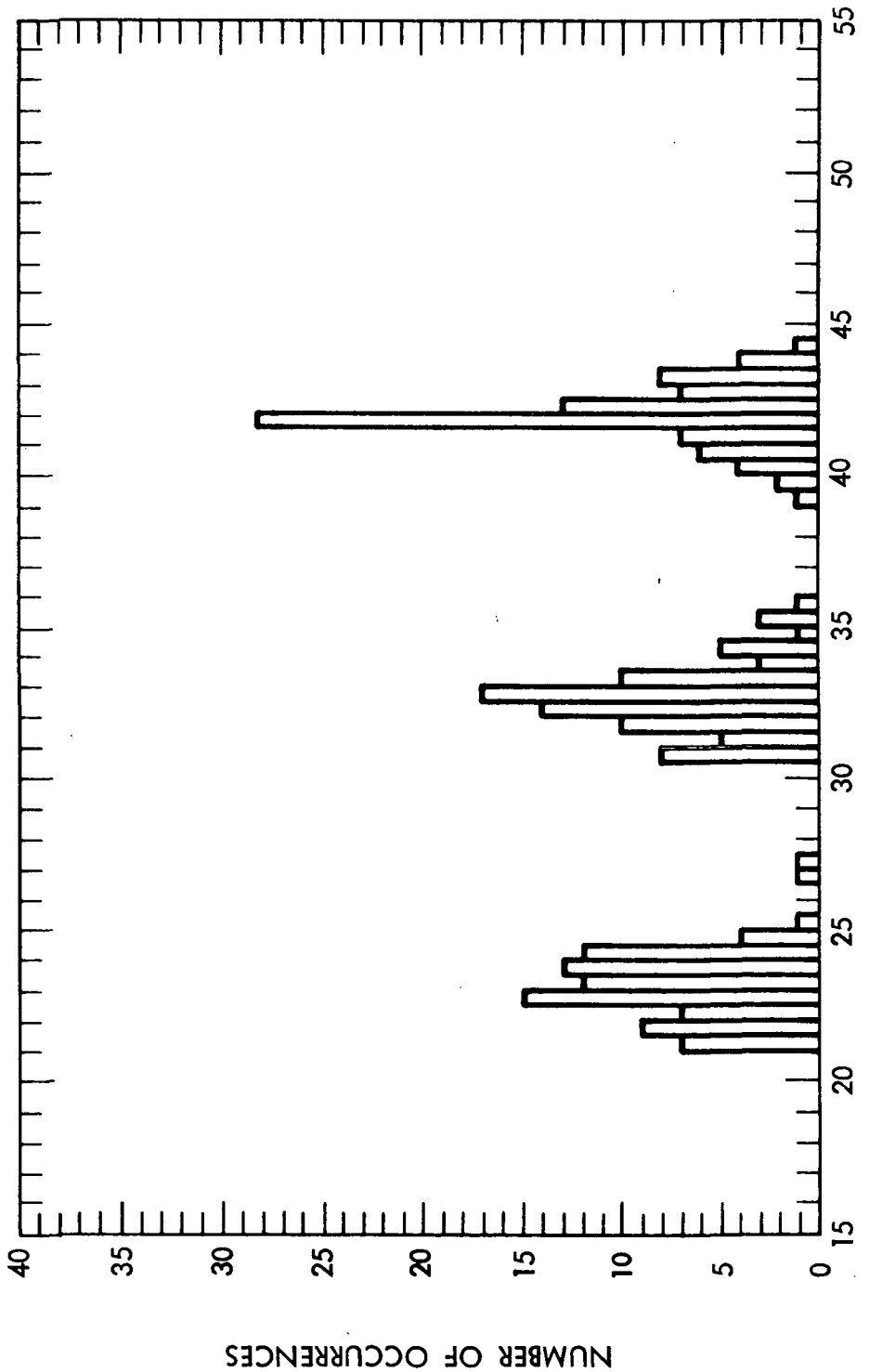

Figure 29. Histogram Showing Distribution of Viewing Angles Used in 1979 Microwave Measurements

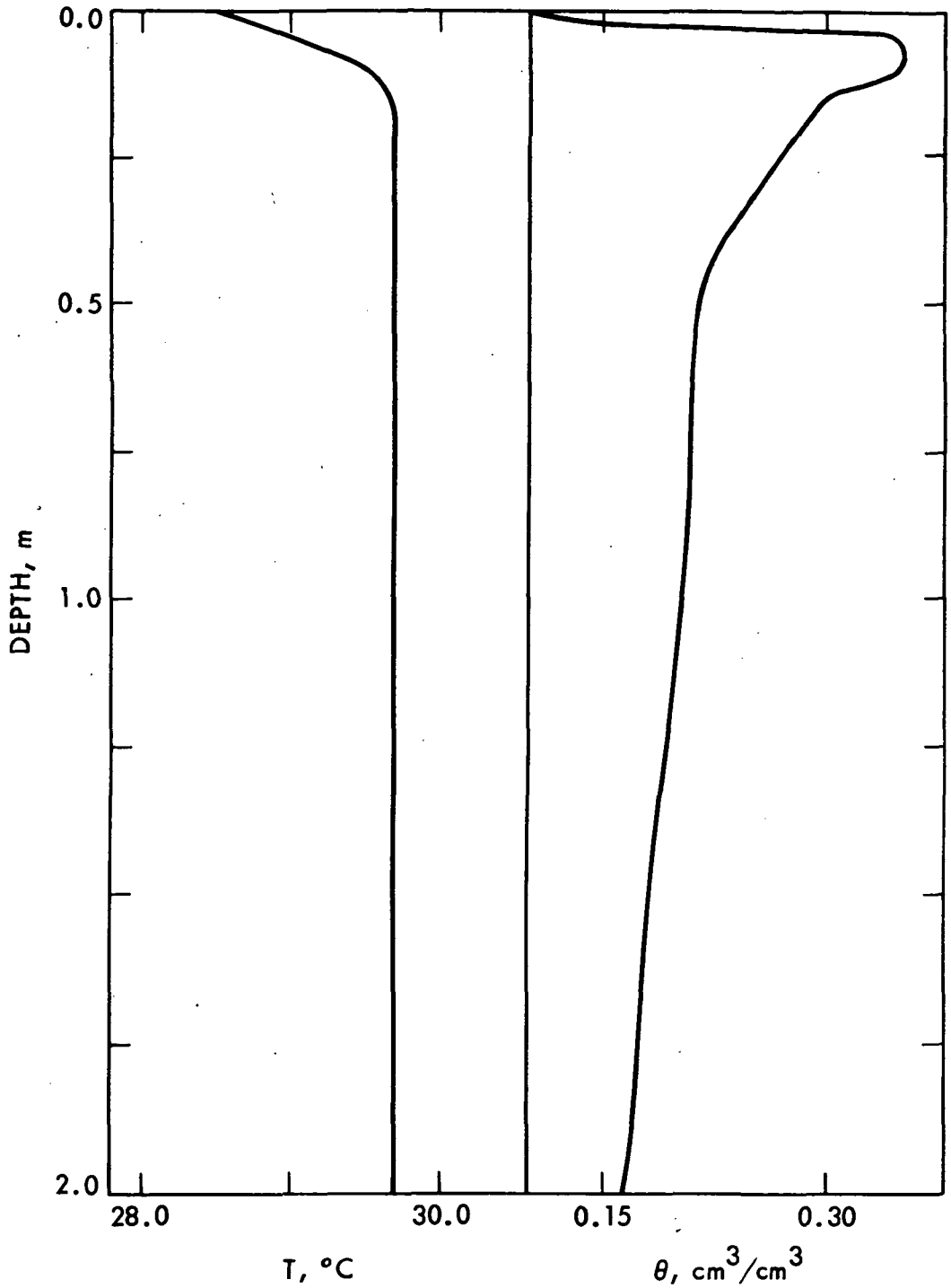

Figure 30. Initial Conditions for Numerical Model Calculations

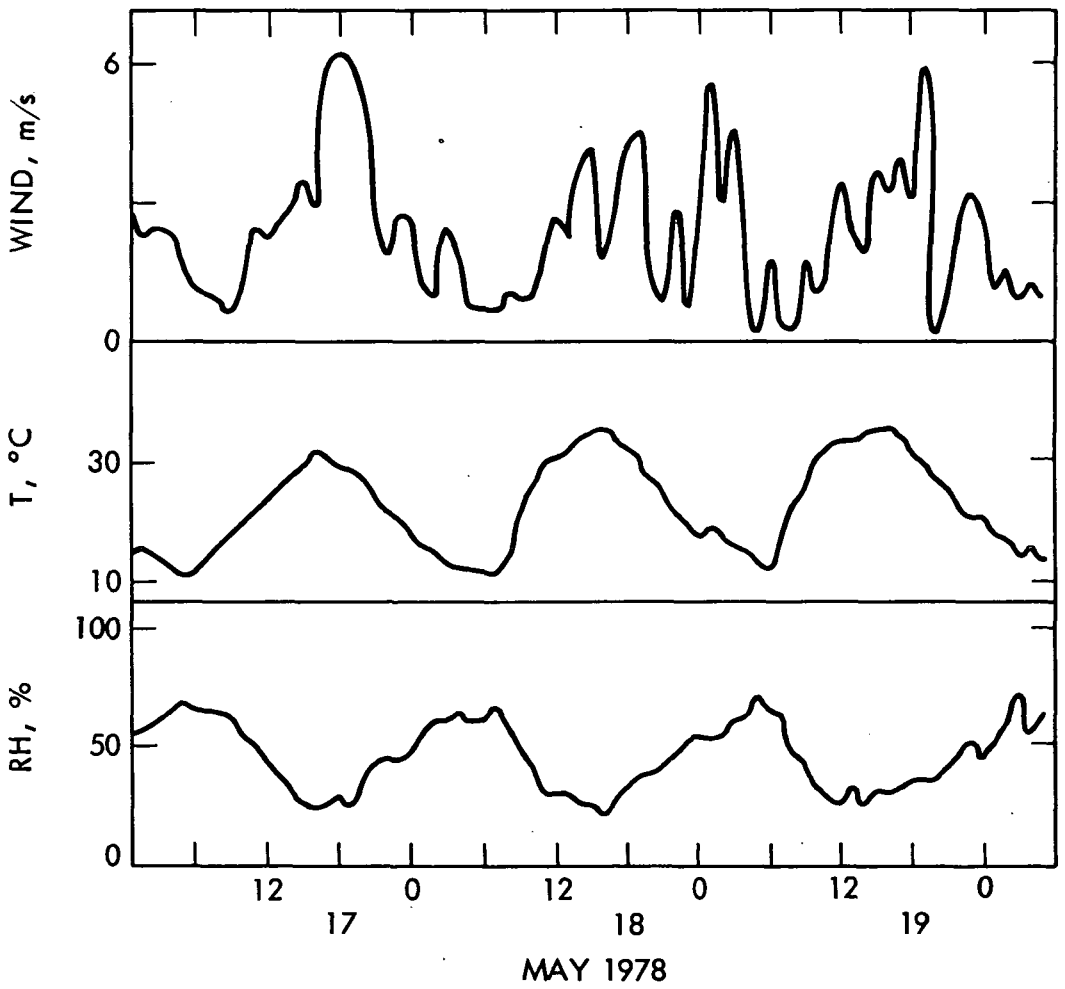

Figure 31. The Meteorological Boundary Conditions for Numerical Model Calculations. The Wind Speed, Air Temperature and Humidity Variations are for a Height of 2 m Above Ground

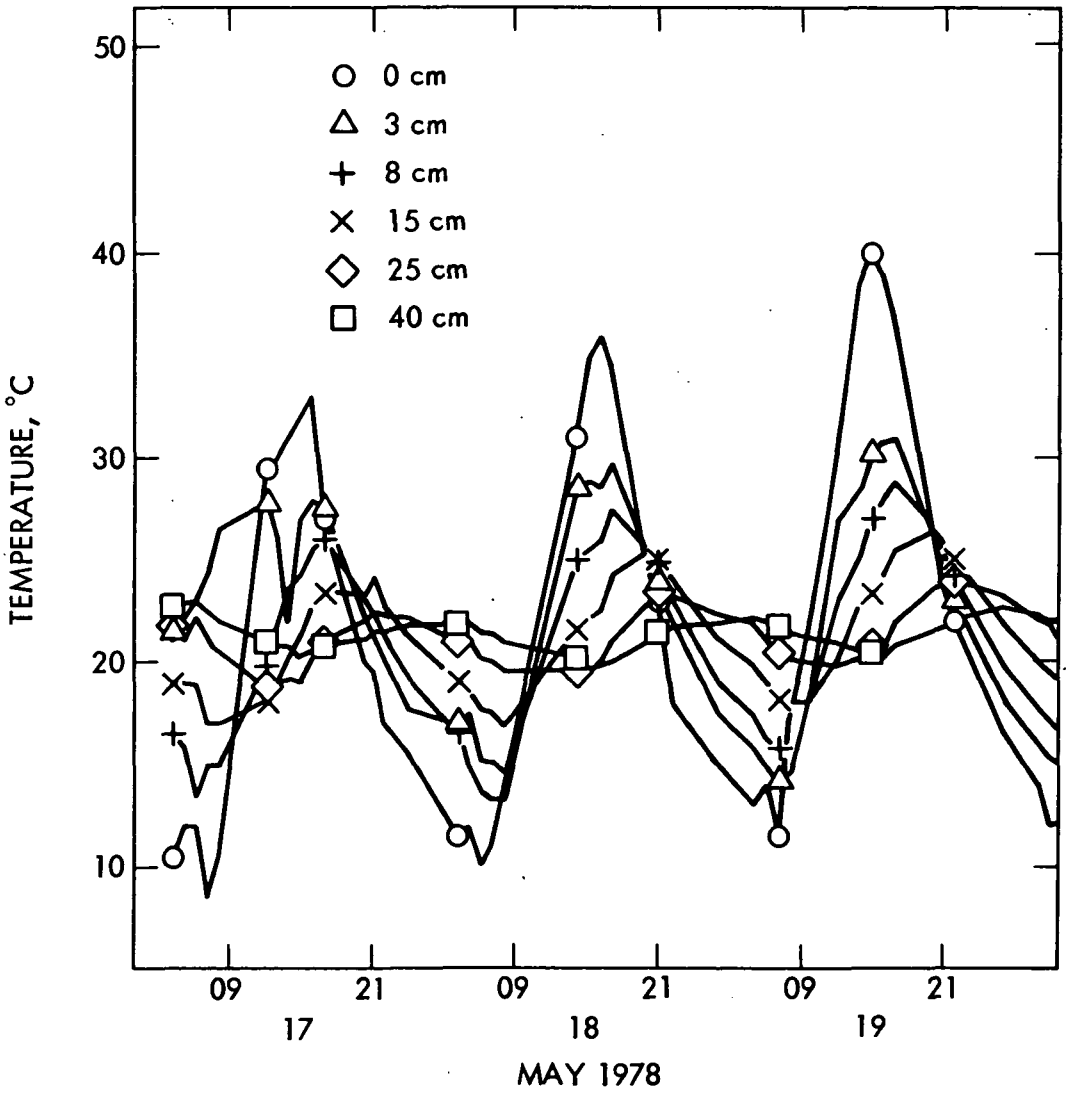

Figure 32. Observed Soil Temperature Variations at Six Different Depths on a Bare Field Near Bakersfield, California for the Period May 17 - 19, 1978

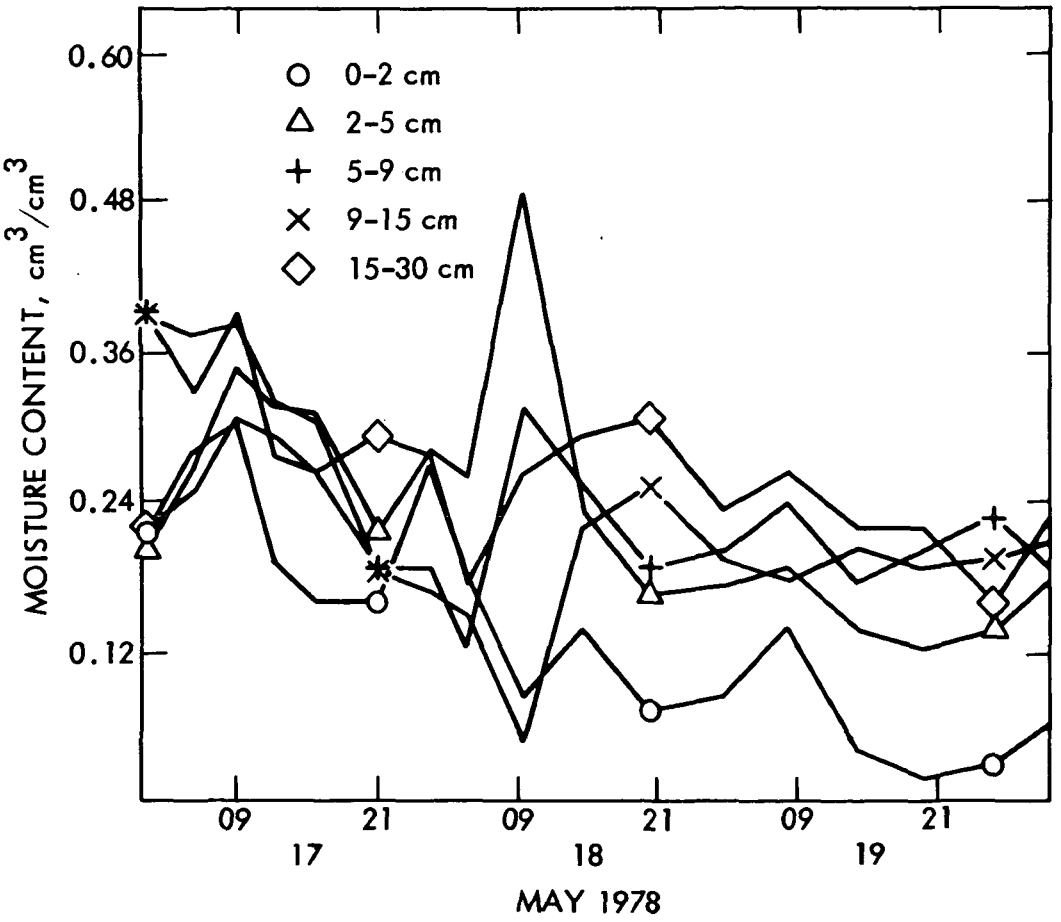

Figure 33. Observed Soil Moisture Content for the Same Time and Place

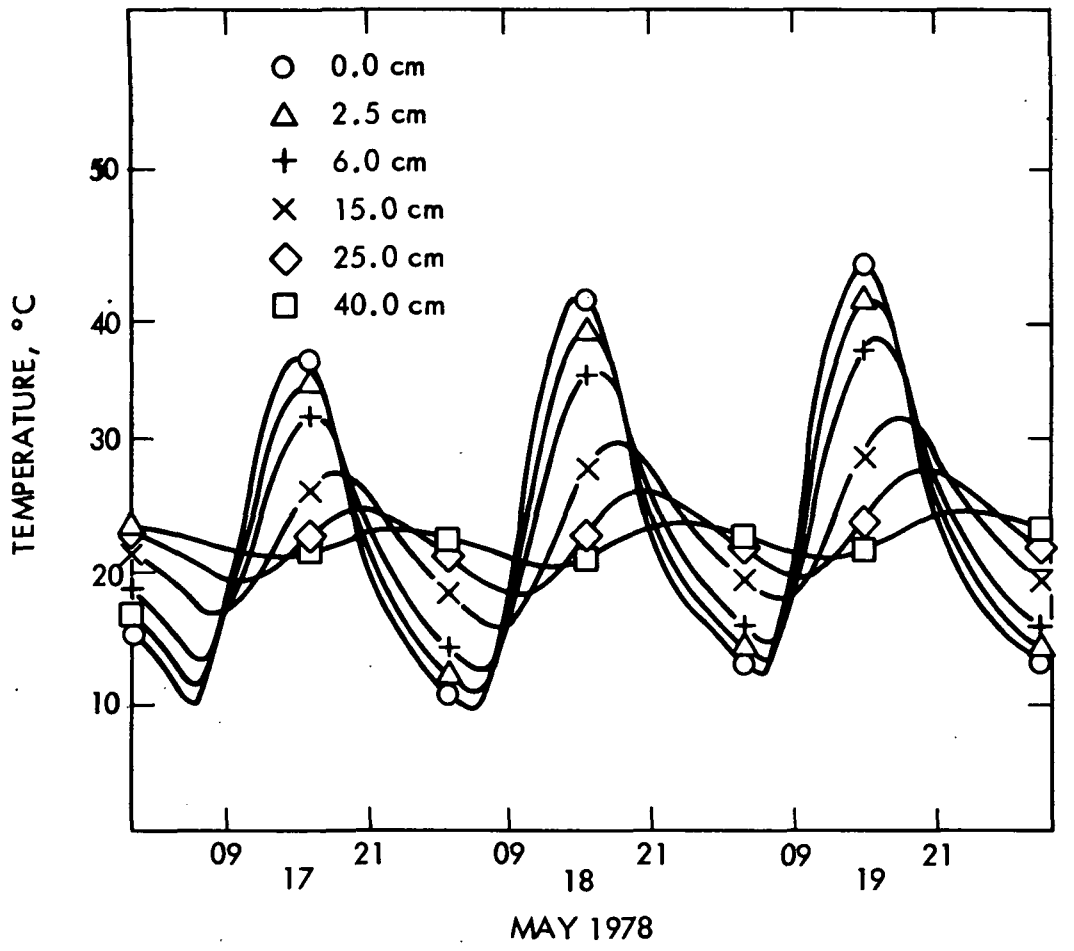

Figure 34. Calculated Soil Temperatures Obtained from the Numerical Model

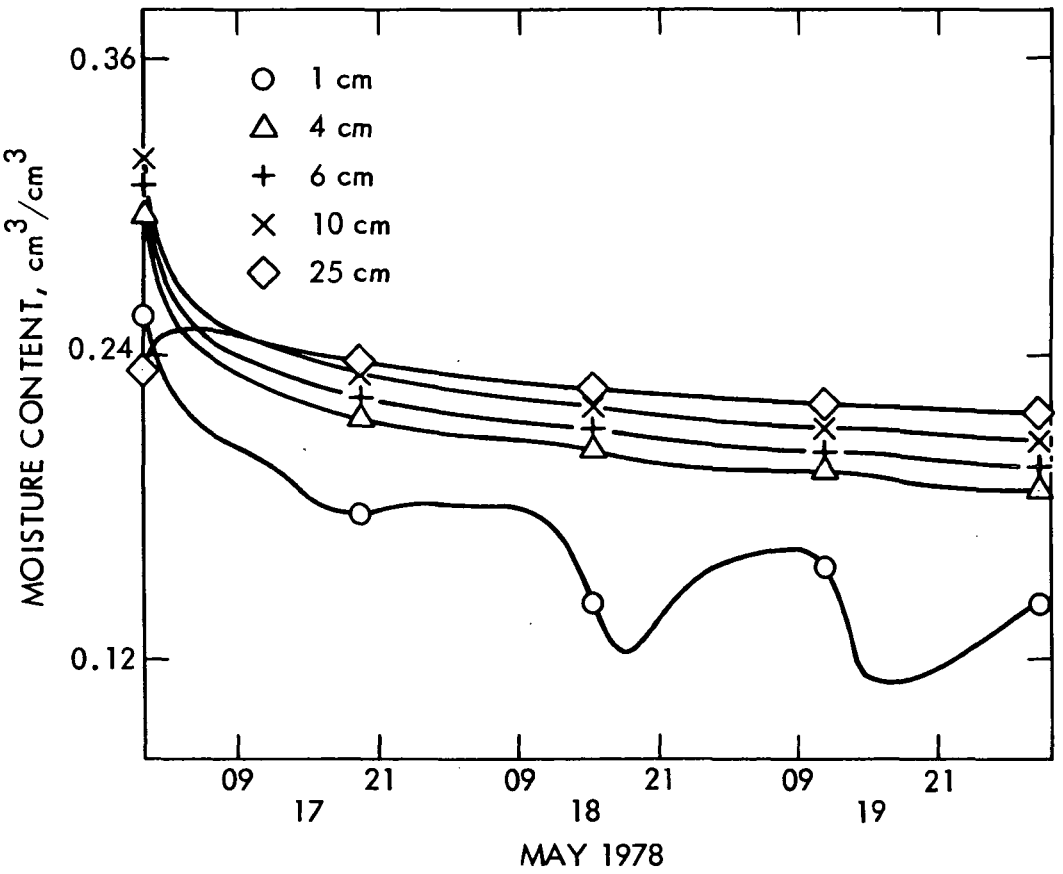

Figure 35. Calculated Soil Moisture Content Obtained from the Numerical Model

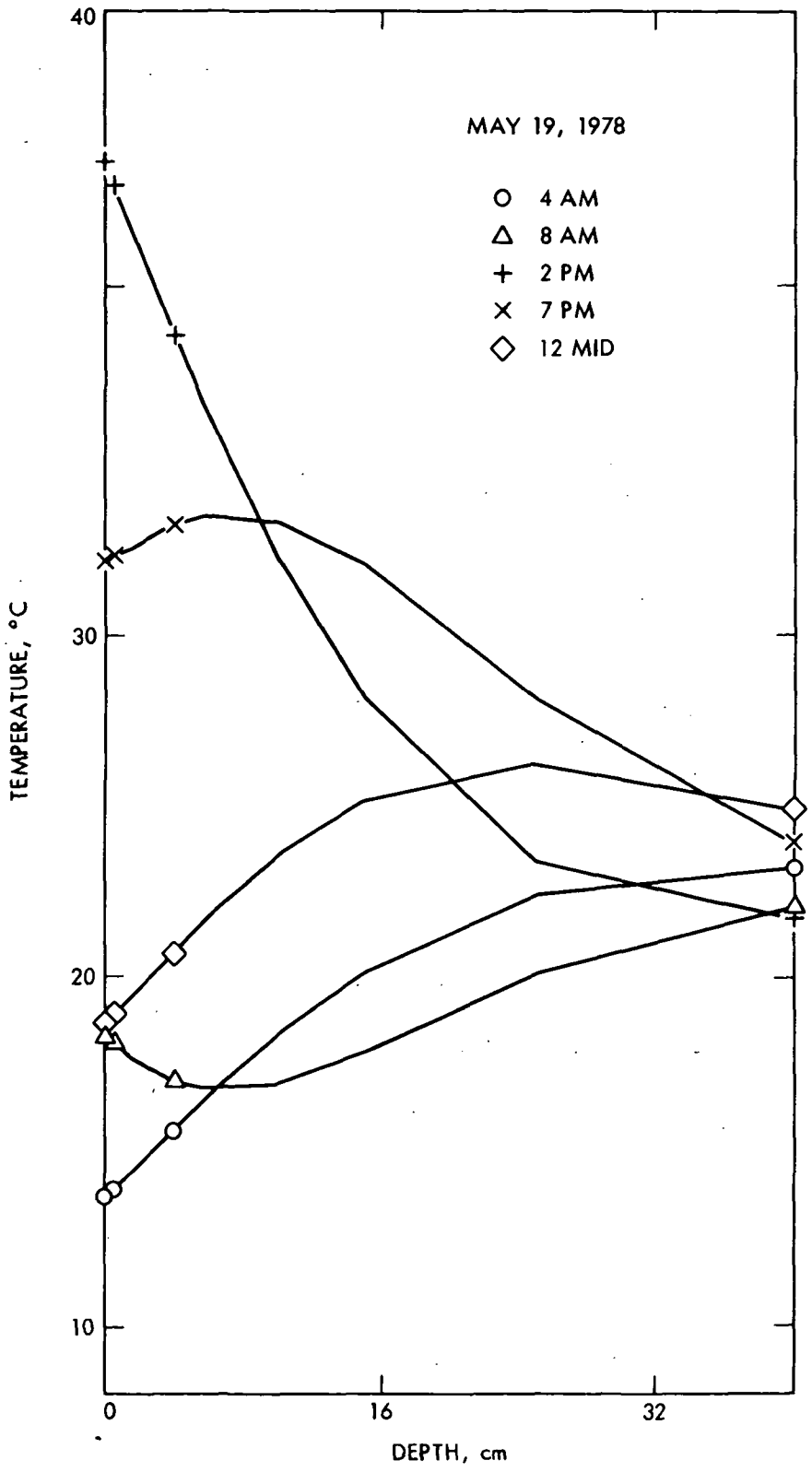

Figure 36. Calculated Soil Temperature Profiles for a 20-Hour Period on May 19, 1978 at the Test Site

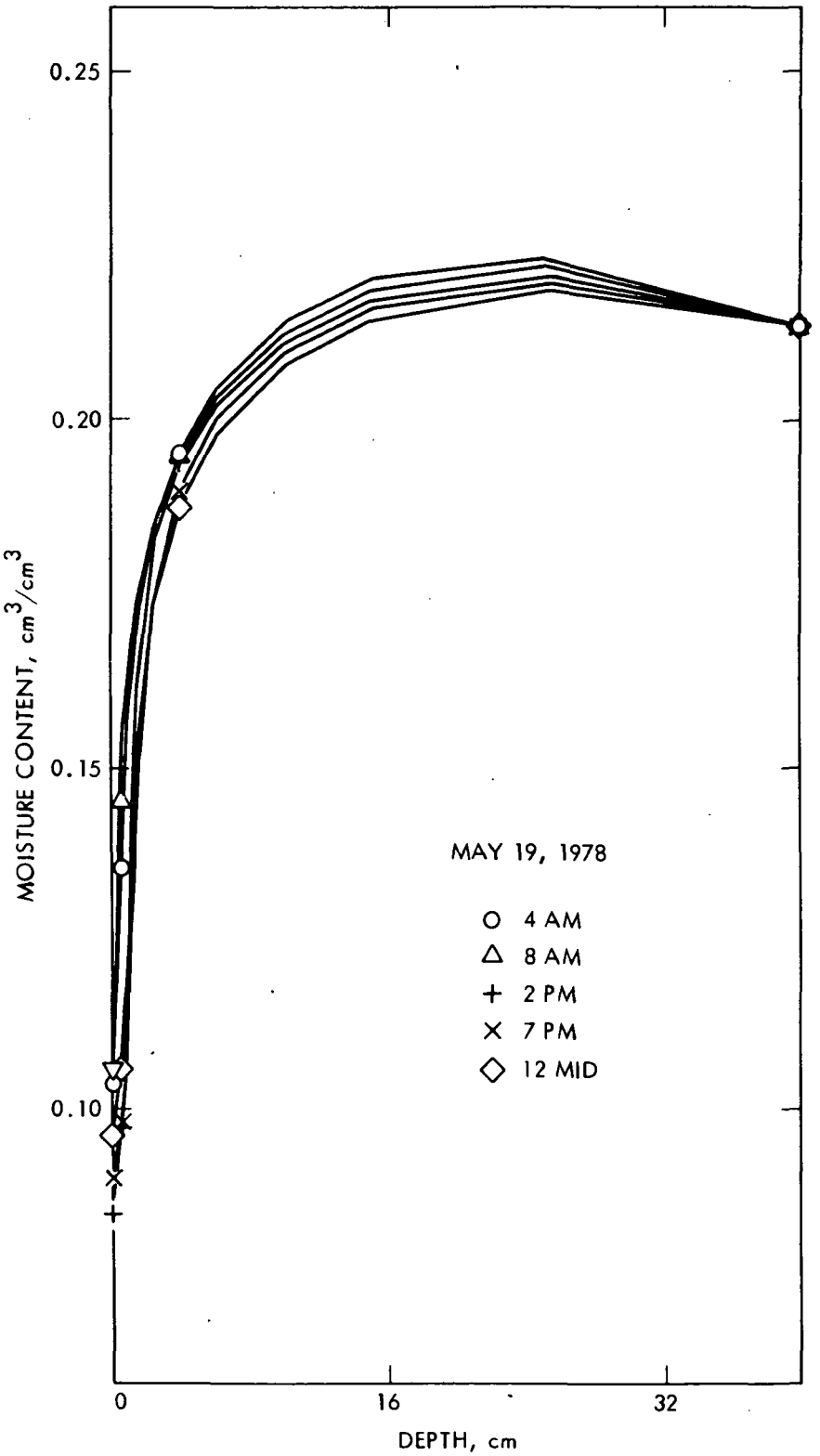

Figure 37. Calculated Soil Moisture Profiles for the Same Time and Place

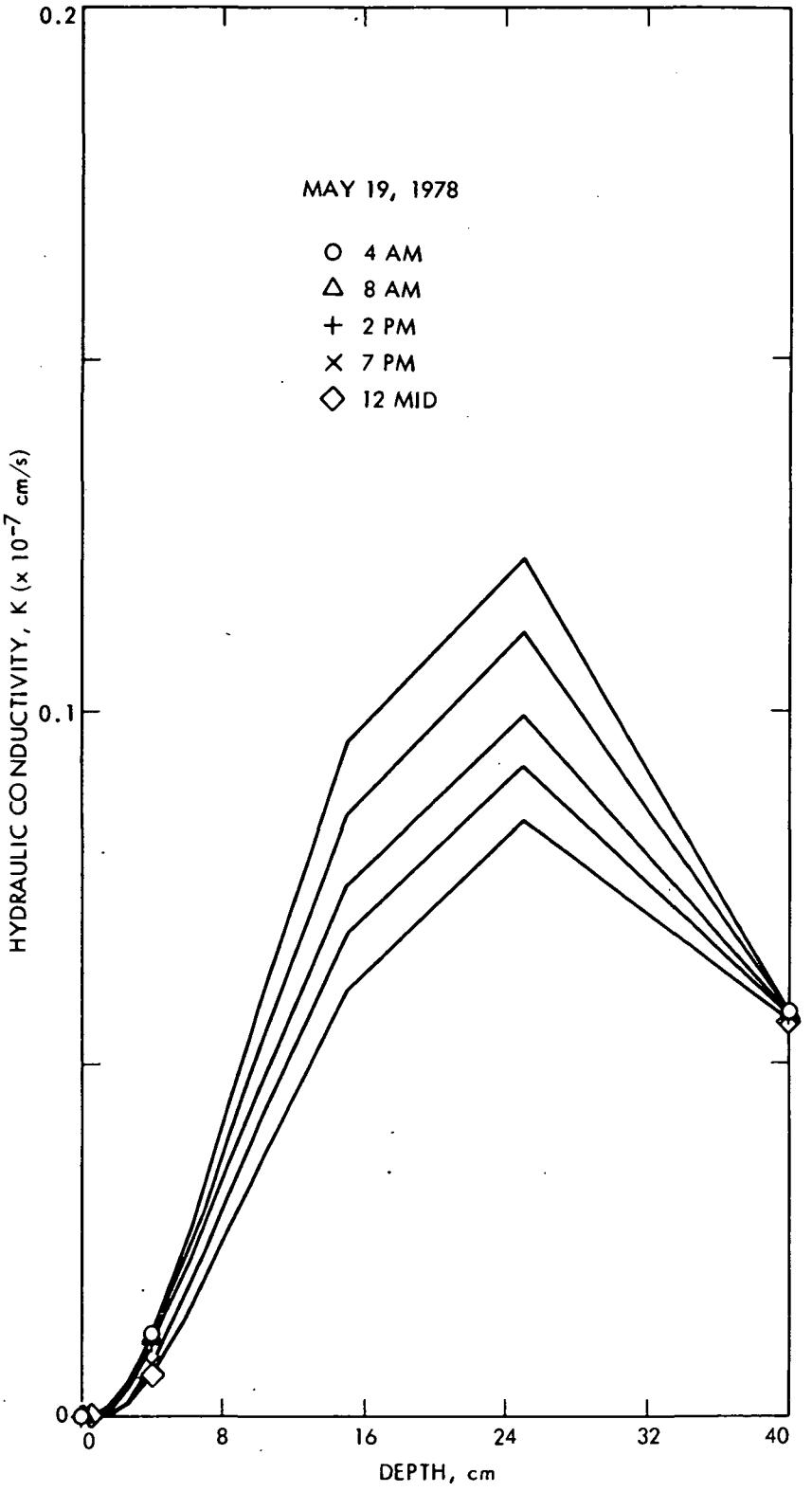

Figure 38. Values of Hydraulic Conductivity (K) Used in Calculating Curves in Figure 37.

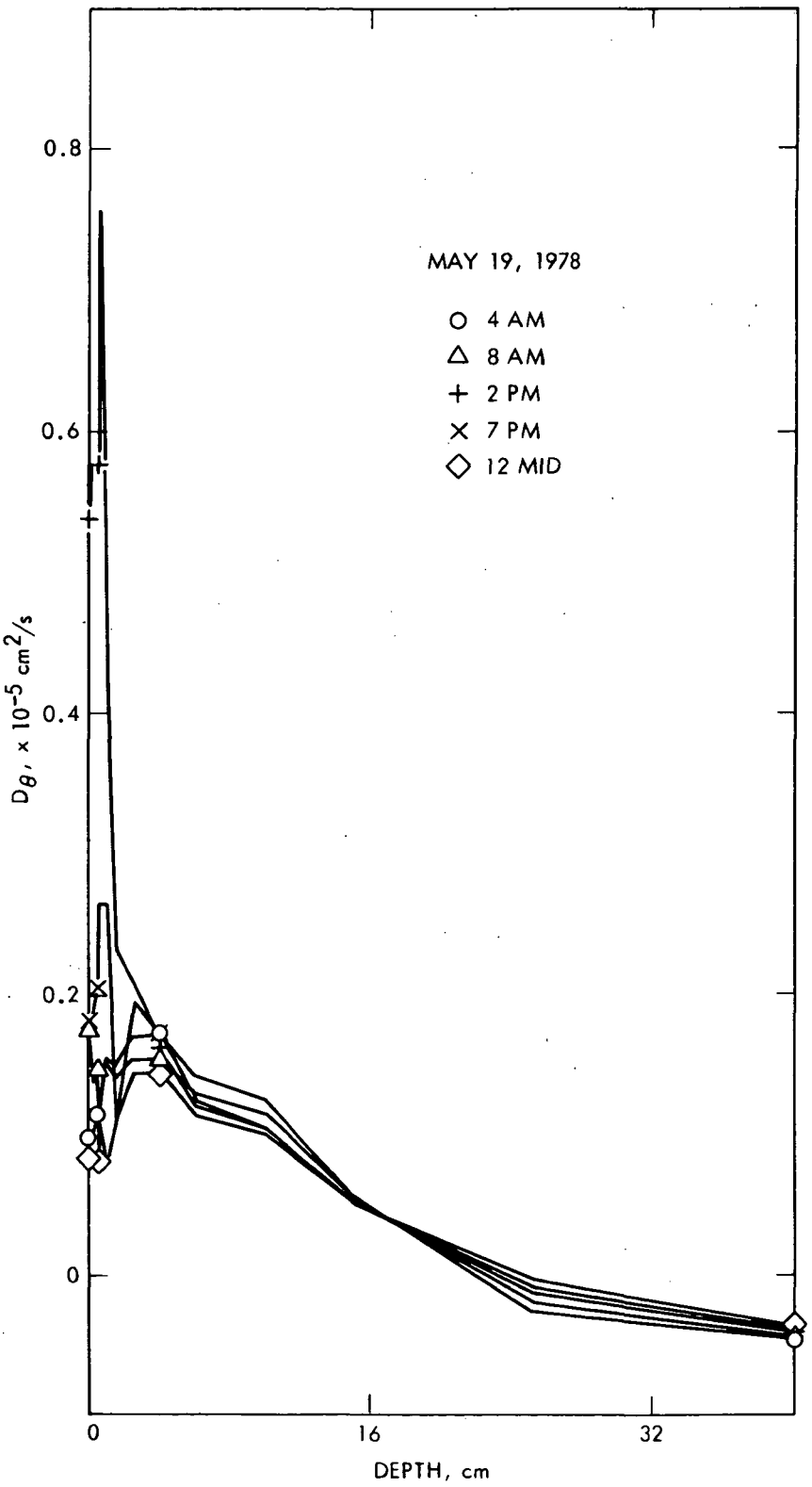

Figure 39. Values of Moisture Diffusivity (D_θ) Used in the Same Calculations

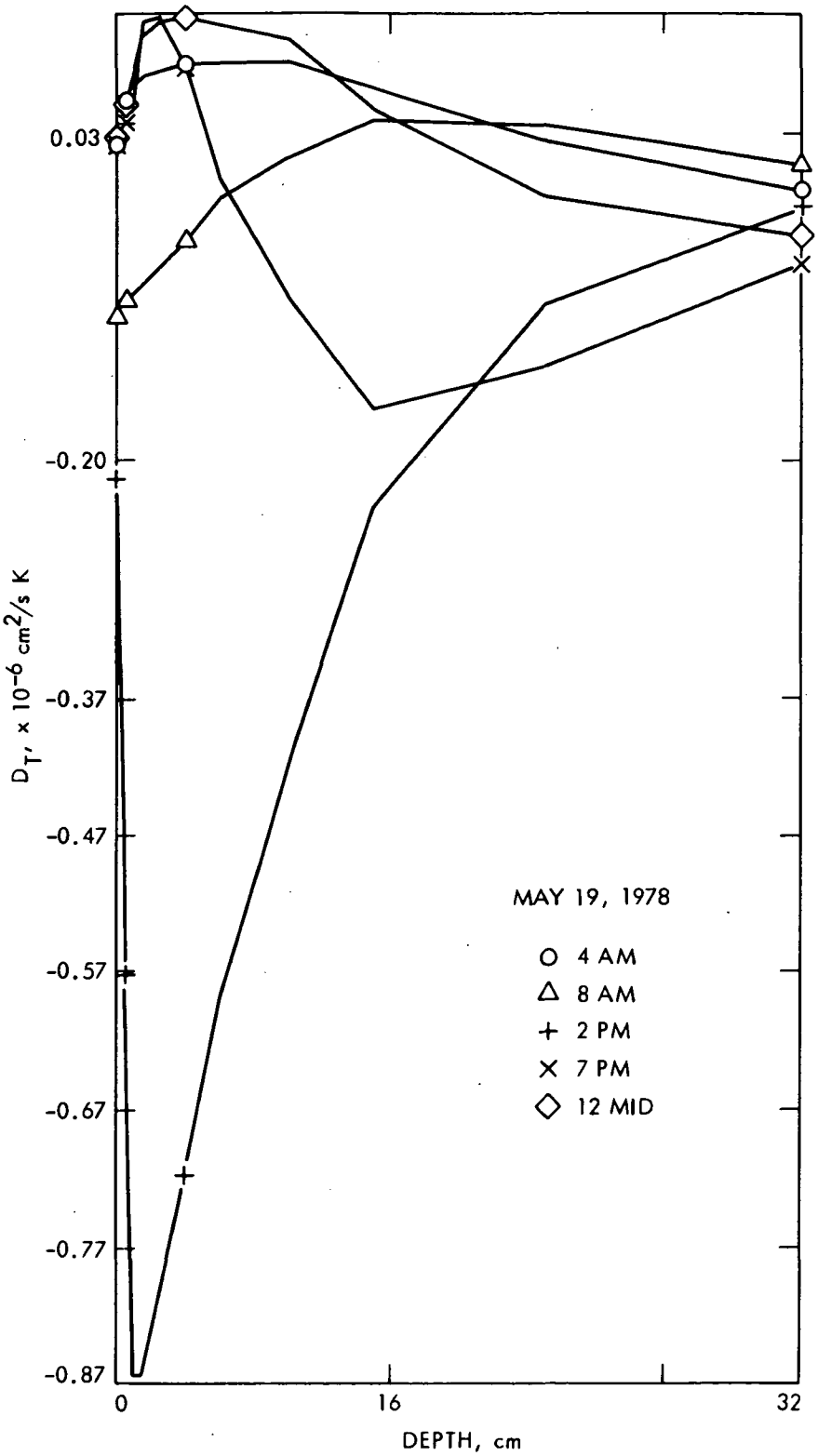

Figure 40. Values of Thermal Diffusivity (D_T) Used in the Same Calculations

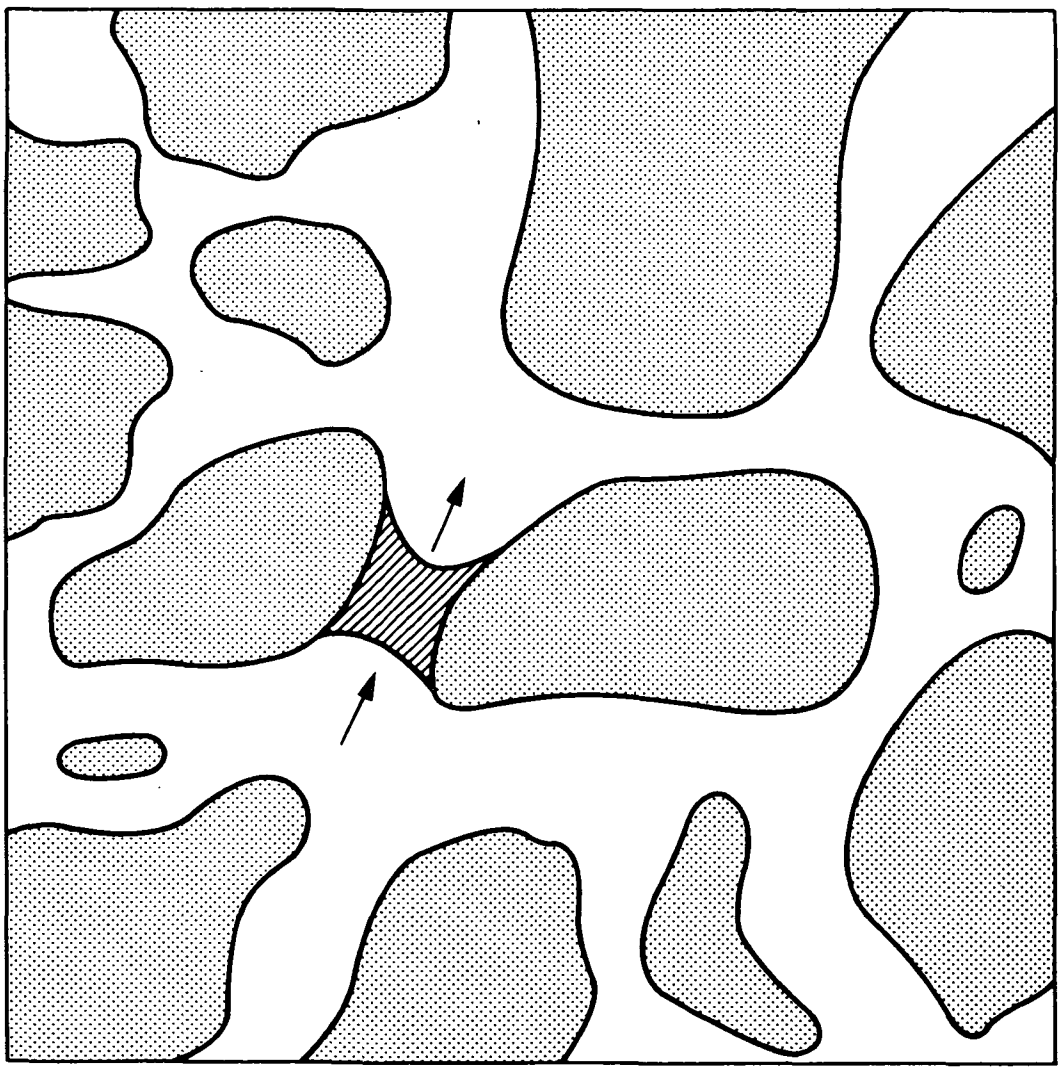

Figure 41. Schematic Diagram of Moisture Flow in a Very Dry Soil Medium. Liquid Bridge Connects Two Adjacent Soil Particles. Arrows Indicate Direction of Vapor Flux.

Appendix I.

Net Radiative and Turbulent Heat Flux Model

Most of the details regarding the parameterization of the net radiative heat flux (R_N) are given in Kahle (1977). A synopsis is given here.

The solar radiation incident on a surface with arbitrary slope and orientation is:

$$R_N(\text{solar}) = R_{diff} + \delta R(\cos Z'/\cos Z)$$

where $R_{diff} = 0.05\ S + 0.10(1-\cos Z)S$

Z = zenith angle of the sun

Z' = angle between the surface normal and the sun

$$S = (1-\alpha_g)S_s \cos Z \left[0.349(1-A) + \frac{0.651(1-\alpha_o)}{(1-\alpha_o \overline{\alpha}_g)}\right]$$

S_s = solar radiation incident at the top of the atmosphere

$A = 0.271(U^* \sec Z)^{0.303}$, Manabe and Möeller (1961) modification of Mugge-Möeller absorption function

U^* = effective water vapor content of the atmosphere; total precipitable water in a unit column of air for cloud-free conditions measured in gm/cm^2

αg = ground albedo

$\overline{\alpha g}$ = average ground albedo

$\alpha_o = 0.085-0.247 \ln[(P_s/1000)\cos Z]$; atmospheric albedo for Rayleigh scattering

P_s = surface pressure in mb

$\delta R = S - R_{diff}$

The longwave radiation from the earth's surface, assumed a perfect black body, is:

$$R_N(\text{terrestrial}) = \sigma T_o^4$$

where T_o is the ground temperature and σ the Stefan-Boltzmann constant.

The long wave radiation from the atmosphere to the earth's surface is

$$R_N(\text{Sky}) = \sigma T_{sky}^4,$$

where T_{sky} is an effective sky temperature, (Kondratyev, 1969):

$$T_{sky} = 263^o + (10^o \cos t)$$

and t is time measured from 1400 local time.

The sensible (Q_S) and latent (Q_E) heat fluxes are calculated by either of two methods:

1. The heat fluxes are obtained by the use of bulk transfer coefficients:

$Q_S = \rho_a c_p C_D W(T_a - T_o)$

$Q_E = \rho_a C_D W L(q_o - q_a)$,

where ρ_a = air density;

C_p = specific heat of dry air at constant pressure;

C_D = $0.002 + 0.006(\overline{Z}/5000)$, a drag coefficient;

W = modified wind speed, adjusted to incorporate gusty winds (equals actual wind speed plus 2 m/s);

$\overline{Z}$ = station elevation in meters;

T_a = air temperature above ground (usually obtained at 1-2 m);

T_o = air temperature at the surface

L = latent heat of condensation;

q_a = specific humidity of air above ground;

q_o = specific humidity of air at ground.

This formulation is used only when meteorological data is available at one height above the surface. Further details are given in Kahle (1977).

2. The heat fluxes are obtained from the profile method:

$$Q_S = \rho_a C_p U_* T_*$$

$$Q_E = \rho_a L U_* Q_*.$$

The parameters U_*, T_*, Q_* are obtained by integrating the equations below, which give the height variation of wind speed (U), temperature (T), and specific humidity (q),

$$\frac{\partial U}{\partial z} = \frac{U_*}{\kappa} \phi_m(\zeta)$$

$$\frac{\partial T}{\partial z} = \frac{T_*}{\kappa} \phi_h(\zeta)$$

$$\frac{\partial q}{\partial z} = \frac{Q_*}{\kappa} \phi_q(\zeta)$$

where κ is von Karmon's constant (=0.35). This method requires meteorological data (U, T, q) at two or more levels above the ground. The functions ϕ_m, ϕ_h, ϕ_q are diabatic functions of ζ which have been empirically obtained (Businger et al., 1971), and which account for the stability of the air near the ground. This is indicated by ζ, a parameter proportional to the bulk

Richardson number of the height interval (e.g., see Yaglom, 1977). During the day, ζ is usually <0 (unstable conditions); at night, ζ is usually >0 (stable conditions).

Finally, U_*, T_*, Q_* are calculated by a least-squares fit of the U, T, q data, measured at several different levels, to the integrated form of the above equations. In this study, U, T, q are obtained from 16 minute averages measured at 7 levels (1/8, 1/4, 1/2, 1, 2, 4, and 8 m) on the portable JPL micrometeorological tower (Kahle et al., 1977).

Appendix II.

Physical Properties of Soils and Soil Components

Table II-1 is a compilation of median values of physical properties of a number of different soils. The list is nominally arranged according to particle size. The parameters have been abstracted from a variety of sources (Baver, 1933; Gustafson, 1941; Ingersoll et al., 1954; de Vries, 1963; Glinka, 1963; Clark, 1966, Davis and De Wiest, 1966; Gary, McAfee, and Wolf, 1972).

Table II-1.

Physical Properties of Soils

Type	Grain Size	Porosity	Bulk Density	Specific Heat
clay	<0.02	0.550-0.620	2.65	0.180
silt	.0625-.002	0.480-0.550	2.70	0.180
fine sand	.0625-0.25	0.480	2.75	0.190
med. sand	0.25-0.50	0.430	2.70	0.190
coarse sand	0.5-2.0	0.380	2.65	0.190
gravel	2.0-75.0	0.320-0.380	2.70	0.195

Grain size pertains to the particle diameter measured in millimeters. Porosity is the volume of pore space per total volume of soil material measured in cm^3/cm^3. Bulk density pertains to the dry weight of material measured in gm/cm^3. Isobaric specific heat values are given for temperatures near 20^oC and are in units of cal/gm^oC.

Table II-2 gives densities and thermal properties of air, water, and soil materials. Values are taken from de Vries (1963), the Smithsonian Meteorological Tables (1951), and Iribarne and Godson (1973).

Table II-2.

Density and Thermal Properties of Air, Water, Soil Materials

Type	Density	Specific Heat	Thermal Conductivity	Thermal Diffusivity
Dry air (20°C)	0.00120	0.240	0.0614	0.213
Water, liquid (20°C)	0.998	0.999	1.43	0.0014
Moist air (20°C, saturated)	0.00119	0.243	0.241	0.835
Clay minerals	2.65	0.181	7.0	0.0146
Quartz	2.66	0.180	21.0	0.0044
Organic matter	1.30	0.46	0.6	0.0010

The units for the parameters listed above are: density (gm/cm^3), specific heat at constant pressure ($cal/cm^3\ ^oC$), thermal conductivity ($mcal/cm\ sec\ ^oC$), and thermal diffusivity (cm^2/sec).

Appendix III

Water Vapor Transport in Nearly Dry Soils

In a relatively dry medium, water vapor transport due to temperature differences occurs in the vapor-liquid continuum as a series-parallel process. Below a certain "critical" water content, θ_c, the liquid phase does not exist as a continuous fluid but rather consists of a network of distinct "islands" connected by vapor filled pores. These liquid islands bridge adjacent soil particles (figure 41). The vapor flux in the air-filled pores adjusts itself to moisture flux through the liquid islands. The total vapor flux density in the medium then becomes proportional to $(a + \theta)(\overline{\nabla}_z T)_a$ (Philip and de Vries, 1957).

The parameter η (equation 25) is significant when θ falls below the critical water content (θ_c) to account for the series-parallel moisture flow and its effect on the rate of vapor transfer,

$$\eta = \frac{a + f(a)\theta}{\alpha a} \frac{(\overline{\nabla}_z T)a}{(\overline{\nabla}_z T)}. \qquad \text{(A1)}$$

Here $f(a) = 1,\ a > a_c,\ a/a_c,\ a < a_c$ where a_c is defined as the value of a when $\theta = \theta_c$. The total temperature gradient in the medium is the weighted sum of all the temperature gradients in each soil component,

$$\overline{\nabla}_z T = a(\overline{\nabla}_z T)_a + \theta(\overline{\nabla}_z T)_\theta + s(\overline{\nabla}_z T)_s \qquad \text{(A2)}$$

where $s = 1 - a - \theta$.

Then ζ is defined as the ratio

$$\zeta = (\overline{\nabla}_z T)a/(\overline{\nabla}_z T). \tag{A3}$$

Specifically,

$$k_i = \frac{(\overline{\nabla}_z T)_i}{(\overline{\nabla}_z T)_0} \tag{A4}$$

where i = soil particles, water, or air and 0 refers to the medium, either air or water. The k_i are calculated by the method of de Vries (1963) described previously. Then ζ is derived as follows.

When water is the continuous medium, ζ is obtained from A2, A3, and A4,

$$\zeta = \frac{k_2}{ak_2 + \Theta + sk_1} \tag{A5}$$

where $k_1 = (\overline{\nabla}_z T)_s/(\overline{\nabla}_z T)_\Theta$ and $k_z = (\overline{\nabla}_z T)_a/(\overline{\nabla}_z T)_\Theta$.

When air is the continuous medium, ζ becomes

$$\zeta = \frac{1}{a + \Theta k_3 + sk_4} \tag{A6}$$

where $k_3 = (\overline{\nabla}_z T)_\Theta/(\overline{\nabla}_z T)_a$ and $k_4 = (\overline{\nabla}_z T)_s/(\overline{\nabla}_z T)_a$.

Table III-1 gives an example of the variation of η and ζ with Θ for a sandy clay loam.

Table III-1.

Variation of Soil Parameters for Vapor Transport

Θ	a	s	ζ	η
0.000	0.503	0.497	1.924	2.884
0.100	0.403	0.497	1.657	3.066
0.200	0.303	0.497	1.760	3.874
0.300	0.203	0.497	1.877	4.790
0.400	0.103	0.497	2.011	5.836
0.500	0.003	0.497	2.165	7.042

The ζ for most soils ranges from about 1.5 to 3.0.